

Master thesis 2006

Exact diagonalization of  
quantum dots

Espen Flage-Larsen

May 31, 2006





# Contents

<b>1</b>	<b>Introduction</b>	<b>8</b>
1.1	Why are quantum dots important? . . . . .	8
1.2	Historical notes about the evolution of quantum dots . . . . .	9
<b>2</b>	<b>Properties of quantum dots</b>	<b>10</b>
2.1	Structure, manufacture and operational principle . . . . .	11
2.1.1	Electron confinement using physical boundaries . . . . .	11
2.1.2	Electron confinement using electrical fields . . . . .	13
2.2	Charge quantization and Coulomb blockage . . . . .	14
<b>3</b>	<b>Theoretical approximations to quantum dots</b>	<b>18</b>
3.1	Single electron quantum dot . . . . .	18
3.1.1	Two dimensions . . . . .	19
3.1.2	Three dimensions . . . . .	23
3.2	Two electron quantum dot . . . . .	26
<b>4</b>	<b>Interacting electrons and diagonalization</b>	<b>30</b>
4.1	Diagonalization in the harmonic oscillator basis . . . . .	31
4.1.1	Relative terms in two dimensions . . . . .	31
4.1.2	Relative term in three dimensions . . . . .	35
4.1.3	Discussions regarding matrix cut-off and matrix element calculation scheme . . . . .	35
4.2	Perturbation as an alternative . . . . .	43
4.3	Diagonalization results . . . . .	45

<b>5</b>	<b>Structure of quantum dots in laboratory basis</b>	<b>53</b>
5.1	Many-particle basis for the shell model . . . . .	53
5.2	Effective interactions and the transformation to laboratory basis . . . .	58
5.3	Brief notes about OSMC and the diagonalization process . . . . .	65
5.4	Comparison of energies using OSMC and CM-rel diagonalization . . . .	66
5.5	Many-particle diagonalization using OSMC . . . . .	67
5.5.1	Four particles . . . . .	68
5.5.2	Six particles . . . . .	69
5.5.3	Eight particles . . . . .	70
<b>6</b>	<b>Concluding remarks</b>	<b>72</b>
<b>A</b>		<b>75</b>
A.1	Lanczos methods . . . . .	75
A.2	Gauge transformations and invariance . . . . .	78
A.3	Coordinate transformations . . . . .	79
A.4	Transformation from center-of-mass to laboratory . . . . .	83
A.5	Time-independent perturbation theory . . . . .	86
A.6	Numerical Integration . . . . .	89
A.6.1	Equal step techniques . . . . .	89
A.6.2	Gaussian quadrature techniques . . . . .	91
A.6.3	Numerical analysis of the numerical integration techniques . . . .	92
A.7	Solution of the radial equation . . . . .	96
A.7.1	Two dimension . . . . .	96
A.7.2	Three dimension . . . . .	100
A.8	Exact solution for the interacting part in relative coordinates . . . . .	102
A.9	Expressions . . . . .	107
A.9.1	Coefficient for the two dimensional Coulomb interaction . . . . .	107

# Preface

This thesis' main idea is to investigate whether the Oslo Shell Model Code [Engeland; 1990-2006] could be used to calculate the structure of many-particle quantum dots. The Oslo Shell Model Code, hereafter OSMC, has been developed to investigate nuclear spectra. If this code could be adapted to quantum dots, we would be able to obtain their structure by exact diagonalization. To be able to use the OSMC we have developed an effective two-particle interaction.

The theoretical descriptions of quantum dots are usually given in two dimensions. In many cases this is an approximation that imitate the experimental situation well, but it is nevertheless an approximation. In this thesis we compare two and three dimensional quantum dots. As we will show in this thesis they are closely related. The spherical symmetric harmonic oscillator potential is used as the confining potential. In addition, a constant magnetic field is applied along the third axis. Using spherical symmetric harmonic oscillators, analytic solutions are found for the non-interacting particles. They will serve as a basis for our two-particle calculations. An analytical solution for the relative motion of the two-particle system is also developed and used as a check for the chosen basis.

The layout of this thesis is as follows. The non-theoretical introduction is given in Chapter 1, where we first explain the importance of the quantum dot followed by a historical overview. In Chapter 2 we take a quick look at the manufacturing techniques, experimental setups and briefly explain the Coulomb blockage.

A theoretical approximation to the single-electron quantum dot is given in Chapter 3. Analytical solutions are developed for both two and three dimensions and the results are compared. At the end of Chapter 3, the two-electron quantum dot is considered by transforming the two-electron Hamiltonian into center-of-mass and relative coordinates. The relative motion only has analytic solutions for special oscillator parameters. A general solution will be obtained by exact diagonalization in a harmonic oscillator basis and the limited analytic solutions will be used to check the results. The center-of-mass motion is simple as it is basically a harmonic oscillator.

Chapter 4 deals with the diagonalization of the two-particle quantum dot. The matrix elements of the interaction are calculated using both numerical integration and series expansion. A discussion of different numerical integration techniques are also introduced accordingly. The two methods are then compared. As an alternative to exact diagonalization we employ second order perturbation theory and compare the results with the exact diagonalization. Results from the diagonalization are listed at

the end of Chapter 4.

In Chapter 5 we set up a basis for the many-particle quantum dot and develop an effective interaction by the use of Lee-Suzuki transformations [Lee and Suzuki; 1980]. The center-of-mass and relative basis is an excellent basis for two-particle system, but has severe limitations when we want to consider a many-particle system. The Moshinsky transformation coefficients [Moshinsky; 1959] are used to transform our system from the center-of-mass and relative basis to the more appropriate laboratory basis. OSMC is then introduced and diagonalization results for four, six and eight particles are listed and discussed.

Concluding remarks and suggestions for future work are given in Chapter 6. Most calculations are done in the Appendix to minimize the number of equations inside the chapters.

# Acknowledgments

I would like to thank my supervisor Morten Hjorth-Jensen for his everlasting encouragement and help throughout this thesis. Torgeir Engeland's contributions were also invaluable. I would also like to thank Simen Kvaal for his proofreading of this thesis.

Espen Flage-Larsen

# Chapter 1

## Introduction

This chapter gives a non-theoretical introduction to the subject of quantum dots. In the first section we will try to motivate readers by explaining why the quantum dots are important. The next section gives a short historical overview.

### 1.1 Why are quantum dots important?

During the recent years, the microchip manufactures have reached a point where they in principle could create structures atom by atom. A whole new world of physics have revealed itself in the process and the need for knowledge about these systems have become critical, both theoretically and experimentally. This evolution has been driven by both scientists and consumers as a consequence of the need for smaller and smaller electronic devices. As the size shrinks one will eventually enter the quantum regime where circuits can no longer be made using conventional techniques due to quantum effects. The main idea in conventional circuits [Millman and Grabel; 1987] is to create a system that can handle voltage differences, controlled by some external device. To manufacture a device far into the quantum regime needs radical thinking. A quantum dot, which traps electrons could eventually see applications in electronics by manipulating electron states rather than voltages to form what is commonly referred to as quantum bits, or qubits [van der Wiel et al.; 2006].

In addition, the quantum dots could also be used to absorb and emit light efficiently at any wavelength, thus forming new kinds of lighting and improving the current laser technologies. Another problem with conventional lasers is the need for cooling and that the pulses are relatively slow. By the use of quantum dots all these parameters could be improved. There is also the possibility of producing efficient white light, see [II et al.; 2005] for details.

The applications discussed above are of a more practical approach. However, the puzzle of the atomic spectra was a prime motivation for the development of quantum mechanics and the quantum dots makes it possible to create artificial atoms, see Chapter 2 for a brief explanation of an artificial atom. Investigating many-electron interactions in an atom is difficult due to the interactions with the nucleus, but in



quantum dots, artificial atoms can be created without the presence of a nucleus. The quantum dot hence serves as an excellent breeding ground for electron cloud studies. Even artificial molecules can be made by combining several many-particle quantum dots. Another exciting property of quantum dots is the possibility to manipulate the geometry of the confinement, thus making potentials not seen in any atom. These new fields of research have emerged during the last ten years, but much remains to be done. In the next section we will briefly cover the historical evolution of the quantum dot.

## 1.2 Historical notes about the evolution of quantum dots

The era of quantum dots started about fifty years ago. Thin layers of materials used as a confinement for quantum mechanical studies was introduced in the late 1950s and early 1960s. However, most of the work during the early days was theoretical due to the insufficient technology and funds available at that time. During the 1960s novel techniques called epitaxial depositions [Heinzel; 2003] was developed. As a consequence it was possible to build ultra-clean composite layers of semiconductor materials, mainly gallium arsenide and aluminum gallium arsenide. One of the first structures developed in the early 1970s was the quantum well [Chang et al.; 1974, Dingle et al.; 1974], where electrons was confined in a thin layer of semiconductor material sandwiched between two layers of another semiconductor material. Impressive results arose from optical studies of these quantum wells and one could clearly observe a two-dimensional character of the sample.

At the beginning of the 1980s, there was a rapid progress in technology and accurate lithography techniques was put to use, see Sec. 2.1.1 for details. A quasi-one-dimensional quantum wire [Petroff et al.; 1982] was made using a lithography process. As the lithography techniques was limited compared to todays standards the width of the wire was typically much wider than the depth. In the middle of the 1980s one of the first methods for making quantum dots was developed. This was based on an etching technique [Reed et al.; 1986], where substrates where etched to create confining dots. As a consequence a complete quantization of the electron free motion was possible. During the late 1980s and 1990s these methods evolved into what they are today. Lithography and etching is still used, but instead of light lithography, electron or ion lithography is used to increase precision. In recent years carbon nanotubes [Harris; 2002] have become very popular due to their promising features. They have high electrical conductivity combined with light weight and high tensile strength. However, as of today, their manufacture process is unstable and the cost of carbon is high.

## Chapter 2

# Properties of quantum dots

In this section we will give an overview of the typical quantum dot. The term quantum dot is rather vague, but it is often characterized as a conducting island with its carrier motion size comparable to the de Broglie wavelength [Brehm and Mullin; 1989]. Usually this island is residence to a given number of electrons. The similarities between quantum dots and atoms are present, but there are significant differences. First of all, the length scales in quantum dots are different from any atom. A quantum dot has a typical length scale of about 100 nm, while atoms are smaller, ranging from about 0.05 nm to 0.4 nm. Secondly, the confining forces are different. In atoms, the attractive force is set up by the nucleus. However, in quantum dots we typically have some external field or potential confining the particles. As a consequence of the length scale, the energy scale is also different. Typical values for atoms and quantum dots are listed in Table 2.1. The magnetic field listed is the strength needed to break the energy structure of the dot or the atom, while the energy excitation tells us how much energy is needed to excite each system. The values listed are by no means intended to be taken too seriously, they are listed so that the typical differences are illustrated. Each system has its extremes. In spite of the difference, quantum dots are often called

	Quantum dot	Atom
Size	100nm	0.1nm
Excitation energy	0.1meV	10eV
Magnetic field	10T	10000T

**Table 2.1:** Typical difference between an atom and a quantum dot. The magnetic field strength listed is the strength needed to break the energy levels. For the atom, we need a very large magnetic field. It is not possible to generate this magnetic field in a laboratory. However, the magnetic field needed to break the energy levels in the quantum dot can be produced at a proper test facility.

artificial atoms. The difference lies more or less in the scaling and one can easily draw parallels between their inner workings. Quantum dots experience energy bands and excitation in energy just like the atoms. They even exhibit magic numbers and a shell structure seen in atoms, although with different values. By controlling the external potential we can determine the number of electrons which populates the quantum dot.

In principle a periodic table for quantum dots can be built by utilizing this.

We will now briefly discuss different manufacturing techniques and the description of Coulomb blockage. Readers are free to skip the following sections and jump directly to Chapter 3 if they do not find this useful. However, the physics covered is not found elsewhere in the thesis. The following sections will also explain the two most frequently used quantum dots. For the curious reader references are given to even more promising devices.

## 2.1 Structure, manufacture and operational principle

Making quantum dots involves a complicated manufacture process. One typically needs high precision, high material purity and a sophisticated controlling device. The common etching method today is more or less the same as developed during the 1980s [Reed et al.; 1986], but the quality of the samples are far better as a consequence of more sophisticated manufacturing equipment. The shape and operation principle is different from design to design, but they all need to be produced on a small scale, typically 10-100 nm to yield size quantization. Common semiconductor materials are normally used. Gallium arsenide (GaAs) is preferred over silicon (Si) due to its electrical properties. GaAs has higher electron mobility, lower breakdown voltages and less noise. As a consequence GaAs samples can be made smaller. However silicon is available from quartz which is found in large quantities on earth. Hence it is cheap to produce silicon. Silicon also bonds with oxides without problems, and  $\text{SiO}_2$  makes an excellent insulator. In addition, mobility is greater in silicon than in gallium arsenide. This gives silicon an advantage over gallium arsenide in logical circuits, due to the potential higher speed of a silicon p-channel transistor. When you want to manufacture quantum dots mainly for measurements and research, size and error considerations are more important than cost and speed. To make an insulator, gallium arsenide can be combined with aluminum or aluminum arsenide (AlAs).

Several methods and designs are available when one wants to make a quantum dot. The objective is the same for all, which is to confine electrons. Manufacturing is not the main topic in this thesis and we will just outline some of the techniques. The two most important utilize either physical bounds or electrical fields to confine the electrons. Both methods give rise to size quantizations.

### 2.1.1 Electron confinement using physical boundaries

To make a quantum dot which is physically restricted in spatial dimensions, we usually use etching. As we have mentioned before, this technique was developed during the middle 80s. To prepare the sample for etching one uses lithography. A basic process for making several small transistors and connect them is illustrated in Fig. 2.1.1. This process serves as an analogy to what goes on during the manufacturing of quantum dots using lithography and etching. However, since we need far better precision, electron or ion beam lithography is often used instead of light lithography. The first step in the manufacture process is to obtain a prepared wafer of silicon or gallium arsenide. The

making of the wafers are dependent on what characteristics you want. Fig. 2.1.2.2(a) shows a typical wafer prepared for a quantum dot application. The bottom layer of GaAs is doped to work as a reservoir. Then follows a layer of AlGaAs which acts as a potential barrier to isolate the next GaAs layer by tunneling. The top layer of Au works as an electrode. Because of the potential difference between GaAs and AlGaAs this wafer traps electrons in the middle GaAs layer. If we make the two barriers different in such a way that electrons can tunnel over one of the barriers but not the other, we can control the electron flow on and off the isolated layer in between. The wafer is layered with a mask on top. By using electron beam lithography a pattern is made in the mask. We then expose the sample for an etching solution that only etch areas not protected by the mask. Finally we deposit ions to dope the material exposed, or we add a suitable metal. The metal can for example function as an electrode. In the end we are left with a small sized confinement as in Fig. 2.1.2.2(b). By applying a potential difference between the electrode and the reservoir, the population of electrons inside the middle GaAs layer can be controlled. The form of these quantum dots can vary from design to design, but the principles are the same.

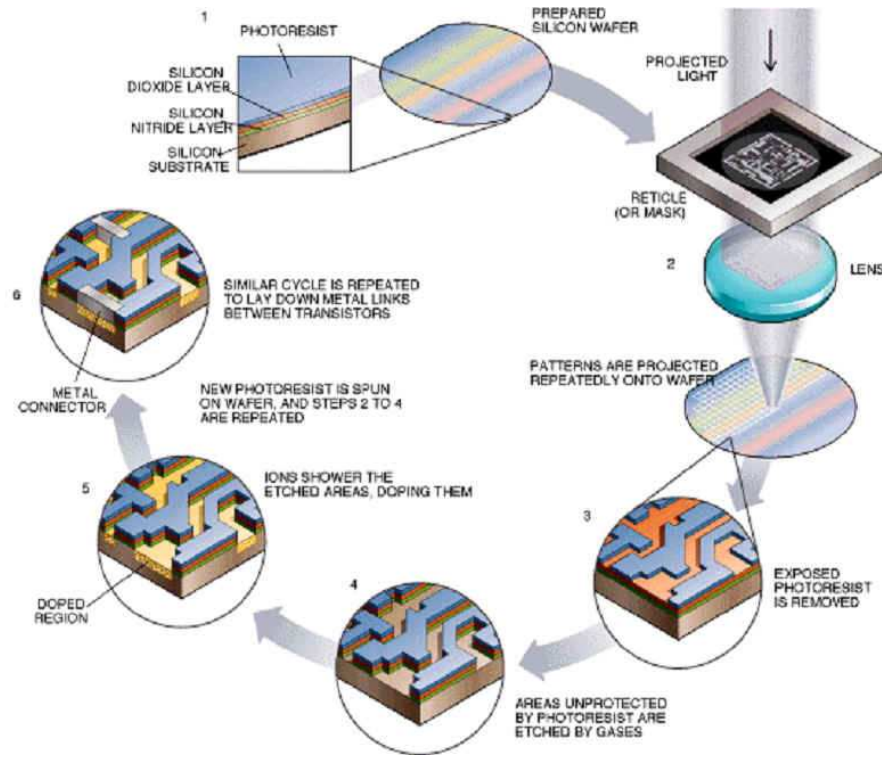


**Figure 2.1.1:** Light lithography used to create advanced integrated circuits.

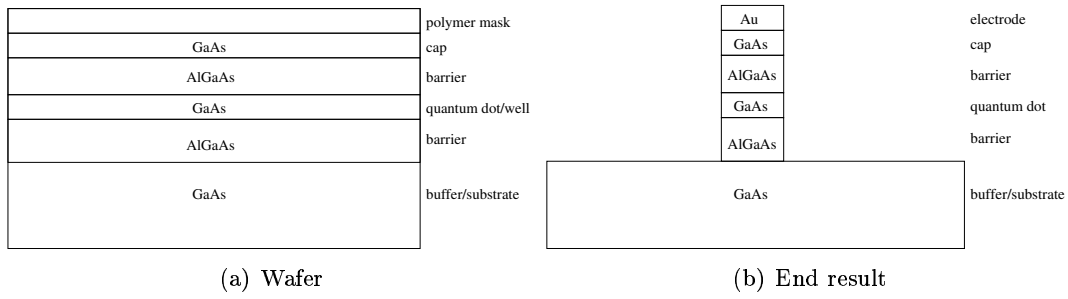


**Figure 2.1.2:** Layers in GaAs quantum dot sample. The figure to the left is an illustration of a typical wafer before etching. The middle GaAs layer will work as a confinement due to the insulators. The end result after lithography and etching is shown in the figure to the right. The confinement is now restricted by the spatial extension of the middle GaAs layer and the potential applied between the buffer and the electrode at the top.

### 2.1.2 Electron confinement using electrical fields

The etching technique is a one-way process and if we need to change some variable in the produced dot, other than the potential difference between the reservoir and the electrode, we need to manufacture a new sample. This can be time consuming and expensive. We also introduce deviations in the sample specifications as the manufacture process cannot produce the exact same sample twice. A more flexible method is to use lithography on a substrate to form electrical gates which can be tuned to give the desired confinement parameters. One example of this is shown in Fig. 2.1.3. Here lithography is used to carve out the conductors on top of a GaAlAs layer covered with a mask. We then deposit a metal on top of it, usually gold. By applying potential difference between the finger gate and  $Q_1$  and  $Q_2$  we form what is called QPC (Quantum Point Contact) which regulates the population of the confinement between the barriers by tunneling. We can then regulate the potential on the center gate to give desired geometric properties of the confinement. For readers familiar with transistors, we then get source and drain on each side of the QPCs. By using electrical fields as confinement we have greater flexibility and properties of the sample can be varied accordingly. Another important feature is that we have no, or very little, edge effects compared to the physical confinement discussed in the previous section.

There are other methods developed, but the two explained above are mostly used. For the curious reader we should mention selective growth [Fukui et al.; 1991, Lebens et al.; 1990] and microcrystal semiconductors [Ekimov et al.; 1985] as alternatives. Another method is self-assembled dots [Marzin et al.; 1994, Raymond et al.; 1996], which is promising due to their small confinement size.

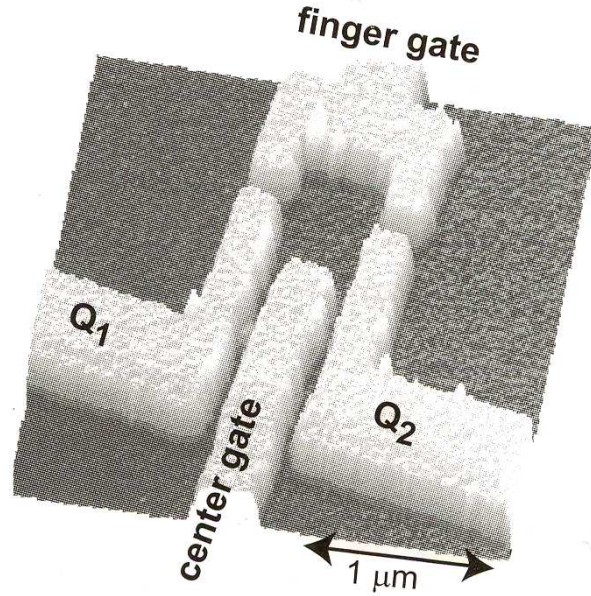


**Figure 2.1.3:** Typical quantum dot layout. A potential is applied between the finger gate and the gates  $Q_1$  and  $Q_2$ . This creates tunneling barriers restricting the flow of electrons on and of the island. The confining island is the square between all gates. The center gate can be used to modify the geometrical properties of the confinement. From [Heinzel; 2003]

## 2.2 Charge quantization and Coulomb blockage

In addition to size quantization we also have what is called charge quantization. Recall the capacitor, where one defines the capacitance  $C$  as the difference between the charges  $q$  and the potential  $V$  between two charge carriers separated in space, that is  $C = q/V$ . The energy stored in a capacitor is defined as  $E = q^2/2C$ .

By making the distance between the carriers small, it will act as a tunnel junction and the charge transfer between the carriers becomes quantized. This mechanism is called Coulomb blockage. To illustrate the Coulomb blockage model, let us look at Fig. 2.1.3. The island is isolated between two QPCs, which work as tunneling barriers. We can now think of the island and the two QPCs as a quantized capacitor. This is an approximation since we have completely disregarded the Pauli exclusion principle, which also adds to the energy difference. See Sec. 5.1 for details about the Pauli principle. The potential difference  $V_g$  between the two gates is a bit more complex than in a standard capacitor, due to the presence of several gates. As an approximation we can disregard these effects. If we add a charge  $q$  to the island, the change in energy would be

$$\Delta E = qV_g + \frac{q^2}{2C}, \quad (2.2.1)$$

where the first term accounts for the work involved due to the potential field, while

the second is the energy coming from the Coulomb repulsion of the capacitor. The electron(s) is(are) responsible for the charge transfer. For  $N$  electrons with charge  $-e$  we have that  $q = -Ne$ . This gives the energy difference as

$$\Delta E(N) = -NeV_g + N^2 \frac{e^2}{2C}. \quad (2.2.2)$$

The change in energy from an  $N + 1$  electron to an  $N$  electron charged island is given as

$$\Delta E(N + 1) - \Delta E(N) = -eV_g + \left(\frac{1}{2} + N\right) \frac{e^2}{C}. \quad (2.2.3)$$

When the energy difference vanishes, the electrons can be transferred on and off the island. This happens when the gate potential is

$$V_g = \left(\frac{1}{2} + N\right) \frac{e}{C}. \quad (2.2.4)$$

This gives rise to a special property which controls current flow through the islands of quantum dots. A plot of the conductance as a function of gate potential is shown in Fig. 2.2.4. We see that Coulomb blockage occurs between the peaks. However, if

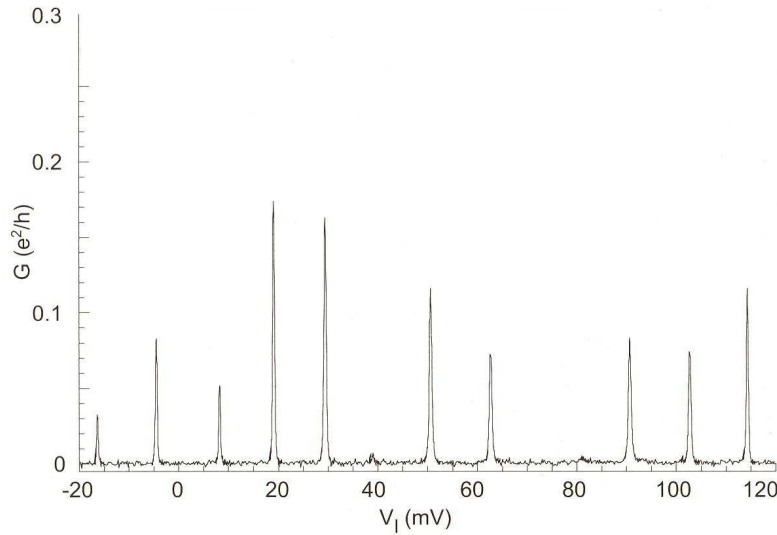


**Figure 2.2.4:** Conductance through a typical quantum dot as a function of the gate potential. We clearly see that current mostly flows at certain discretized gate potentials. Filtering devices are used to filter out noise from other physical processes. From [Heinzel; 2003].

we measure the conductance of a typical quantum dot without any kind of filtering device we would observe more noise and imperfection than what is shown in Fig. 2.2.4. Typically one would have main peaks which arise due to Coulomb blockage and noise which arises due to size quantization. Also, when the gate potential increases we see a diminishing distance between the conductance peaks. One explanation for this is that the dot increases in size, approaching the electrodes which increases conductance. The first peak can be the first electron on the dot, but it can also be the tenth. It depends

on how we have tuned the tunnel barriers. When the barriers are sufficiently close to the confining center for tunneling to happen, we normally see the first electron in the leftmost peak. If the distance is larger, we need to increase the radius of the electron cloud sitting in the center of the confinement. Since electrons repel each other, each time we add an electron, the size of the confined cloud increases and the distance to the tunnel barriers decrease accordingly. It should be noted that the Coulomb blocking is a purely classical effect, but it is affected by the quantum effects at the QPCs.

Observing Coulomb blockage in real life is not easy. First of all, the resistance in the QPC need to be sufficiently large. We need to observe single electrons tunneling through the QPC. This means, that the tunneling event time  $dt$  need to be significantly larger than the tunneling time  $\tau$ . The tunneling time has been estimated as  $\tau = \hbar/eV$  [Ratner; 1997]. We will now estimate the order of resistance needed. Using Ohm's law

$$V = RI, \quad (2.2.5)$$

where  $V$  is the voltage over a resistance  $R$ . The current  $I$  is defined as  $dq/dt$ . Substituting this into the Ohm's law yields

$$dt = \frac{Rdq}{V}. \quad (2.2.6)$$

The difference in charge is  $e$ , so a crude approximation for the tunneling event time can be written as

$$dt \approx \frac{eR}{V}. \quad (2.2.7)$$

To observe a single electron transfer we would like to have  $dt \gg \tau$ , that is

$$R \gg \frac{\hbar}{e^2}. \quad (2.2.8)$$

The term  $\hbar/e^2$  can be located in experimental physics tables, such as [Mohr and Taylor; 2006]. It is approximately 4 k $\Omega$ . Since an increase in temperature adds more thermal fluctuations, the width of the peaks are directly related to the temperature of the sample. As a consequence the temperature is an important aspect. If the operational temperature is too high, we can have thermal fluctuations giving rise to unwanted excitations. Since we need a large tunnel resistor we quickly run into practical problems with cooling. Today, these limitations are seldom a problem and quantum dots made out of silicon are able to operate at room temperature.

In most experimental situations the electrons in quantum dots are manipulated by an external magnetic field. This field is usually manipulated such that the magnetic field vector  $\vec{B}$  is normal to the dot surface. For a typical quantum dot this results in a complicated spectrum of energy levels shown in Fig. 2.2.5. Trying to understand the figure without a theoretical model would be pure guesswork and the main topic of the next chapter is to give a theoretical approach to the quantum dot. A complete model of quantum dots would be utterly impossible to develop in this thesis, but we will start slow and simple, expanding the theory as needed.



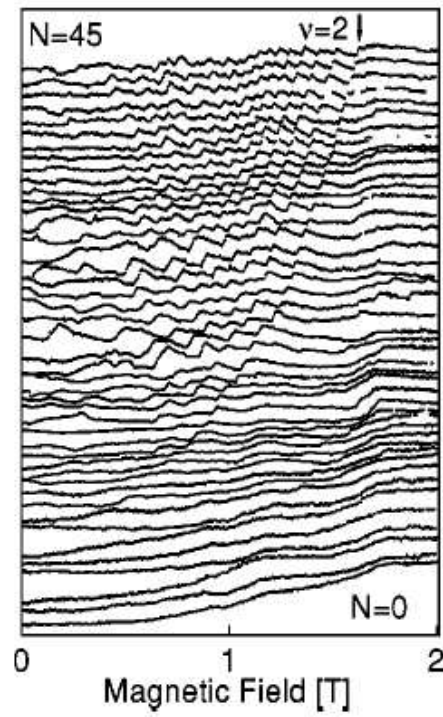


**Figure 2.2.5:** Energy as a function of magnetic field along normal plane of a quantum dot. These are typical experimental values. From [Ciorga et al.; 2000].

## Chapter 3

# Theoretical approximations to quantum dots

In this chapter we aim at developing a theoretical framework for describing the effects seen in quantum dots. Quantum dots are complex devices. It is not easy to give a simple yet complete theoretical model. Effects of electron-electron interactions, the Pauli exclusion principle, edge effects and external fields all need to be accounted for. For a two-electron quantum dot, we only need to add the electron-electron interaction in addition to the effects mentioned above. But as the electron number increases, many-body interactions occur and the complexity increases drastically. In this thesis we completely disregard edge effects. A common approximation for quantum dots is to reduce the spatial dimensions from three to two, where the third dimension is fixed by a manufacture technique, see Sec. 2.1 for details. In this thesis we try to compare the two and three dimensional results where possible. In both two and three dimensions we will be using a harmonic oscillator confinement. Ideally this harmonic confinement will be a potential of the form

$$V(x, y, z) \propto ax^2 + by^2 + cz^2, \quad (3.0.1)$$

which gives rise to a bowl shaped potential which can be tuned by varying  $a$ ,  $b$  and  $c$ . But to simplify calculation and obtain analytic solutions we will use a spherical symmetric potential, where  $a = b = c$  for three dimensions and  $a = b$ ,  $c = 0$  for two dimensions. This chapter starts by developing a theory for the single electron quantum dot. Following is a discussion of the two electron dot. This chapter is essential to the future work of this thesis.

### 3.1 Single electron quantum dot

Let us now look at a single electron quantum dot confined by a harmonic oscillator potential. We make restrictions in the x-y directions, while we fix the third dimension. To follow experiments we will include a constant magnetic field along the third axis. As mentioned we only consider spherically symmetric harmonic confinement. The mass

of the electrons will be labeled  $m^*$  to avoid confusion with quantum numbers. In solid states like silicon and gallium arsenide the effective electron mass will be different from the bare mass, thus its also natural to avoid using  $m$ , which readers might misinterpret as the bare mass. This effective mass can be determined as long as we have the full energy of the system. The two dimensional quantum dot is considered first, then the three dimensional one.

### 3.1.1 Two dimensions

The two dimensional Hamiltonian for non-interacting electrons confined in a harmonic oscillator potential is given as

$$H = \sum_{i=1}^N \left( \frac{\vec{p}_i^2}{2m^*} + \frac{1}{2}m^*\omega_0^2(x_i^2 + y_i^2) \right), \quad (3.1.1)$$

where  $N$  is the electron number,  $m^*$  the effective electron mass and  $\vec{p}_i$  the  $i$ 'th electron's momentum. The coordinates are given as  $x_i$  and  $y_i$ . By introducing a external vector field  $\vec{A}$  we get a modified Hamiltonian

$$H = \sum_{i=1}^N \left( \frac{1}{2m^*}(\vec{p}_i + \frac{e}{c}\vec{A}_i)^2 + \frac{1}{2}m^*\omega_0^2(x_i^2 + y_i^2) + e\phi + \vec{\rho}_i \cdot \vec{B} \right). \quad (3.1.2)$$

In addition to the added vector potential, we get a contribution from the electrical potential  $\phi$  and the magnetic field  $\vec{B}$ . The electron charge is given as  $e$ . The magnetic moment  $\vec{\rho}$  is introduced due to the spin coupling with the magnetic field. The magnetic moment is defined as  $\vec{\rho} = q\vec{L}/2m$  [Shankar; 1994]. However, since it is the electron spin that couples, we write  $\vec{\rho} = -eg\vec{S}/2m^*c$ , where  $g$  is the Landé g-factor. Its value is  $g \approx 2$ , more correct values can be located in tables of particle physics, see for example [Mohr and Taylor; 2006]. The two last terms in the Hamiltonian in Eq. (3.1.2) are scalars when expectation values are calculated, they can thus be taken outside and disregarded during calculations. We can reintroduce them in the final result if we want. We also see that Eq. (3.1.2) is separable in the single electron Hamiltonians as the total Hamiltonian only acts on single electrons. Without the scalar terms Eq. (3.1.2) becomes

$$H = \frac{1}{2m^*}(\vec{p} + \frac{e}{c}\vec{A})^2 + \frac{1}{2}m^*\omega_0^2(x^2 + y^2), \quad (3.1.3)$$

for the single electron. Expanding the first term gives

$$(\vec{p} + \frac{e}{c}\vec{A})^2 = p^2 + \frac{e}{c}(\vec{p} \cdot \vec{A} + \vec{A} \cdot \vec{p}) + \frac{e^2}{c^2}A^2. \quad (3.1.4)$$

The momentum and the vector fields do not commute in general. However, by selecting a proper gauge they can be shown to commute. See App. A.2 for further details. Since we only want a constant magnetic field along the z-axis we choose the vector field  $\vec{A}$  as

$$\vec{A} = \frac{B}{2}(-y, x, 0), \quad (3.1.5)$$

where  $B$  now is the amplitude of the applied magnetic field. By Maxwell's equations [Goldstein et al.; 2002] we have

$$\vec{B} = \nabla \times \vec{A}, \quad (3.1.6)$$

which gives for the chosen  $\vec{A}$

$$\vec{B} = B\vec{e}_z. \quad (3.1.7)$$

We see that  $\vec{A}$  is indeed a valid choice, giving rise to a constant magnetic field along the third axis. Substituting the vector field from Eq. (3.1.5) into Eq. (3.1.4) yields

$$(\vec{p} + \frac{e}{c}\vec{A})^2 = p^2 + \frac{eB}{c}(xp_y - yp_x) + \frac{e^2 B^2}{4c^2}(x^2 + y^2). \quad (3.1.8)$$

As a consequence of the Coulomb gauge,  $\vec{p}$  and  $\vec{A}$  commute. Substituting this back into Eq. (3.1.3) gives

$$H = \frac{1}{2m^*} \left( p^2 + \frac{eB}{c}(xp_y - yp_x) + \frac{e^2 B^2}{4c^2}(x^2 + y^2) \right) + \frac{1}{2}m^*\omega_0^2(x^2 + y^2), \quad (3.1.9)$$

where the second term in the first bracket can be associated with the third component of the angular momentum, see App. A.3 for details. Defining

$$\omega_B = \frac{eB}{2m^*c}, \quad (3.1.10)$$

and

$$\omega^2 = \omega_0^2 + \omega_B^2, \quad (3.1.11)$$

together with the substitution  $p \rightarrow -i\hbar\nabla$ , we get a more compact notation of the Hamiltonian as

$$H = -\frac{1}{2m^*} \left( \hbar^2 \nabla^2 + \frac{ie\hbar B}{c} \left( x \frac{\partial}{\partial y} - y \frac{\partial}{\partial x} \right) \right) + \frac{1}{2}m^*\omega^2(x^2 + y^2). \quad (3.1.12)$$

To simplify calculation we now transform the Hamiltonian to polar coordinates  $r$  and  $\theta$ . Details for the transformations are given in App. A.3. After the transformations are done, Eq. (3.1.12) reads

$$H = -\frac{\hbar^2}{2m^*} \left( \frac{\partial^2}{\partial r^2} + \frac{1}{r} \frac{\partial}{\partial r} + \frac{1}{r^2} \frac{\partial^2}{\partial \theta^2} + i \frac{eB}{\hbar c} \frac{\partial}{\partial \theta} \right) + \frac{1}{2}m^*\omega^2 r^2. \quad (3.1.13)$$

At first sight changing to polar coordinates  $r$  and  $\theta$  seems more complicated, but it is not. By doing this, we will end up solving a rather simple second order differential equation. With the Hamiltonian in Eq. (3.1.13), the Schrödinger equation becomes

$$-\frac{\hbar^2}{2m^*} \left( \frac{\partial^2}{\partial r^2} + \frac{1}{r} \frac{\partial}{\partial r} + \frac{1}{r^2} \frac{\partial^2}{\partial \theta^2} + i \frac{eB}{\hbar c} \frac{\partial}{\partial \theta} \right) \Psi(r, \theta) + \frac{1}{2}m^*\omega^2 r^2 \Psi(r, \theta) = E \Psi(r, \theta). \quad (3.1.14)$$

This equation is separable in  $r$  and  $\theta$  as

$$\Psi(r, \theta) = e^{im\theta} \psi(r), \quad (3.1.15)$$

where  $m$  takes certain values, since we demand a continuity of  $\Psi(r, \theta)$ . This restricts  $m$  to the values  $m = 0, \pm 1, \pm 2, \dots$ . Substituting Eq. (3.1.15) into Eq. (3.1.14) yields

$$-\frac{\hbar^2}{2m^*} \left( \frac{\partial^2}{\partial r^2} + \frac{1}{r} \frac{\partial}{\partial r} - \frac{m^2}{r^2} - \frac{emB}{\hbar c} \right) \psi(r) + \frac{1}{2} m^* \omega^2 r^2 \psi(r) = E \psi(r), \quad (3.1.16)$$

where the eigenvectors  $\psi(r)$  are given as

$$\psi(r)_{nm} = \sqrt{\frac{2n!}{(n+|m|)!}} \beta^{(|m|+1)/2} r^{|m|} e^{-\beta r^2/2} L_n^{|m|}(\beta r^2), \quad (3.1.17)$$

with corresponding eigenvalues

$$E = (2n + |m| + 1) \hbar \omega + m \hbar \omega_B, \quad (3.1.18)$$

where

$$\beta = \frac{m^* \omega}{\hbar}. \quad (3.1.19)$$

The  $L_n^{|m|}(\beta r^2)$  is the associated Laguerre polynomial. See App. A.7.1 for the derivation of the eigensolutions in Eqs. (3.1.17) and (3.1.18). Definition of the associated Laguerre polynomials are also given in App. A.7.1. The radial eigenvectors in Eq. (3.1.17) are normalized. However, we also need to normalize the angle dependent part of the total eigenvector defined in Eq. (3.1.15). This is rather easy and the total eigenvector is written as

$$\Psi_{nm}(r, \theta) = \sqrt{\frac{n!}{\pi(n+|m|)!}} \beta^{(|m|+1)/2} r^{|m|} e^{-\beta r^2/2} L_n^{|m|}(\beta r^2) e^{im\theta}. \quad (3.1.20)$$

Using Eq. (3.1.11) we can rewrite Eq. (3.1.18) as

$$\frac{E}{\hbar \omega_0} = (2n + |m| + 1) \sqrt{1 + \frac{\omega_B^2}{\omega_0^2}} + m \frac{\omega_B}{\omega_0}. \quad (3.1.21)$$

This equation gives rise to the Fock-Darwin energy spectrum shown in Fig. 3.1.1. At,  $\omega_B = 0$  ( $B = 0$ ), the eigenvalues are given as

$$E^{B=0} = (2n + |m| + 1) \hbar \omega_0, \quad (3.1.22)$$

with degeneracy of  $d = 2n + |m| + 1$ . By defining a new quantum number,  $N = 2n + |m|$  it is possible to develop the shell fillings shown in Table 3.1. Remember that due to the electron spin degeneracy we have a factor two multiplied to the previous mentioned degeneracy. This is due to the Pauli principle, see Sec. 5.1 for details. The total degeneracy can then be defined as  $D = 2d$ . This extra degeneracy is not shown in Fig. 3.1.1 since we excluded the electron spin coupling in the energy term from Eq. (3.1.18). In Fig. 3.1.1 the plotted lines seem to gather in bands as  $\omega_B \rightarrow \infty$ . These bands are often referred to as Landau bands or levels, see standard textbooks in quantum mechanics, such as [Shankar; 1994] for details. In the large field limit,

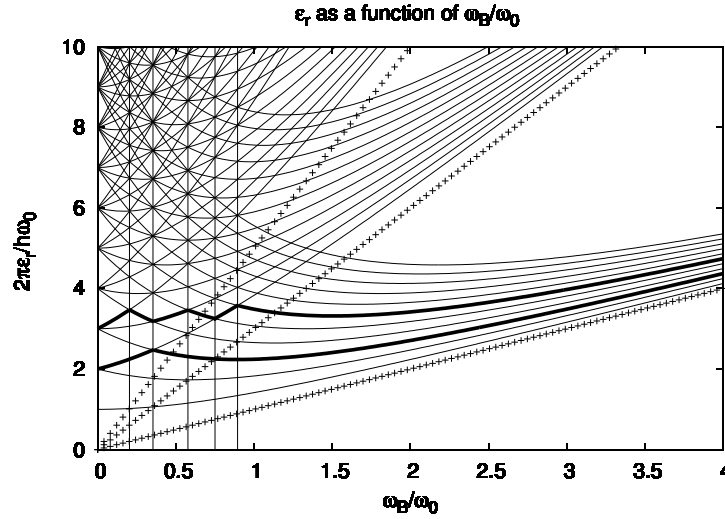


**Figure 3.1.1:** The two dimensional Fock-Darwin energy spectrum for a single electron quantum dot. Landau levels are clearly visible at the far right in the figure. Observe the thick lines as they represent a particle in shells  $S = 6$  and  $S = 12$  from Table 3.1. The plussed lines are the eigenvalues obtained when  $\omega_B \rightarrow \infty$ . One clearly see that the levels converge to the high field limits and form Landau bands as  $\omega_B$  increases. A degenerate state at  $\omega_B = 0$  is split as  $\omega_B$  is increasing due to the  $m\hbar\omega_B$  energy term. But suddenly accidental degeneracy occur and the electron chooses the states which is most favorable. Hence the zig-zag lines.

where  $\omega_B \rightarrow \infty$  we get the energy levels

$$E^{B \rightarrow \infty} \approx (2n + |m| + m + 1)\hbar\omega_B. \quad (3.1.23)$$

Observe that we have two cases, one for  $m \geq 0$  and one for  $m < 0$ . In the first case, the energy is given as

$$E^{B \rightarrow \infty} \approx (2(n + m) + 1)\hbar\omega_B, \quad (3.1.24)$$

while in the second case, the  $m$  terms cancel and we are left with

$$E^{B \rightarrow \infty} \approx (2n + 1)\hbar\omega_B. \quad (3.1.25)$$

By defining the Landau band quantum number  $N_L = 0, 1, 2, \dots$  we can write the high field approximation as

$$\frac{E^{B \rightarrow \infty}}{\hbar\omega_0} \approx (2N_L + 1) \frac{\omega_B}{\omega_0}. \quad (3.1.26)$$

These energy lines are shown in Fig. 3.1.1 as lines with pluses for  $N_L = 0, 1, 2$ . We clearly see that as the magnetic field is increased, the Fock-Darwin spectrum converges to the high field limit forming Landau levels, or Landau bands. The intersection points are highlighted using vertical lines in Fig. 3.1.1. They will appear where the ratio of the energy difference between two Landau levels and sublevels is an integer. In Fig. 3.1.1 we have only calculated and drawn a limited number of Landau bands, but it is enough to illustrate what will happen to an energy level when the magnetic field is increased.

N	D=2d	Shell filling=S
0	2	2
1	4	6
2	6	12
3	8	20

**Table 3.1:** Two dimensional quantum numbers and shell filling for a quantum dot without electron-electron interaction. The shell filling factor tells us how many electrons there is in the dot, up to the given state  $N$

At  $\omega_B = 0$  the levels are degenerate. Increasing  $\omega_B$  increases or decreases the energy of the electron depending on the choice of  $m$ . The degenerate states will separate due to the  $m\hbar\omega_B$  term. Suddenly accidental degeneracies occur and the electron chooses the state which is most favorable in energy. We then get the zig-zag lines indicated in Fig 3.1.1. They are very important and show up in experiments. They can to some extent predict the noise in conductance peaks mentioned in Sec. 2.2, but it is by no means a perfect model. Each line in Fig. 3.1.1 is degenerate as a consequence of disregarding the electron spin. Including this would break the spin degeneracy and split one line into two, thus revealing an even more complicated energy spectra. We can relate the two bold lines in Fig. 3.1.1 to filled shells, for  $S = 6$  and  $S = 12$  particles. When the quantum dot is in a filled shell state, we need to add energy to open up a new shell, and place electrons such that they obey the Pauli principle. It takes much less energy to add an electron to an already open shell. From Fig. 2.2.5 we can see similarities, however deviations are clearly visible. This should not come as a surprise, since it is a simplified model where the electron-electron interaction is left out.

In the beginning of this section we disregarded some constant terms to simplify calculations. Since we have set  $\vec{E} = \vec{0}$ , the term left out takes care of the energy difference due to the coupling between the electron spin and the magnetic field. Including this term the energy in Eq. (3.1.18) gives,

$$E = (2n + |m| + 1)\hbar\omega + m\hbar\omega_B + gs\frac{m^*}{\mu}\hbar\omega_B, \quad (3.1.27)$$

where  $\mu$  is the bare electron mass. The factor  $g$  is the familiar Landé factor,  $g \approx 2$ . The electron spin  $s$  can take half integer values,  $s = \pm 1/2$ .

In experiments it is almost impossible to completely fix one dimension and realistic quantum dots operates in three dimensions. Let us now look at the three dimensional quantum dot and how it relates to the previous discussions in two dimensions.

### 3.1.2 Three dimensions

The discussion of a non-interacting three dimensional quantum dot follows Sec. 3.1.1 until we write out the Hamiltonian in Eq. (3.1.12). The only difference is that we get an extra  $z^2$  term from the harmonic oscillator potential. This modified Hamiltonian

reads

$$H = -\frac{1}{2m^*} \left( \hbar^2 \nabla^2 + \frac{ie\hbar B}{c} \left( x \frac{\partial}{\partial y} + y \frac{\partial}{\partial x} \right) \right) + \frac{1}{2} m^* \omega^2 (x^2 + y^2 + z^2). \quad (3.1.28)$$

If we did not have the  $z$ -component due to the harmonic confinement, the only  $z$  dependent term would be  $p_z$ . We could then separate the Schrödinger equation in  $z$  and  $(x, y)$ . This is not the case here, since  $p_z$  and  $z$  do not commute. Just like for two dimensions we now transform the Hamiltonian into polar coordinates. How the  $\nabla^2$  operator and the derivatives transform is given in App. A.3. Transforming Eq. (3.1.28) into spherical polar coordinates yields

$$H = -\frac{1}{2m^*} \left\{ \hbar^2 \left( \frac{\partial^2}{\partial r^2} + \frac{2}{r} \frac{\partial}{\partial r} + \frac{1}{r^2} \left[ \frac{1}{\sin^2(\phi)} \frac{\partial^2}{\partial \theta^2} + \cot(\phi) \frac{\partial}{\partial \phi} + \frac{\partial^2}{\partial \phi^2} \right] \right) + \frac{ie\hbar B}{c} \frac{\partial}{\partial \theta} \right\} + \frac{1}{2} m^* \omega^2 r^2. \quad (3.1.29)$$

We observe that the angle dependent part in the bracket is the  $L^2$  operator while the derivative of  $\theta$  is related to  $L_z$ , see App. A.3 for details. From the Schrödinger equation

$$H\Psi = E\Psi, \quad (3.1.30)$$

we can assume

$$\Psi(r, \theta, \phi) = \psi(r) \Omega(\theta, \phi). \quad (3.1.31)$$

The eigensolutions of the angle dependent part are worked out in standard textbooks in quantum mechanics, see for example [Shankar; 1994]. The eigenvalues of  $L_z$  and  $L^2$  are shown to be

$$L^2 \Omega(\theta, \phi) = \hbar^2 l(l+1) \Omega(\theta, \phi), \quad (3.1.32)$$

$$L_z \Omega(\theta, \phi) = m\hbar \Omega(\theta, \phi), \quad (3.1.33)$$

where  $l = 0, 1, 2, \dots$  and  $m = 0, \pm 1, \pm 2, \dots$ . The normalized spherical eigenvectors  $\Omega(\theta, \phi)$  are written as

$$\Omega(\theta, \phi)_{lm} = \alpha_m \sqrt{\frac{(2l+1)(l+|m|)!}{4\pi(l-|m|)!}} P_l^{|m|}(\cos(\theta)) e^{im\phi}, \quad (3.1.34)$$

with the definition

$$\alpha_m = \begin{cases} 1 & m \leq 0 \\ (-1)^m & m \geq 0 \end{cases} \quad (3.1.35)$$

In the derivation the constraint  $|m| \leq l$  has to be used to obtain valid solutions. The Legendre polynomials  $P_l^{|m|}(x)$  are tabulated in [Abramowitz and Stegun; 1972]. The first few are listed in Table 3.2. The Legendre polynomials are defined in the Rodrigues representation as

$$P_l^{|m|}(x) = \frac{(-1)^{|m|}}{2^l l!} (1-x^2)^{\frac{|m|}{2}} \left( \frac{d}{dx} \right)^{l+|m|} (x^2-1)^l, \quad (3.1.36)$$



with the recurrence relation

$$P_l^{|m|}(x) = \frac{1}{l - |m|} \left( x(2l - 1)P_{l-1}^{|m|}(x) - (l + |m| - 1)P_{l-2}^{|m|}(x) \right). \quad (3.1.37)$$

Substituting the angle dependent eigenvector back into the Hamiltonian in Eq. (3.1.29)

$ m $	$l$	$P_l^{ m }(x)$
0	0	1
0	1	$x$
0	2	$\frac{1}{2}(3x^2 - 1)$
1	1	$-\sqrt{1 - x^2}$
1	2	$-3x\sqrt{1 - x^2}$
2	2	$3(1 - x^2)$

**Table 3.2:** Lowest order associated Legendre polynomials.

and using the Schrödinger equation yields

$$-\frac{\hbar^2}{2m^*} \left\{ \frac{\partial^2}{\partial r^2} + \frac{2}{r} \frac{\partial}{\partial r} - \frac{l(l+1)}{r^2} - \frac{emB}{\hbar c} \right\} \psi(r) + \frac{1}{2} m^* \omega^2 r^2 \psi(r) = E \psi(r). \quad (3.1.38)$$

Comparing this equation with Eq. (3.1.16) we notice several similarities. The eigenvectors of Eq. (3.1.38) are given as

$$\psi_{nl}(r) = \sqrt{\frac{2n!}{(n+l+1/2)!}} \beta^{(l+3/2)/2} r^l e^{-\beta r^2/2} L_n^{l+1/2}(\beta r^2), \quad (3.1.39)$$

with the corresponding eigenvalues

$$E = \left( 2n + l + \frac{3}{2} \right) \hbar \omega + m \hbar \omega_B. \quad (3.1.40)$$

If we divide both sides by  $\hbar \omega_0$  we get

$$\frac{E}{\hbar \omega_0} = \left( 2n + l + \frac{3}{2} \right) \sqrt{1 + \frac{\omega_B^2}{\omega_0^2}} + m \frac{\omega_B}{\omega_0}. \quad (3.1.41)$$

Due to the constraint  $|m| \leq l$ , each  $l$  gives rise to a degeneracy of  $2l + 1$ . As in the two dimensional case we define  $N = 2n + l$  and plot the Fock-Darwin spectra for three dimensions in Fig.3.1.2. The same behavior as in Sec. 3.1.1 can be observed, but with added degeneracy. The filled shells can be located in the Fock-Darwin spectrum just as in Sec. 3.1.1. The filled shells and the degeneracy factors are tabulated for the lowest states in Tab. 3.3. The total degeneracy  $D$  is obtained by adding the spin degeneracy of the electrons.

If we now were to consider the electron spin we might ask ourselves if we could have combinations of orbital and spin momentum. This is indeed the case and the total angular momentum operator will obey the same commutator relations as the orbital

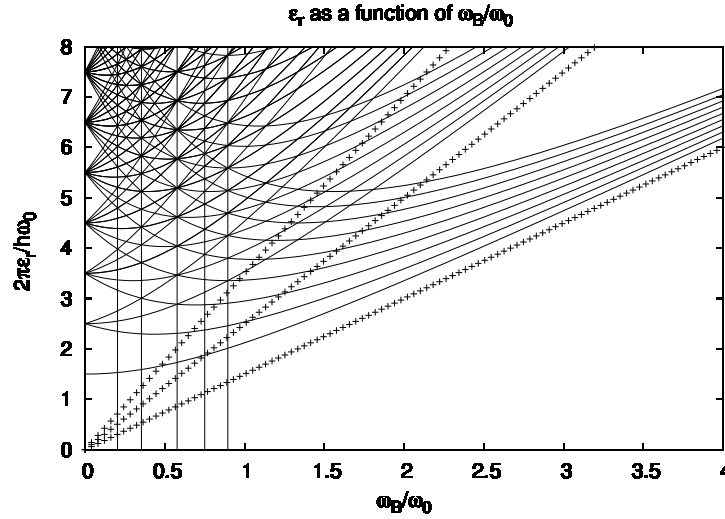


**Figure 3.1.2:** Three dimensional Fock-Darwin energy spectrum. Landau levels are clearly visible at the far right in the figure

N	D=2d	Shell filling=S
0	2	2
1	6	8
2	12	20
3	20	40

**Table 3.3:** Three dimensional quantum numbers and shell filling for a quantum dot without electron-electron interaction. The shell filling factor tells us how many electrons there is in the dot, up to the given state  $N$

momenta operators. The eigenvectors of the Hamiltonian will thus also be eigenvectors of the total angular momentum operator. As a consequence we want to exchange the orbital momenta  $\vec{l}$  by  $\vec{j}$ . The total angular momenta  $\vec{j}$  is defined as

$$\vec{j} = \vec{l} + \vec{s}, \quad (3.1.42)$$

where  $\vec{s}$  is the electron spin. The same restrictions applies to  $m$ , that is  $|m| \leq j$ . Note however that  $m$  now take half integer values. This also is the case for  $j$ , as  $j = 0, 1/2, 1, 3/2, 2, \dots$ . See basic textbooks in quantum mechanics, for example [Shankar; 1994]. The two last sections shed light on some of the effects seen in single-electron quantum dots. It is by far a complete model and in the next section we will include the electron-electron interaction to investigate the two-electron quantum dot.

## 3.2 Two electron quantum dot

Let us now consider a more realistic quantum dot confining two electrons. Since the mass is equal for electrons, we only include the constant correction due to the reduced

mass and keep  $m^*$  as the single electron mass during all calculation. The Hamiltonian for a two-electron system, interacting via the Coulomb potential has the following structure.

$$H = \sum_{i=1}^2 \left\{ \frac{1}{2m^*} \left( \vec{p}_i + \frac{e}{c} \vec{A}_i \right)^2 + \frac{1}{2} m \omega_0^2 r_i^2 + e\phi + \vec{p}_i \cdot \vec{B} \right\} + \frac{e^2}{4\pi\epsilon\epsilon_0 |\vec{r}_1 - \vec{r}_2|}. \quad (3.2.1)$$

Again the  $e\phi$  and  $\vec{p}_i \cdot \vec{B}$  becomes scalars when the expectation values are calculated. As a consequence we disregard them during calculations. They can be added to the eigenvalue at the end if desired. We still want to consider a constant magnetic field along the third axis. Just as before, we choose

$$\vec{A} = \frac{B}{2} (-y, x, 0). \quad (3.2.2)$$

The major problem of equation Eq. (3.2.1) is the interacting term. We introduce center-of-mass and relative coordinates to render the Hamiltonian separable. Defining

$$\vec{r} = \vec{r}_1 - \vec{r}_2, \quad (3.2.3)$$

$$\vec{R} = \frac{1}{2} (\vec{r}_1 + \vec{r}_2), \quad (3.2.4)$$

where  $\vec{R}$  and  $\vec{r}$  represent the center-of-mass and relative coordinates respectively, and

$$\vec{p} = \frac{1}{2} (\vec{p}_1 - \vec{p}_2), \quad (3.2.5)$$

$$\vec{P} = \vec{p}_1 + \vec{p}_2, \quad (3.2.6)$$

where  $\vec{P}$  and  $\vec{p}$  are the momenta in center-of-mass and relative coordinates, respectively. Let us define  $\vec{L}$ ,  $\vec{l}$ ,  $\vec{l}_1$  and  $\vec{l}_2$  as the orbital momentum for the center-of-mass, relative, particle one and particle two respectively. The orbital momenta for the center-of-mass motion is

$$\vec{L} = \vec{R} \times \vec{P}, \quad (3.2.7)$$

using Eq. (3.2.4) and (3.2.6) yields

$$\vec{L} = \frac{1}{2} \{ \vec{r}_1 \times \vec{p}_1 + \vec{r}_2 \times \vec{p}_1 + \vec{r}_1 \times \vec{p}_2 + \vec{r}_2 \times \vec{p}_2 \}. \quad (3.2.8)$$

Similarly we get

$$\vec{l} = \frac{1}{2} \{ \vec{r}_1 \times \vec{p}_1 - \vec{r}_2 \times \vec{p}_1 - \vec{r}_1 \times \vec{p}_2 + \vec{r}_2 \times \vec{p}_2 \}, \quad (3.2.9)$$

$$\vec{l}_1 = \vec{r}_1 \times \vec{p}_1, \quad (3.2.10)$$

$$\vec{l}_2 = \vec{r}_2 \times \vec{p}_2. \quad (3.2.11)$$

Adding the relative and center-of-mass angular momenta gives the relation

$$\vec{l}_1 + \vec{l}_2 = \vec{l} + \vec{L}. \quad (3.2.12)$$

In other words, the total orbital momentum is conserved under the coordinate transformation.

Maxwell's equations [Goldstein et al.; 2002] implies that  $\vec{A}$  must be linear, resulting in

$$\vec{A}(\vec{r}) = \vec{A}(\vec{r}_1) - \vec{A}(\vec{r}_2), \quad (3.2.13)$$

$$\vec{A}(\vec{R}) = \frac{1}{2} \left( \vec{A}(\vec{r}_1) + \vec{A}(\vec{r}_2) \right). \quad (3.2.14)$$

We now want to transform Eq. (3.2.1) to the new coordinates. We see that

$$p_1^2 + p_2^2 = \frac{1}{2} (P^2 + 4p^2), \quad (3.2.15)$$

$$r_1^2 + r_2^2 = \frac{1}{2} (4R^2 + r^2), \quad (3.2.16)$$

$$|\vec{r}_1 - \vec{r}_2| = r. \quad (3.2.17)$$

The transformed Hamiltonian can now be separated as

$$H = 2H_r + \frac{1}{2}H_R, \quad (3.2.18)$$

with the definitions

$$H_r = \frac{p^2}{2m^*} + \frac{1}{2}m^*\omega_r^2 r^2 + \frac{e^2}{8\pi\epsilon_0\epsilon r}, \quad (3.2.19)$$

$$H_R = \frac{P^2}{2m^*} + \frac{1}{2}m^*\omega_R^2 R^2, \quad (3.2.20)$$

$$\omega_r = \frac{\omega_0}{2}, \quad (3.2.21)$$

$$\omega_R = 2\omega_0, \quad (3.2.22)$$

where  $H_r$  and  $H_R$  are the Hamiltonians for the relative and center-of-mass respectively. If we do the minimal substitution with new variables  $\vec{A}_r$  and  $\vec{A}_R$  for the vector fields we get the Hamiltonian

$$H = \frac{(\vec{P} + \vec{A}_R)^2}{4m^*} + m^*\omega_0^2 R^2 + \frac{(\vec{p} + \vec{A}_r)^2}{m^*} + \frac{1}{4}m^*\omega_0^2 r^2 + \frac{e^2}{4\pi\epsilon_0\epsilon} \frac{1}{r}. \quad (3.2.23)$$

If we write out this equation and compare it to equation Eq. (3.2.1) we see that it is convenient to define the new potentials as

$$\vec{A}_r = \frac{1}{2}\vec{A}(\vec{r}), \quad (3.2.24)$$

$$\vec{A}_R = 2\vec{A}(\vec{R}). \quad (3.2.25)$$

With these definitions we can rewrite Eq. (3.2.23) as

$$H = 2H_r + \frac{1}{2}H_R + H_S, \quad (3.2.26)$$

$$H_R = \frac{(\vec{P} + \vec{A}_R)^2}{2m^*} + \frac{1}{2}m^*\omega_R^2 R^2, \quad (3.2.27)$$

$$H_r = \frac{(\vec{p} + \vec{A}_r)^2}{2m^*} + \frac{1}{2}m^*\omega_r^2 r^2 + \frac{e^2}{8\pi\epsilon_0\epsilon r}, \quad (3.2.28)$$

$$H_S = \vec{\rho}_1 \cdot \vec{B} + \vec{\rho}_2 \cdot \vec{B}. \quad (3.2.29)$$

In Eq. (3.2.26) we have included an extra term called  $H_S$ . This is the operator for the spin coupling to the magnetic field. Previously we dropped this terms from the Hamiltonian, but we have included it here to show that there is no need to transform it. Using the Schrödinger equation

$$H\Psi = E\Psi, \quad (3.2.30)$$

with the Hamiltonian defined in Eq. (3.2.26) we can write the eigenvectors as

$$\Psi = \Phi(r)\Upsilon(R)\chi(s_1, s_2), \quad (3.2.31)$$

where  $\Psi(r)$ ,  $\Upsilon(R)$  and  $\chi(s_1, s_2)$  are the eigenfunctions for the relative, center-of-mass and spin part, respectively. This can be done since  $H_r$ ,  $H_R$  and  $H_S$  commute. The corresponding eigenvalues are

$$E = 2E_r + \frac{1}{2}E_R + \epsilon_{adj}, \quad (3.2.32)$$

where  $\epsilon_{adj}$  includes the eigenvalue of  $H_S$ . The eigensolutions of the center-of-mass Hamiltonian are analogues to the one particle case, but with modified parameters. They are worked out in Sec. 3.1.1 and 3.1.2 for two and three dimensions, respectively. We will now only focus on the relative part until we bring everything together at the end, adding the center-of-mass contributions. It turns out that there exist solutions for the relative part which are exact, but only for special values of  $\omega$ . The solutions are worked out in App. A.8. In the general case we need to solve the differential equations numerically. This is what we cover in the next section. However, the analytic approach in App. A.8 can be used to check the stability of the numerical methods.

## Chapter 4

# Interacting electrons and diagonalization

This chapter deals with the solutions of the center-of-mass and relative part of the two-electron quantum dot Hamiltonian. In addition to Chapter 2, this chapter is important for the future work of this thesis. We here develop numerical methods for solving the relative part and do an analysis where several methods are available. This hopefully ensures the best choice of methods. In this chapter we will switch to the Dirac notation due to its simplicity. See any textbook on quantum mechanics, for example [Shankar; 1994] for a mathematical introduction to the Dirac notation. Up until now, we have had the possibility to solve the Schrödinger equations analytically. This is not the case for the relative part. The two and three dimensional solutions of Eq. (3.2.30) can be solved generally by exact diagonalization. By exact we now mean as exact as the numerical limitations allow. These limitations lies in the accuracy, size and computing time. Using Dirac notation we can now write Eq. (3.2.30) as

$$H|\Psi\rangle = E|\Psi\rangle, \quad (4.0.1)$$

where  $|\Psi\rangle$  can be expanded in the basis vectors  $|\beta\rangle$  as

$$|\Psi\rangle = \sum_{\beta} \langle\beta|\Psi\rangle |\beta\rangle, \quad (4.0.2)$$

with  $H$  from Eq. (3.2.26). The quantum numbers  $\beta$  describing the different states are at this point unknown. The eigenvectors  $|\beta\rangle$  form a basis in the Hilbert space, see for example [Shankar; 1994] for details. They are orthonormal, hence

$$\langle\beta'|\beta\rangle = \delta_{\beta'\beta}. \quad (4.0.3)$$

Inserting Eq. (4.0.2) into Eq. (4.0.1) gives

$$\sum_{\beta} H|\beta\rangle \langle\beta|\Psi\rangle = \sum_{\beta} E|\beta\rangle \langle\beta|\Psi\rangle, \quad (4.0.4)$$

and multiplying from the left with  $\langle\beta'|\Psi\rangle$  yields

$$\sum_{\beta} \langle\beta'|H|\beta\rangle \langle\beta|\Psi\rangle = \sum_{\beta} E \delta_{\beta'\beta} \langle\beta|\Psi\rangle. \quad (4.0.5)$$

Defining the coefficient  $\Psi_{\beta} = \langle\beta|\Psi\rangle$  gives

$$\sum_{\beta} \langle\beta'|H|\beta\rangle \Psi_{\beta} = E \Psi_{\beta'}, \quad (4.0.6)$$

which can be written as

$$\tilde{H}\vec{\Psi} = E\vec{\Psi}, \quad (4.0.7)$$

where  $\tilde{H} = \langle\beta'|H|\beta\rangle$ . To find the eigenvalues, we need to diagonalize the matrix  $\tilde{H}$ . This is done by the use of orthogonal transformations. The diagonalization routines in this thesis are the QR algorithm with implicit shifts and Householder reduction. They are among the most effective methods for solving eigenproblems. The derivation of these methods are outlined in [Golub and Loan; 1996] and [Press et al.; 2002]. More optimized diagonalization methods can be employed when only the extreme eigenvalues are needed, but their are not covered in this chapter. In the next section we will diagonalize the Hamiltonian from Eq. (3.2.26) by using eigenvectors of the harmonic oscillator as a basis. The analytical solutions worked out in App. A.8 will be used to check the choice of basis at the end of this chapter. Perturbation theory is also considered and a comparison is done between perturbation theory and the exact diagonalization method. This will give a convenient overview of the different solutions.

## 4.1 Diagonalization in the harmonic oscillator basis

In App. A.7.1 we calculated the exact harmonic oscillator basis functions for two dimensions. The eigensolutions of the interacting and non-interacting Hamiltonians generally differ. In this thesis we will approximate the interacting basis by using a harmonic oscillator basis. This is convenient since we have analytic expressions for the eigenvectors. The motivation for doing this will follow as soon as we have developed the notation and calculation methods for two dimensions. The diagonalization of the Coulomb interaction needs a discussion regardless of the basis used. The analogy between two and three dimensions should now be clear from Secs. 3.1.1 and 3.1.2.

### 4.1.1 Relative terms in two dimensions

The two dimensional Schrödinger equation in the harmonic oscillator basis can be written

$$H_0|NMnm\rangle = E_0|NMnm\rangle, \quad (4.1.1)$$

where  $H_0$  are the Hamiltonian from Eq. (3.2.26), but without the interaction. The quantum numbers  $N$  and  $M$  represent the center-of-mass basis, while  $n$  and  $m$  represent the relative basis. In this thesis, we use the harmonic oscillator bases for both the center-of-mass and the relative eigenvectors. From Eq. (4.0.7) we see that the matrix

of interest can be written as

$$\tilde{H} = \langle N'M'n'm'|H|NMnm\rangle. \quad (4.1.2)$$

In the rest of this section we disregard the spin coupling  $H_S$  and the addition energy  $\epsilon_{adj}$  from Eq. (3.2.26) until further notice. From Eq. (3.2.26) we can now write

$$\tilde{H} = 2\langle N'M'n'm'|H_r|NMnm\rangle + \frac{1}{2}\langle N'M'n'm'|H_R|NMnm\rangle. \quad (4.1.3)$$

The relative Hamiltonian  $H_r$  is diagonal in  $N, N', M$  and  $M'$ . The center-of-mass Hamiltonian  $H_R$  is diagonal in  $n, n', m$  and  $m'$ . Then matrix from Eq. (4.1.3) yields

$$\tilde{H} = 2\langle n'm'|H_r|nm\rangle + \frac{1}{2}\langle N'M'|H_R|NM\rangle. \quad (4.1.4)$$

The last term is the center-of-mass energy. The center-of-mass solutions are exactly the same as the solutions worked out in App. A.7.1, but with capital quantum numbers and a slightly different  $\omega$  defined as

$$\omega^2 = \omega_R^2 + \omega_{B_R}^2, \quad (4.1.5)$$

where

$$\omega_{B_R} = 2\omega_B. \quad (4.1.6)$$

The definition of  $\omega_R$  and  $\omega_B$  can be found in Secs. 3.2 and 3.1.1 respectively. We can simplify Eq. (4.1.4) even more. The relative motion is the same as the center-of-mass motion, but with the addition of the Coulomb interaction and a different  $\omega$  factor given as

$$\omega^2 = \omega_r^2 + \omega_{B_r}^2, \quad (4.1.7)$$

where

$$\omega_{B_r} = \frac{\omega_B}{2}. \quad (4.1.8)$$

The definition of  $\omega_r$  can be found in Sec. 3.2. We can then define  $H_r = H_{r_0} + H_{r_1}$  where  $H_{r_1}$  describes the Coulomb interaction part of  $H_r$  while  $H_{r_0}$  is equal to  $H_R$  with the coordinates replaced by  $r$ , with  $\omega$  defined in Eq. (4.1.7). The Hamiltonian  $H_{r_1}$  will be diagonal in  $m$  and  $m'$  as the angle dependent part of the eigenvector is a mere constant. We can now write the relative matrix from Eq. (4.1.4) as

$$\tilde{H}_r = (2n + |m| + 1)\hbar\omega + m\hbar\omega_B + 2\langle n'm|H_{r_1}|nm\rangle, \quad (4.1.9)$$

where  $\omega$  is defined as

$$\omega^2 = \omega_0^2 + \omega_B^2. \quad (4.1.10)$$

The only terms we need to calculate when using the Harmonic oscillator basis is the matrix elements

$$\langle n'm|H_{r_1}|nm\rangle = \int_V \Psi_{n'm}^* \Psi_{nm} \frac{\sigma}{r} dV. \quad (4.1.11)$$

The constant  $\sigma = e^2/8\pi\epsilon\epsilon_0$  determines the strength of the interaction, while  $\Psi$  describe the eigenfunctions defined in Eq. (3.1.20). The volume element in two dimensions can be found in App. A.3. Substituting the volume element  $dV = r dr d\theta$  and the



eigenfunctions into Eq. (4.1.11), we see that

$$\langle n'm|H_{r_1}|nm\rangle^{2D} = \frac{1}{2\pi} \int_0^{2\pi} \int_0^\infty \psi_{nm}(r) \psi_{n'm}(r) \frac{\sigma}{r} r dr d\theta. \quad (4.1.12)$$

We are left with an integral over the radial eigenfunctions defined in Sec. 3.1.1. The integral we need to calculate in two dimensions now has the form

$$\langle n'm|H_{r_1}|nm\rangle^{2D} = \sigma \int_0^\infty \psi_{nm}(r) \psi_{n'm}(r) dr. \quad (4.1.13)$$

To obtain eigenvalues we need to diagonalize this matrix. This is done on a computer using matrix manipulation techniques. In principle  $n \rightarrow \infty$ , resulting in infinitely large matrices. Obviously, infinite matrices cannot be treated and we need to introduce a cut-off on the quantum numbers. It is very important that this cut-off does not affect the eigenvalues we are to consider. In this thesis, we only consider the lowest eigenvalues, but we still need to determine a sufficiently high cut-off.

We need to calculate integral in Eq. (4.1.11) in an efficient way, numerically. Let us first develop an explicit expression for this integral in two dimensions. Substituting the basis function from Eq. (3.1.17) into Eq. (4.1.13) yields

$$\langle n'm|H_{r_1}|nm\rangle^{2D} = \sigma \int_0^\infty \beta^{|m|+1} r^{2|m|} e^{-\beta r^2} L_{n'}^{|m|}(\beta r^2) L_n^{|m|}(\beta r^2) dr, \quad (4.1.14)$$

where  $\beta = m^* \omega / \hbar$ . The Laguerre polynomials  $L_n^{|m|}(\beta r^2)$  are defined in App. A.7.1. Substituting  $x = \beta r^2$  gives

$$\langle n'm|H_{r_1}|nm\rangle^{2D} = \frac{\sigma \sqrt{\beta}}{2} \int_0^\infty x^{|m|-1/2} e^{-x} L_{n'}^{|m|}(x) L_n^{|m|}(x) dx. \quad (4.1.15)$$

The constant term in front of the integral can be simplified by multiplying the fraction by  $\omega m^* \hbar^3$  in the denominator and nominator. This give rise to a modified Bohr radius  $a_0^*$  due to the effective mass of the electron and the modified oscillator length  $l_B$ . Both of these are defined in Eqs. (A.8.11) and (A.8.12) respectively. Dividing the equation by  $\hbar \omega$  yields

$$\frac{\langle n'm|H_{r_1}|nm\rangle^{2D}}{\hbar \omega} = \frac{l_B}{4a_0^*} I_{n'n}^{2D}, \quad (4.1.16)$$

where

$$I_{n'n}^{2D} = \sqrt{\frac{2n!}{(n'+|m|)!}} \sqrt{\frac{2n!}{(n+|m|)!}} \int_0^\infty x^{|m|-1/2} e^{-x} L_{n'}^{|m|}(x) L_n^{|m|}(x) dx. \quad (4.1.17)$$

This is a dimensionless integral and this suits a dimensionless form of the energy term in Eq. (4.1.9) perfectly. The interacting integrals cannot generally be solved analytically due to the Laguerre polynomials, but it is possible to express Eq. (4.1.11) as a series. We will now consider the two dimensional matrix elements in Eq. (4.1.13) and express the eigenfunction by a series over the Talmi integrals [Talmi; 1952]. By doing this we can develop an analytic solution to Eq. (4.1.13) of any order in the quantum numbers without calculating the integral. We will follow [Moshinsky; 1969] where the solutions

for the three dimensional harmonic oscillator are worked out in detail. By using the alternative eigenfunction from Eq. (A.7.37) and the substitution  $\rho^2 = \beta r^2$  we can now write Eq. (4.1.13) as

$$\langle n'm | H_{r_1} | nm \rangle^{2D} = \hbar\omega \sum_{k'=0}^{n'} \sum_{k=0}^n a_{n'mk'} a_{nmk} \frac{l_B}{4a_0^*} \int_0^\infty e^{-\rho^2} \rho^{2(k'+k+|m|)} d\rho, \quad (4.1.18)$$

where  $a_{nmk}$  is defined as

$$a_{nmk} = (-1)^k \frac{\sqrt{2n! (n+|m|)!}}{(n-k)! (|m|+k)! k!}. \quad (4.1.19)$$

If we now redefine  $p = k + k' + |m|$  we can write the equation above in the following way

$$\langle n'm | H_{r_1} | nm \rangle^{2D} = \hbar\omega \frac{l_B}{4a_0^*} \sum_p B(n'm, nm, p) I_p. \quad (4.1.20)$$

We now have a series expansion of the  $B$  factors given as

$$B(n'm, nm, p) = \frac{\Gamma(p+3/2)}{2} \sum_{k=0}^n a_{nmk} a_{n'm(p-k-|m|)}, \quad (4.1.21)$$

where  $\Gamma$  is the Gamma function [Abramowitz and Stegun; 1972] and  $I_p$  the Talmi integrals, defined as

$$I_p = \frac{2}{\Gamma(p+3/2)} \int_0^\infty \rho^{2p} e^{-\rho^2} d\rho. \quad (4.1.22)$$

The Talmi integrals are tabulated in [Abramowitz and Stegun; 1972] and can be written as

$$I_p = \frac{\Gamma(p+1/2)}{\Gamma(p+3/2)}. \quad (4.1.23)$$

The properties of Gamma function ensure that  $\Gamma(n+1) = n\Gamma(n)$ , see [Abramowitz and Stegun; 1972] for details. Using this,  $I_p$  can be simplified to

$$I_p = \frac{1}{p+1/2}. \quad (4.1.24)$$

The coefficient  $B$  is tabulated and discussed in [Brody et al.; 1960, Brody and Moshinsky; 1967] and can be found by the rather complicated expression listed in App. A.9.1. The summation over  $p$  is by the relation  $p = k + k' + |m|$  only allowed to take the following values

$$|m| \leq p \leq n' + n + |m|. \quad (4.1.25)$$

The matrix elements in two dimensions can then be written as

$$\frac{\langle n'm | H_{r_1} | nm \rangle^{2D}}{\hbar\omega} = \frac{l_B}{4a_0^*} \sum_p B(n'm, nm, p) \frac{1}{p+1/2}. \quad (4.1.26)$$

### 4.1.2 Relative term in three dimensions

For three dimensions all the previous discussions apply. But there are important differences. First of all, the volume element is different. In three dimensions we would need to replace  $dV = r dr d\theta$  by  $dV = r^2 \sin\phi dr d\theta d\phi$ . See App. A.3 for details. The quantum number  $m$  is replaced by  $l + 1/2$  in addition to slight differences in the eigenfunctions, compare Secs. 3.1.1 and 3.1.2. Just as for two dimensions, the angle dependent eigenvector does not give contributions. Taking this into account we get the interacting energy in three dimensions as

$$\frac{\langle n'l | H_{r1} | nl \rangle^{3D}}{\hbar\omega} = \frac{l_B}{4a_0^*} I_{n'n}^{3D}, \quad (4.1.27)$$

with  $I_{3D}$  defined as

$$I_{n'n}^{3D} = \sqrt{\frac{2n'!}{(n' + l + 1/2)!}} \sqrt{\frac{2n!}{(n + l + 1/2)!}} \int_0^\infty x^l e^{-x} L_{n'}^{l+1/2}(x) L_n^{l+1/2}(x) dx. \quad (4.1.28)$$

The three dimensional counterpart for the series expansion should be obvious, as the only difference comes in the power of  $p$  in Eq. (4.1.22). We will now move on to the process of calculating Eq. (4.1.9), where we will compare numerical integrations schemes with the series expansions method.

### 4.1.3 Discussions regarding matrix cut-off and matrix element calculation scheme

Both the integral and series method involves factorials. They increase as the quantum numbers grows. As a consequence, we need to investigate how factorials can be represented in an effective and accurate way. In modern computers double precision is the most common representation when large numbers or precision are needed. Double precision utilize 64 bits to represent a single number. For an overview on number representation, see [Landau and Páez; 1997]. There exist arbitrary precision methods, but they greatly increase computation time. Hence they are not used in this thesis. The largest numbers we can represent using double precision are in the range of  $10^{308}$ . This limit is reached for  $170!$  By looking at the normalization factors in Eqs. (4.1.17) and (4.1.28) we see that the largest factorials are given as  $(n + |m|)!$  for two dimensions and  $(n + l + 1/2)!$  for three dimensions. Note that we can write

$$(n + \frac{1}{2})! = \frac{\sqrt{\pi}}{2^{2n+1}} \frac{(2n+1)!}{n!}. \quad (4.1.29)$$

This yields an upper numerical limit of  $n + |m| = 170$  and  $n + l = 84$  in two and three dimension respectively for the integration method. For the series method we see from Eq. (A.7.38) and (A.7.57) that the upper limits due to the single factorial calculations are the same as for the integration method. But we are multiplying large factorials together in a brute force way, thus making it more severe. In addition we are summing large and small numbers, which could affect accuracy.

We will now show why we prefer the integration scheme. In Fig. 4.1.1 we have made a comparison between the two methods plotting the normalization  $\langle nm|nm\rangle$  and  $\langle nl|nl\rangle$  for two and three dimensions respectively as a function of  $n$ . The numerical integration was carried out using Gauss-Laguerre quadrature, see App. A.6 for an analysis of different integration techniques. We clearly see the problems with the series method. In both two and three dimensions the normalization diverges as soon as we hit  $n \approx 14$  for  $m, l = 0$  and around  $n \approx 12$  for  $m, l = 5$ . This seems a bit odd at first, but let us first address the brute force multiplication of factorials. Observe that we

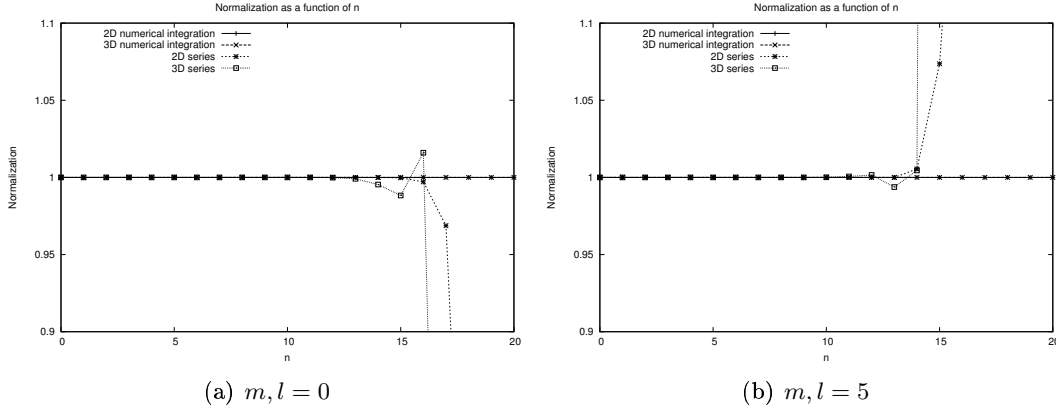


**Figure 4.1.1:** Comparing normalization  $\langle nm|nm\rangle$  and  $\langle nl|nl\rangle$  between numerical integration and series expansion as function of  $n$ . We have calculated the factorials in a brute force way. The series method seems useless above  $n \approx 15$ , while the integration method is completely stable.

can write

$$\frac{a! b!}{c!} = e^{\ln(a!) + \ln(b!) - \ln(c!)} \quad (4.1.30)$$

This is a simple, yet clever way of expressing ratios of large factorials. In Fig. 4.1.2 we make use of this multiplication scheme. However, notice that there is not any noticeable difference between Fig. 4.1.1 and 4.1.2. By employing a totally different

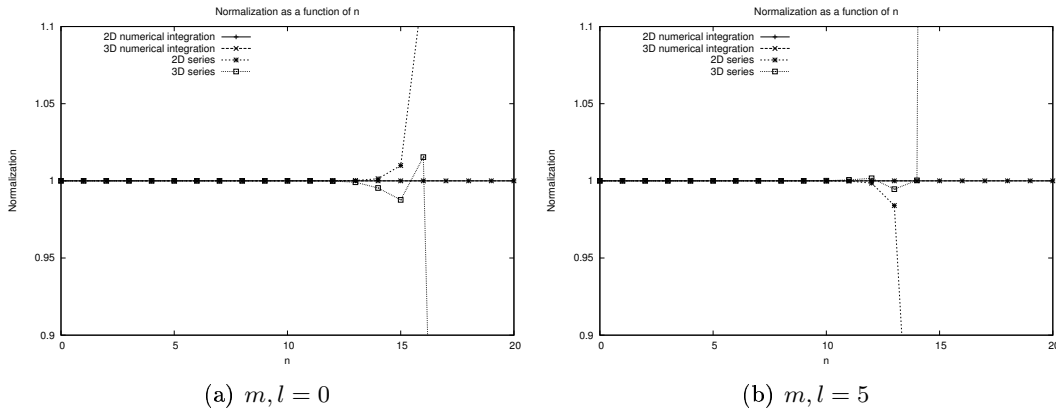


**Figure 4.1.2:** From Fig. 4.1.1, but here we use the multiplication scheme in Eq. (4.1.30) to evaluate the factorials. We see the same behavior as in Fig. fig:normalization.

multiplication scheme for the factorials, we are left with the same behavior. If we take a look at the factorial products they are well within the numerical limit at  $10^{308}$  even for quite large  $n$ , if  $m, l = 0$ . This predicts that the change of multiplication scheme should not have any impact, as long as we are within the numerical limits. The only operation not considered is the summation in Eq. (4.1.18) and its three dimensional counterpart. For each increase in  $k$  or  $k'$  we change sign of the coefficient, thus leading to an alternating series. At the same time,  $k$  and  $k'$  are increasing, so we are summing larger and larger positive and negative numbers. To illustrate that this is the problem, we sum all the positive and negative numbers separately and take the sum of the totals at the end. By using the brute force multiplication scheme, Fig. 4.1.3 illustrates a slight improvement, at least for two dimensions. The series method needs sophisticated and maybe arbitrary precision techniques to give acceptable results at high  $n$ . Hence we will use numerical integration in this thesis. Even though we do not use the series method, it is an excellent tool for checking numerical calculations for low  $n$  values.

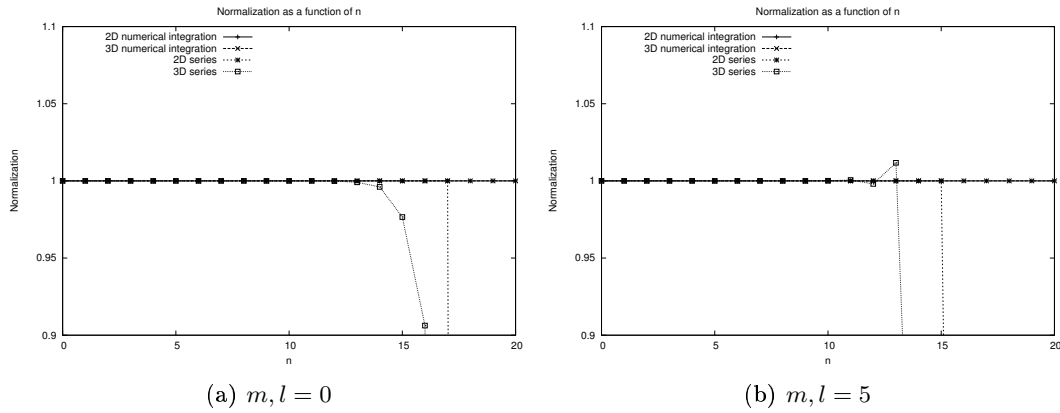


**Figure 4.1.3:** Comparing normalization  $\langle nm|nm\rangle$  and  $\langle nl|nl\rangle$  between numerical integration and series expansion as function of  $n$ . We again use brute force multiplication to calculate the factorials, but with separate negative and positive summation. We see slight improvements over Fig. fig:normalization.

We need to choose a fast and accurate numerical integration technique. In harmonic oscillator problems the Gauss-Laguerre technique is preferred, see App. A.6 for details. The number of different quantum numbers  $n'$  and  $n$  are restricted due to computer work. A method that decreases computer accuracy should not be preferred unless the loss can be controlled. Due to finite computing time, we need to have an upper limit on  $n'$  and  $n$ . Ideally we want to set it very large, but even modern computers are severely limited when it comes to matrix calculations. Let us now investigate the convergence of the eigenvalues and how they relate to the matrix cut-off. We introduce the difference  $\epsilon$ , which we define as

$$|\epsilon| = |E_n^{n_{max}} - E_n^{n'_{max}}|. \quad (4.1.31)$$

Where  $n_{max}$  is the matrix cutoff and  $n'_{max} = n_{max} - 1$ . With this definition we are diagonalizing  $n_{max} \times n_{max}$  matrices to obtain the eigenvalues of  $E_n^{n_{max}}$ . Then in the next iteration  $n_{max}$  is increased by one and the difference in Eq. (4.1.31) is found by taking the difference between the eigenvalues diagonalized at  $n_{max}$  and  $n'_{max}$ . As

we increase  $n_{max}$  more and more states are included in the diagonalization process. As the matrix grows larger, the added row and column contribute less to the lowest eigenvalues. Thus we should observe a convergence of the lowest eigenvalues in  $\epsilon$  as we increase  $n_{max}$ . The strength of the Coulomb interaction is determined by  $l_B/a_0^*$ . When the strength grows the off-diagonal elements grows and might give faster or slower convergence, depending on the numerical diagonalization method used. Most diagonalization methods converge faster if the matrix elements on the diagonal is larger by a significant margin than the off-diagonal elements. If the matrix elements becomes almost identical we might get severe problems with convergence. However, in our case, the diagonal elements will always be largest due to the non-interacting energies.

In Figs. 4.1.4 and 4.1.5 the difference  $|\epsilon|$  in three dimensions is plotted against  $n_{max}$ , for two choices of  $l$ . For  $l_B/a_0^* = 1$  at  $l = 0$ , we have a slow convergence compared

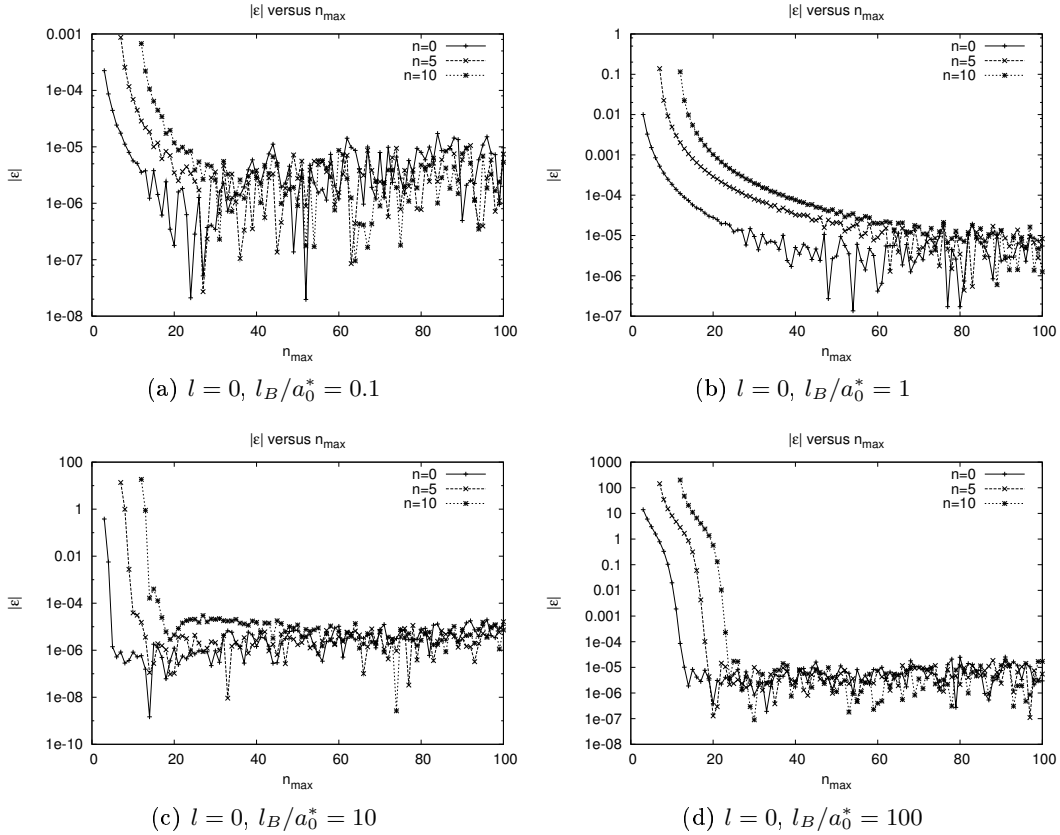


**Figure 4.1.4:** Relative error,  $|\epsilon|$  defined in Eq. (4.1.31), as a function of matrix cutoff  $n_{max}$  for three dimensions. The matrix cut-off  $n_{max}$  determines the size of the  $n_{max} \times n_{max}$  matrix diagonalized to obtain the eigenvalues  $E_n^{n_{max}}$ . In this figure  $l = 0$ . It is easy to observe convergence at  $n_{max} \approx 80$  for all cases. In some situations as for example  $l_B/a_0^* = 100$  we even have convergence at  $n_{max} \approx 30$ . Also observe a more rapid convergence for  $l_B/a_0^* = 10$  and  $l_B/a_0^* = 100$ .

to other choices of  $l_B/a_0^*$ , while  $l_B/a_0^* = 10$  seems to give the fastest convergence of the four, at least for  $l = 0$ . As  $n_{max}$  approaches 80, we see that we have convergence for all four values of  $l_B/a_0^*$ . Even at  $n_{max} = 30$ , most of the plots have well a defined convergence, with a fluctuation of about  $10^{-5}$ . In Fig. 4.1.5 the same applies. We can

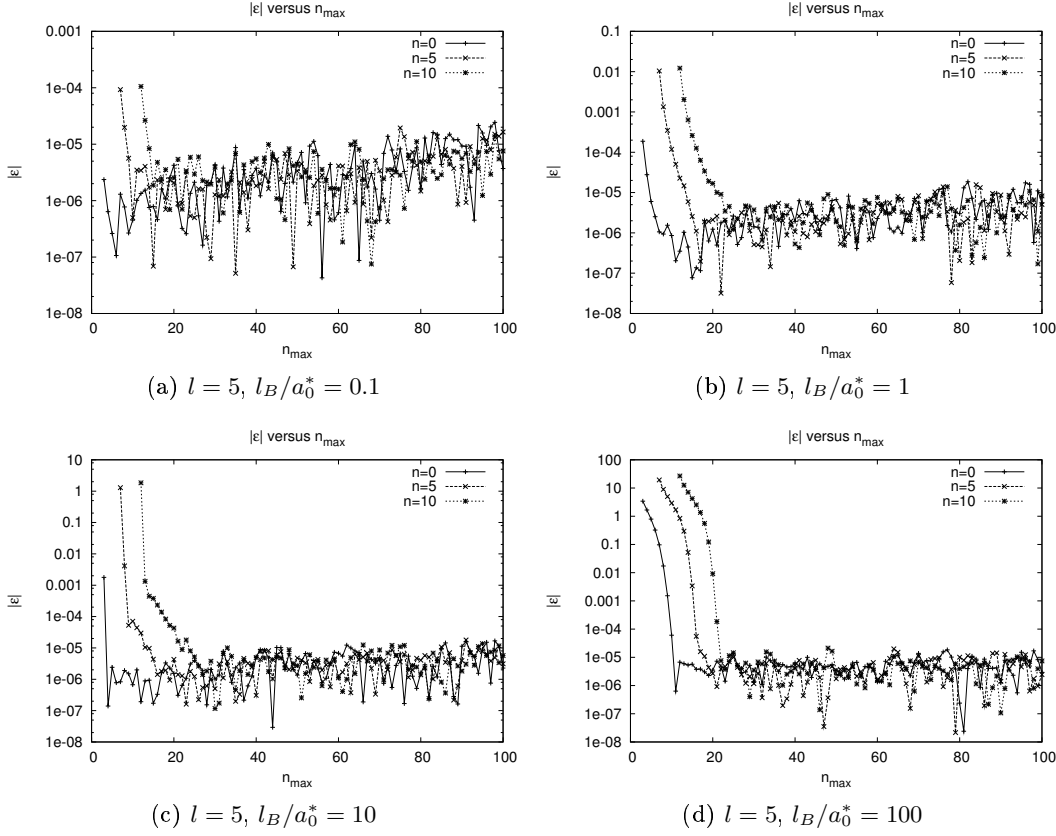


**Figure 4.1.5:** From Fig. 4.1.4, but now for  $l = 5$ . Here the convergence is generally faster than for  $l = 0$ . As soon as  $n_{max} \approx 30$ , a stable solution is obtained.

then conclude that a choice of  $n_{max} = 80$  is sufficient for the given values of  $l_B/a_0^*$  and  $l$ . For two dimensions one should expect to see the same results. Figs. 4.1.6 and 4.1.7 illustrate the two dimensional case. We clearly see the same behavior as in three dimensions. Note how much more slower the convergence is for  $l_B/a_0^* = 1$  at  $n = 5, 10$  and  $m = 0$ . For  $n_{max} = 80$  we have one magnitude difference in  $\epsilon$  when we compare it with the three dimensional counterpart. For two dimensions we conclude that  $n_{max} = 80$  is sufficient for all cases except  $l_B/a_0^* = 1$  at  $m = 0$ , where we should increase  $n_{max}$  to about 100 to obtain convergence for  $n = 5, 10$ . In Table 4.2 we summarize the discussion by listing the values of  $n_{max}$  used during simulations.

$m$	0				5			
$l_B/a_0^*$	0.1	1	10	100	0.1	1	10	100
$n$	$n_{max}$	$n_{max}$	$n_{max}$	$n_{max}$	$n_{max}$	$n_{max}$	$n_{max}$	$n_{max}$
0	80	80	80	80	80	80	80	80
5	80	100	80	80	80	80	80	80
10	80	100	80	80	80	80	80	80

**Table 4.1:** The matrix cut-off  $n_{max}$  used in simulations for two dimensions.

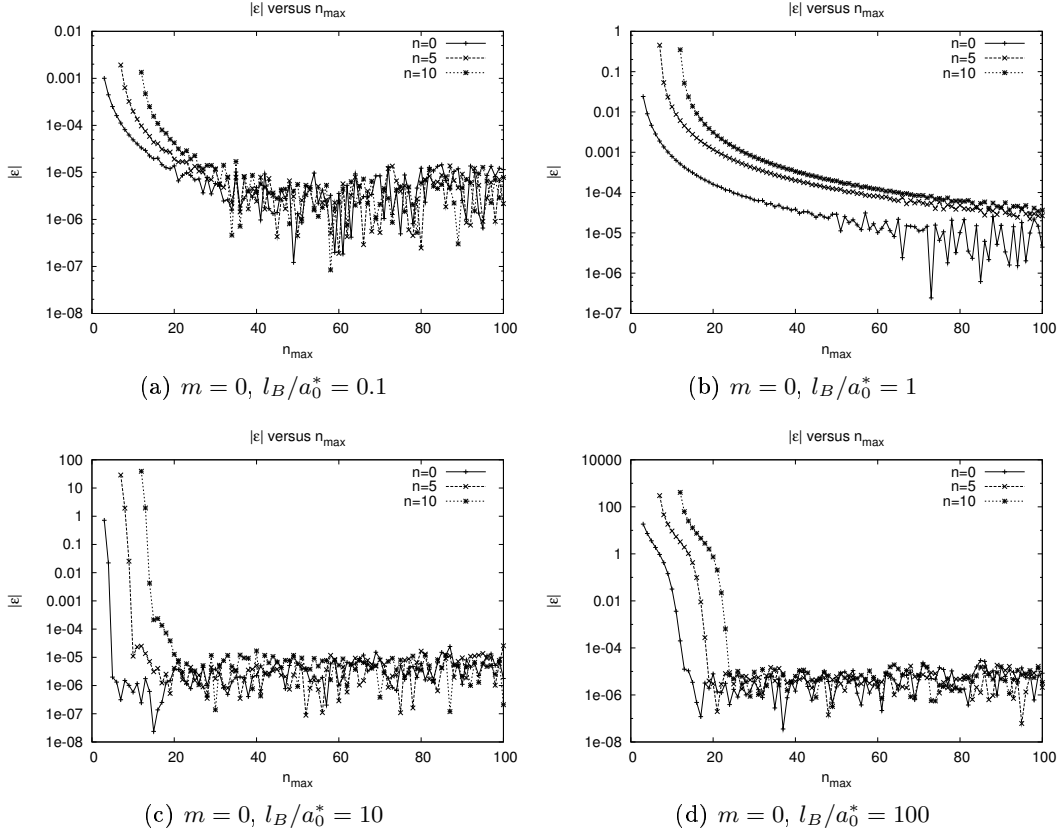


**Figure 4.1.6:** Relative error,  $|\epsilon|$  defined in Eq. (4.1.31), as a function of matrix cutoff  $n_{max}$  for two dimensions. The matrix cut-off  $n_{max}$  determines the size of the  $n_{max} \times n_{max}$  matrix diagonalized to obtain the eigenvalues  $E_n^{n_{max}}$ . In this figure  $m = 0$ . It is easy to observe convergence at  $n_{max} \approx 80$  for almost all cases. At  $l_B/a_0^* = 1$  we do not observe convergence for  $n = 5, 10$  before  $n_{max} \approx 100$ . An early convergence is also observed at for example  $l_B/a_0^* = 10$ . As in three dimension we have a more rapid convergence for  $l_B/a_0^* = 10$  and  $l_B/a_0^* = 100$ .

$m$	0				5			
$l_B/a_0^*$	0.1	1	10	100	0.1	1	10	100
$n$	$n_{max}$	$n_{max}$	$n_{max}$	$n_{max}$	$n_{max}$	$n_{max}$	$n_{max}$	$n_{max}$
0	80	80	80	80	80	80	80	80
5	80	80	80	80	80	80	80	80
10	80	80	80	80	80	80	80	80

**Table 4.2:** The matrix cut-off  $n_{max}$  used in simulation for three dimensions.

Now that the numerical methods are determined it is time to compare the diagonalization results with the analytic solutions obtained in App. A.8. We will in this section switch index between  $n$  and  $n'$  so there is no doubt about the principal quantum number  $n$ . The energy term is also relabeled and it should be obvious from App. A.8 how they are related. For two dimensions, we have the recursion relation



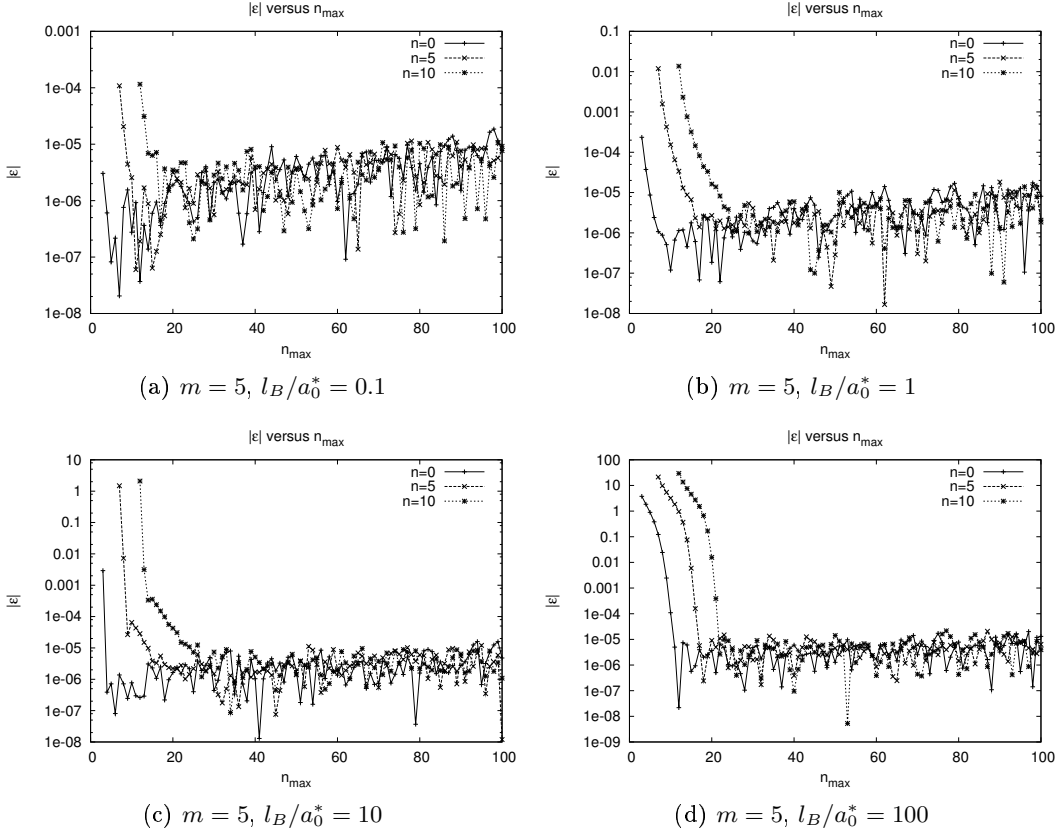


**Figure 4.1.7:** From Fig 4.1.6, but now for  $m = 5$ . The rather slow convergence for  $m = 0$  at  $l_B/a_0^* = 1$  have disappeared and we have convergence as soon as  $n_{max} \approx 30$  for all four plots.

from Eq. (A.8.27)

$$a'_n = \frac{1}{n'(n' + 2|m|)} \left[ (2(n' + |m| - 1) - \epsilon') a_{n'-2} + \frac{l_B}{a_0^*} a_{n'-1} \right] \quad (4.1.32)$$

for  $n \geq 2$ . Where

$$a_0 \neq 0, \quad (4.1.33)$$

$$a_1 = \frac{2l_B}{a_0^*(1 + 2|m|)}, \quad (4.1.34)$$

$$\epsilon' = 2(n + |m|). \quad (4.1.35)$$

The non-zero constant  $a_0$  can be taken outside and cancel in all calculations. For simplicity we define  $a_0 = 1$ . The relative energy in two dimensions from Eq. (A.8.34) is given as

$$\epsilon_r^{ex} = (n + |m|)\hbar\omega + m\hbar\omega_B, \quad (4.1.36)$$

which would relate to Eq. (4.1.9) in the general case. The energy term in Eq. (4.1.36) is only valid if  $a_{n'=n} = a_{n'=n+1} = 0$ . This puts restrictions on  $l_B/a_0^*$  for given  $m$  values. To find the exact energies we first solve Eq. (4.1.32) and terminate this at  $n' = n$  by

demanding that  $a_{n'=n} = 0$ . We then substitute the energy term from Eq. (4.1.35) and solve for  $l_B/a_0^*$ . The three dimensional counterparts can easily be found by replacing  $m = l + 1/2$ . Let us start with the simplest polynomial, which is when  $n = 2$ . Using  $a_2 = 0$  in Eq. (4.1.32) would give

$$\left(\frac{l_B^2}{a_0^{*2}}\right)_{n=2} = \frac{1 + 2|m|}{2}, \quad (4.1.37)$$

by the use of Eqs. (4.1.33) and (4.1.34). Finding  $n = 3$  involves a bit more algebra, but the same procedure applies and we get

$$\left(\frac{l_B^2}{a_0^{*2}}\right)_{n=3} = 3 + 4|m|. \quad (4.1.38)$$

Both  $n = 2$  and  $n = 3$  yield ground states for  $|m| = 0$ . For  $n \geq 3$  we get several solutions of  $l_B/a_0^*$ , two for  $n = 3$  for example. When this happens, the smallest value will be the ground state. To compare solutions with the diagonalization in the harmonic oscillator basis we will select a  $l_B/a_0^*$  value which suits the analytic solution. The  $m$  values will be equal in the diagonalization and the exact solutions. However, there is no guarantee that the principal quantum number in each case is the same. To avoid misunderstanding we will label  $n$  in the diagonalized solutions as  $n_d$  and  $n$  in the exact solutions as  $n_{ex}$ . Let us also define the relative error in energy between the exact solution and the diagonalized solution of the relative part as

$$|\epsilon_{ex-d}| = \left| \frac{\epsilon_{ex} - \epsilon_r}{\epsilon_{ex}} \right|, \quad (4.1.39)$$

where the energy  $\epsilon_r$  is obtained by diagonalizing Eq. (4.1.9). In Table 4.3 we compare the diagonalization solutions and the exact solutions for specific values of  $l_B/a_0^*$  which gives valid exact solutions. The difference between the solutions are not large, which can be seen from the error  $|\epsilon_{ex-d}|$ . They are within acceptable limits. The error is

$n_d$	$n_{ex}$	$l_B/a_0^*$	$m$	$\epsilon_r/\hbar\omega$	$\epsilon_{ex}/\hbar\omega$	$ \epsilon_{ex-d} $
0	2	$\sqrt{\frac{1}{2}}$	0	2.000610	2	$3.05 \times 10^{-4}$
0	2	$\sqrt{\frac{11}{2}}$	5	6.999998	7	$2.86 \times 10^{-7}$
0	3	$\sqrt{3}$	0	3.000438	3	$1.46 \times 10^{-4}$
0	3	$\sqrt{23}$	5	7.999999	8	$1.25 \times 10^{-7}$

**Table 4.3:** Comparison between the exact  $\epsilon_{ex}$  and the diagonalized  $\epsilon_r$  energies. The error  $|\epsilon_{ex-d}| = |(\epsilon_{ex} - \epsilon_r)/\epsilon_{ex}|$  is listed for different values of principal and orbital quantum numbers. The principal quantum number for the diagonalization is  $n_d$  while it is  $n_{ex}$  for the exact solutions. The orbital quantum numbers are the same for both solutions. The errors are acceptable, but are expected to increase as soon as we increase the principal quantum numbers.

expected to increase with excited states. For the lowest states, the harmonic oscillator basis is shown to be acceptable.

## 4.2 Perturbation as an alternative

Until now we have discussed what numerical schemes and approximations we should use in the diagonalization process, but we have left out any analytical approximation. As the interacting correction is small, at least for large  $r$  and small  $l_B/a_0^*$ , we could ask ourselves whether perturbation theory is a viable alternative to exact diagonalization. To second order we have

$$E_n = E_n^0 + \langle n^0 | H_{r_1} | n^0 \rangle + \sum_{n' \neq n} \frac{|\langle n' | H_{r_1} | n^0 \rangle|^2}{E_n^0 - E_{n'}^0}, \quad (4.2.1)$$

where  $|n^0\rangle$  is the normalized eigenvector for the unperturbed Hamiltonian  $H_{r_0}$  with eigenvalue  $E_n^0$ . See App. A.5 for the derivation of second order perturbation theory. A necessary condition for perturbative expansion is that the perturbation is small compared to the unperturbed eigenvalue  $E_n^0$ . In our case we would treat the Coulomb interaction as a perturbation and the single particle Hamiltonians as the unperturbed term. The Coulomb interaction falls off like  $1/r$  and as long as  $r$  is sufficiently big, this term is small. In our case the oscillator parameter  $l_B/a_0^*$  will also determine the strength of the interaction.

To calculate the integrals in the perturbation expansion we still use Gauss-Laguerre techniques. The series in Eq. (4.2.1) needs to be terminated at some  $n'_{max}$  and for comparison reasons we terminate this at  $n_{max} = 80$  as discussed in Sec. 4.1. By doing this, we ensure that we include the same number of corrections in both the perturbation expansion and the matrix diagonalization. We now define the relative error as

$$|\epsilon| = \left| \frac{\text{exact diagonalization} - \text{second order perturbation}}{\text{exact diagonalization}} \right|. \quad (4.2.2)$$

In Figs. 4.2.8 and 4.2.9 we have plotted the relative error  $|\epsilon|$  as a function of  $l_B/a_0^*$  for two and three dimensions, respectively. The condition in Eq. (A.5.19) is clearly illustrated for both two and three dimensions. For the lowest eigenvalues,  $n = 0$ , we need to go as low as  $l_B/a_0^* \approx 0.01$  to get a relative error of  $10^{-5}$  which still is quite high. Going to the higher states reduces the relative error. This has to do with the relative electron-electron distance. As the quantum numbers are increased, the electrons can be further apart and the interaction decreases. This is the case for both increasing  $n$  and  $m, l$ . In Fig. 4.2.10 we plot the difference  $||\epsilon_{2D}| - |\epsilon_{3D}||$  where  $|\epsilon_{2D}|$  and  $|\epsilon_{3D}|$  are the relative errors for two and three dimensions respectively. Two important facts can be deduced from this figure. The first fact is already discussed, where larger values of  $n$  and  $m, l$  gives less restrictions on the relative distance, thus decreasing the interaction. The other fact shows the important difference between two and three dimensions. Decreasing the dimensions from three to two gives further restriction on the electrons movement and there is a greater probability for them being closer to each other. This increases the interaction. Hence the relative error in three dimensions is less for a given  $l_B/a_0^*$ . Increasing the interaction strength  $l_B/a_0^*$  would worsen the difference, which is also observed in Fig. 4.2.10.

Remember that both the perturbation theory and the exact diagonalization are approximations to a solution we do not know exactly, except for special  $l_B/a_0^*$  values.

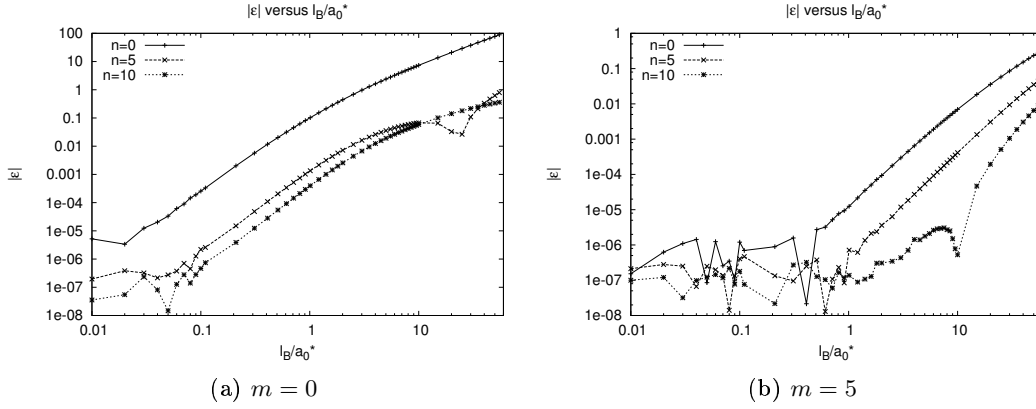


**Figure 4.2.8:** Relative error between matrix diagonalization and second order perturbation theory in two dimensions. Depending on the desired accuracy, we see from Fig. 4.2.8(a), that in order to use second order perturbation and keeping  $|\epsilon| < 0.001$ , we need to make sure that  $l_B/a_0^* < 0.1$  for  $n, m = 0$ . When we increase  $n$ , the electrons can be further apart. As a consequence we can increase  $l_B/a_0^*$  while still maintaining  $|\epsilon| < 0.001$ . The same discussion for Fig. 4.2.8(b), but with modified  $|\epsilon|$ . Note the sudden drop for  $n = 10$  in Figs. 4.2.8(a) and 4.2.8(b), the same thing happens with  $n = 5$  if we had extended  $l_B/a_0^*$  above 60. No explanation of this was found, but it is probably due to accidental increase in accuracy during summation of the perturbation series.

However, one thing is for sure, the perturbation theory is much more limited than matrix diagonalization techniques regarding the choice of  $l_B/a_0^*$ . Thus, we will not be using perturbation theory in this thesis. Its results will be compared with the matrix diagonalization for small values of  $l_B/a_0^*$ . Perturbation theory could be a

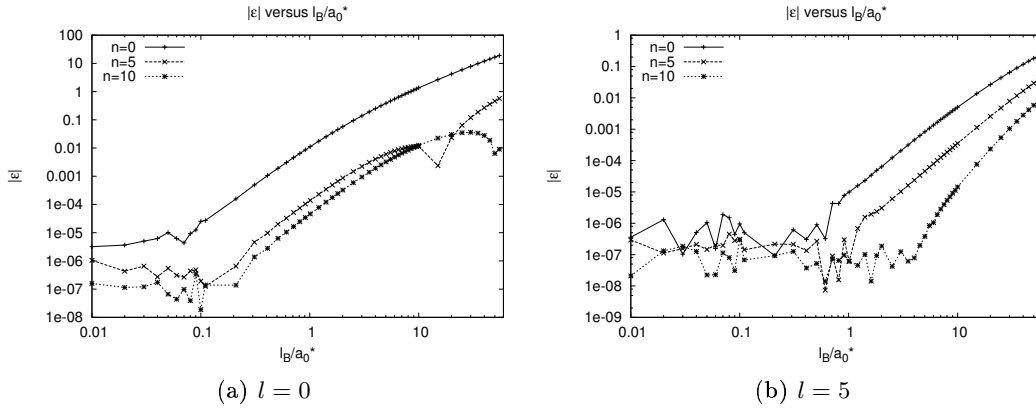


**Figure 4.2.9:** From Fig. 4.2.8, but here we consider the three dimensional case. If we carefully compare two and three dimensions we can see that the relative error in three dimensions is less for a given  $l_b/a_0^*$ . This is also shown in Fig 4.2.10 and can be explained by the decrease of freedom. When the electrons reside in two dimensions the relative motion is restricted thereby forcing the electrons closer and making the interaction stronger.

viable option for Coulomb problems where  $l_B/a_0^*$  is sufficiently small as it require less computational efforts than various diagonalization techniques. Observe the dip in error for the highest states. This is unexplained at the time of writing, but it is probably

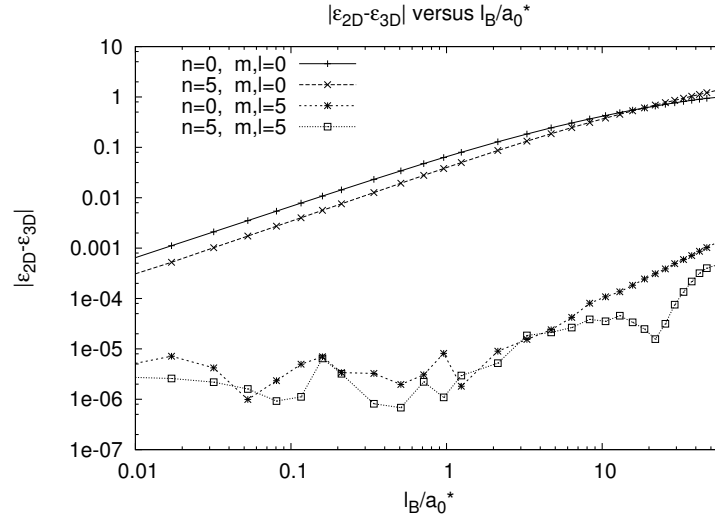


**Figure 4.2.10:** Relative error difference between two and three dimensions for each combination of  $n$  and  $m, l$ . This figure sheds light on two important properties of our system. For higher  $m, l$  values, we have less restriction on the position of the electrons and they can be further apart, thus lowering the interaction. As a consequence the perturbative error decreases. We also observe that for high  $l_B/a_0^*$ , the error difference between two and three dimensions is large compared to small  $l_B/a_0^*$ . This is a consequence of the restrictions laid upon the electrons in two dimensions. When they are smeared down in two dimensions there is a greater probability for them being closer to each other than in three dimensions. This increases the interaction, making the perturbative error bigger for two dimensions.

due to the summation of the perturbation series.

So far in this chapter we have discussed various schemes for calculating the complicated relative motion. Exact diagonalization turned out to be the best method as accuracy and flexibility is a major concern. In the next section we will list the diagonalization results in two and three dimensions for different choice of  $n$  and  $m, l$ .

### 4.3 Diagonalization results

We have carefully analyzed the numerical methods and it is now time to put them to good use. In this section we summarize the diagonalization results using the techniques discussed in the previous sections. Eigenvalues for the total system are listed in Table 4.4-4.7 for two dimensions, while Table 4.8-4.11 lists the results for three dimensions. The exact diagonalized energies  $E$  and the second order perturbed energies  $E'$  are given for  $l_B/a_0^*$ . For  $l_B/a_0^* = 10, 100$  the accuracy obtained by second order perturbation theory were too low in both two and three dimensions to be listed. The center-of-mass quantum numbers  $N = 0$  and  $M, L = 0$  where used during calculations. We have excluded the spin splitting, the  $m\hbar\omega_B$  and  $M\hbar\omega_B$  terms. They are merely additive constants. Only the ten first  $n$  are listed along with different values of  $m, l$  and  $l_B/a_0^*$ . As discussed in Sec. 4.2, the second order perturbation theory gives acceptable agreement for  $l_B/a_0^* = 0.01$ . For higher values of  $l_B/a_0^*$  the accuracy gets worse. Note

that for a given  $l_B/a_0^*$ , the perturbation theory gives better agreement when increasing  $m$  or  $l$ . This has to do with the relative electron-electron distance. When increasing  $m$  or  $l$  the electrons can be further apart and the interaction becomes weaker than for  $m = 0$  or  $l = 0$ .

$l_B/a_0^*$	0.01			
$m$	0		5	
$n$	$E/\hbar\omega$	$E'/\hbar\omega$	$E/\hbar\omega$	$E'/\hbar\omega$
0	2.017672	2.017656	7.004365	7.004361
1	4.013282	4.013277	9.004186	9.004180
2	6.011348	6.011347	11.004031	11.004027
3	8.010181	8.010174	13.003897	13.003896
4	10.009355	10.009354	15.003782	15.003782
5	12.008740	12.008736	17.003685	17.003681
6	14.008243	14.008246	19.003592	19.003590
7	16.007844	16.007844	21.003509	21.003508
8	18.007508	18.007505	23.003434	23.003434
9	20.007219	20.007215	25.003365	25.003365
10	22.006957	22.006961	27.003306	27.003302

**Table 4.4:** Lowest eigenvalues in two dimensions for  $m = 0, 5$  and  $l_B/a_0^* = 0.01$ . The diagonalized eigenvalues are labeled  $E$ , while the eigenvalues obtained using second order perturbation theory are labeled  $E'$ .

$l_B/a_0^*$	0.1			
$m$	0		5	
$n$	$E/\hbar\omega$	$E'/\hbar\omega$	$E/\hbar\omega$	$E'/\hbar\omega$
0	2.170701	2.170394	7.043581	7.043575
1	4.131206	4.131249	9.041765	9.041767
2	6.112746	6.112788	11.040245	11.040248
3	8.101315	8.101352	13.038939	13.038943
4	10.093282	10.093302	15.037806	15.037803
5	12.087186	12.087202	17.036794	17.036793
6	14.082335	14.082354	19.035886	19.035889
7	16.078354	16.078367	21.035068	21.035072
8	18.074989	18.075006	23.034319	23.034327
9	20.072110	20.072118	25.033643	25.033645
10	22.069591	22.069597	27.033006	27.033015

**Table 4.5:** From Table 4.4, but now for  $m = 0, 5$  and  $l_B/a_0^* = 0.1$ .

In Sec. 3.1.1 and 3.1.2 we plotted Fock-Darwin spectra. For the sake of comparison it would be preferable to develop the same kind of spectra for the numerical diagonalization with interaction included. For a two dimensional, non-interacting quantum dot

$l_B/a_0^*$	1			
$m$	0		5	
$n$	$E/\hbar\omega$	$E'/\hbar\omega$	$E/\hbar\omega$	$E'/\hbar\omega$
0	3.320053	3.086113	7.431916	7.431830
1	5.148342	5.159534	9.414600	9.414555
2	7.034804	7.058200	11.399955	11.399928
3	8.952925	8.973895	13.387309	13.387292
4	10.890248	10.907872	15.376208	15.376204
5	12.840222	12.855060	17.366362	17.366350
6	14.799023	14.811698	19.357506	19.357501
7	16.764288	16.775280	21.349480	21.349485
8	18.734446	18.744118	23.342170	23.342171
9	20.708437	20.717042	25.335451	25.335454
10	22.685474	22.693214	27.329244	27.329251

**Table 4.6:** From Table 4.4, but now for  $m = 0, 5$  and  $l_B/a_0^* = 1$ .

$l_B/a_0^*$	10		100	
$m$	0	5	0	5
$n$	$E/\hbar\omega$	$E/\hbar\omega$	$E/\hbar\omega$	$E/\hbar\omega$
0	8.821806	10.995593	34.181240	34.758886
1	10.585394	12.877493	35.920815	36.512759
2	12.375899	14.772193	37.667653	38.273712
3	14.188776	16.677455	39.421444	40.041442
4	16.020389	18.591561	41.181908	41.815668
5	17.867843	20.513186	42.948790	43.596107
6	19.728798	22.441228	44.721802	45.382512
7	21.601359	24.374829	46.500719	47.174621
8	23.483983	26.313275	48.285293	48.972223
9	25.375390	28.255971	50.075292	50.775079
10	27.274505	30.202437	51.870515	52.582985

**Table 4.7:** From Table 4.4, but now for  $m = 0, 5$  and  $l_0/a_0 = 10, 100$ . Results for perturbation theory were not printed as the accuracy were too low, see Sec. 4.2 for details.

Eq. (3.1.21) gives the energy as

$$\frac{E}{\hbar\omega_0} = (2n + |m| + 1) \sqrt{1 + \frac{\omega_B^2}{\omega_0^2}} + m \frac{\omega_B}{\omega_0}. \quad (4.3.1)$$

Adding the correction term in two dimensions from Eq. (4.1.9) yields the matrix elements

$$\left( \frac{E}{\hbar\omega_0} \right)_{n'n} = (2n + |m| + 1) \sqrt{1 + \frac{\omega_B^2}{\omega_0^2}} + m \frac{\omega_B}{\omega_0} + \frac{l_B}{2a_0^*} \frac{\omega}{\omega_0} I_{n'n}^{2D}, \quad (4.3.2)$$

$l_B/a_0^*$	0.01			
$l$	0		5	
$n$	$E/\hbar\omega$	$E'/\hbar\omega$	$E/\hbar\omega$	$E'/\hbar\omega$
0	3.011267	3.011268	8.004171	8.004168
1	5.009408	5.009397	10.004008	10.004008
2	7.008362	7.008365	12.003872	12.003871
3	9.007674	9.007675	14.003753	14.003753
4	11.007165	11.007165	16.003652	16.003649
5	13.006775	13.006767	18.003553	18.003557
6	15.006441	15.006442	20.003473	20.003474
7	17.006174	17.006170	22.003399	22.003398
8	19.005941	19.005938	24.003325	24.003329
9	21.005740	21.005735	26.003261	26.003265
10	23.005558	23.005557	28.003201	28.003206

**Table 4.8:** Lowest eigenvalues in three dimensions for  $l = 0, 5$  and  $l_B/a_0^* = 0.01$ . The diagonalized eigenvalues are labeled  $E$ , while the eigenvalues obtained using second order perturbation theory are labeled  $E'$ .

$l_B/a_0^*$	0.1			
$l$	0		5	
$n$	$E/\hbar\omega$	$E'/\hbar\omega$	$E/\hbar\omega$	$E'/\hbar\omega$
0	3.111312	3.111282	8.041656	8.041647
1	5.093421	5.093417	10.040052	10.040051
2	7.083337	7.083347	12.038698	12.038693
3	9.076552	9.076549	14.037530	14.037515
4	11.071513	11.071513	16.036482	16.036479
5	13.067559	13.067561	18.035553	18.035555
6	15.064336	15.064340	20.034725	20.034723
7	17.061634	17.061638	22.033968	22.033968
8	19.059322	19.059325	24.033280	24.033277
9	21.057315	21.057312	26.032643	26.032642
10	23.055530	23.055535	28.032061	28.032055

**Table 4.9:** From Table 4.8, but now for  $l = 0, 5$  and  $l_B/a_0^* = 0.1$ .

where

$$\omega = \sqrt{\omega_0^2 + \omega_B^2}. \quad (4.3.3)$$

The integral  $I_{n'n}^{2D}$  is defined in Eq. (4.1.17). Since  $l_B$  depends on  $\omega$  we need to collect the constant factors in front of the matrix into one expression. By writing

$$\frac{l_B}{a_0^*} \frac{\omega}{\omega_0} = \frac{e^2 m^*}{4\pi\epsilon\epsilon_0 \hbar^2} \sqrt{\frac{\hbar\omega}{\omega_0^2}}, \quad (4.3.4)$$



$l_B/a_0^*$	1			
$l$	0		5	
$n$	$E/\hbar\omega$	$E'/\hbar\omega$	$E/\hbar\omega$	$E'/\hbar\omega$
0	4.000038	3.972762	8.413250	8.413185
1	5.880322	5.878811	10.397889	10.397853
2	7.801196	7.802764	12.384757	12.384726
3	9.743691	9.745630	14.373306	14.373288
4	11.699278	11.701106	16.363187	16.363179
5	13.663510	13.665155	18.354152	18.354144
6	15.633831	15.635295	20.345986	20.345990
7	17.608627	17.609938	22.338577	22.338573
8	19.586842	19.588024	24.331785	24.331781
9	21.567744	21.568813	26.325523	26.325524
10	23.550788	23.551772	28.319736	28.319731

**Table 4.10:** From Table 4.8, but now for  $l = 0, 5$  and  $l_B/a_0^* = 1$ .

$l_B/a_0^*$	10		100	
$l$	0	5	0	5
$n$	$E/\hbar\omega$	$E'/\hbar\omega$	$E/\hbar\omega$	$E'/\hbar\omega$
0	9.350610	11.855797	34.687119	35.377642
1	11.117484	13.746849	36.426850	37.134252
2	12.911140	13.746849	38.173834	38.897900
3	14.727020	17.561329	39.927787	40.668284
4	16.561527	19.481307	41.688408	42.445121
5	18.411763	19.481307	43.455427	44.228109
6	20.275391	23.340689	45.228587	46.017031
7	22.150540	25.278381	47.007646	47.811620
8	24.035661	27.220488	48.792359	49.611651
9	25.929483	29.166513	50.582516	51.416898
10	27.830936	31.115991	52.377881	53.227148

**Table 4.11:** From Table 4.8, but now for  $l = 0, 5$  and  $l_B/a_0^* = 10, 100$ . Results for perturbation theory were not printed as the accuracy were too low, see Sec. 4.2 for details.

and defining

$$l_0 = \sqrt{\frac{\hbar}{m^*\omega_0}}, \quad (4.3.5)$$

we get

$$\frac{l_B}{a_0^*} \frac{\omega}{\omega_0} = \frac{l_0}{a_0^*} \sqrt{\frac{\omega}{\omega_0}}. \quad (4.3.6)$$

We substitute Eq. (4.3.6) into Eq. (4.3.2), and use the definitions of  $\omega$ ,  $\omega_B$  and  $\omega_0$  from

App. A.7.1 to get the matrix elements

$$\left(\frac{E}{\hbar\omega_0}\right)_{n'n}^{2D} = (2n + |m| + 1) \sqrt{1 + \frac{\omega_B^2}{\omega_0^2}} + m \frac{\omega_B}{\omega_0} + \frac{l_0}{2a_0^*} I_{n'n}^{2D} \left(1 + \frac{\omega_B^2}{\omega_0^2}\right)^{1/4}. \quad (4.3.7)$$

The same expression can easily be developed for three dimensions by adding the interacting correction to Eq. (3.1.41). This gives the matrix elements

$$\left(\frac{\epsilon_r}{\hbar\omega_0}\right)_{n'n}^{3D} = \left(2n + l + \frac{3}{2}\right) \sqrt{1 + \frac{\omega_B^2}{\omega_0^2}} + m \frac{\omega_B}{\omega_0} + \frac{l_0}{2a_0^*} I_{n'n}^{3D} \left(1 + \frac{\omega_B^2}{\omega_0^2}\right)^{1/4}. \quad (4.3.8)$$

The integrals  $I_{n'n}^{3D}$  is defined in Eq. (4.1.28) and (4.1.17) respectively. By using the same matrix diagonalization as before we can evaluate the relative energy  $E/\hbar\omega_0$  in both two and three dimensions and plot them to form Fock-Darwin spectra. The results can then be compared with the non-interacting case in Sec. 3.1.1. Four two-dimensional Fock-Darwin spectra are plotted in Fig. 4.3.11, one for each value of  $l_0/a_0^*$ . We clearly

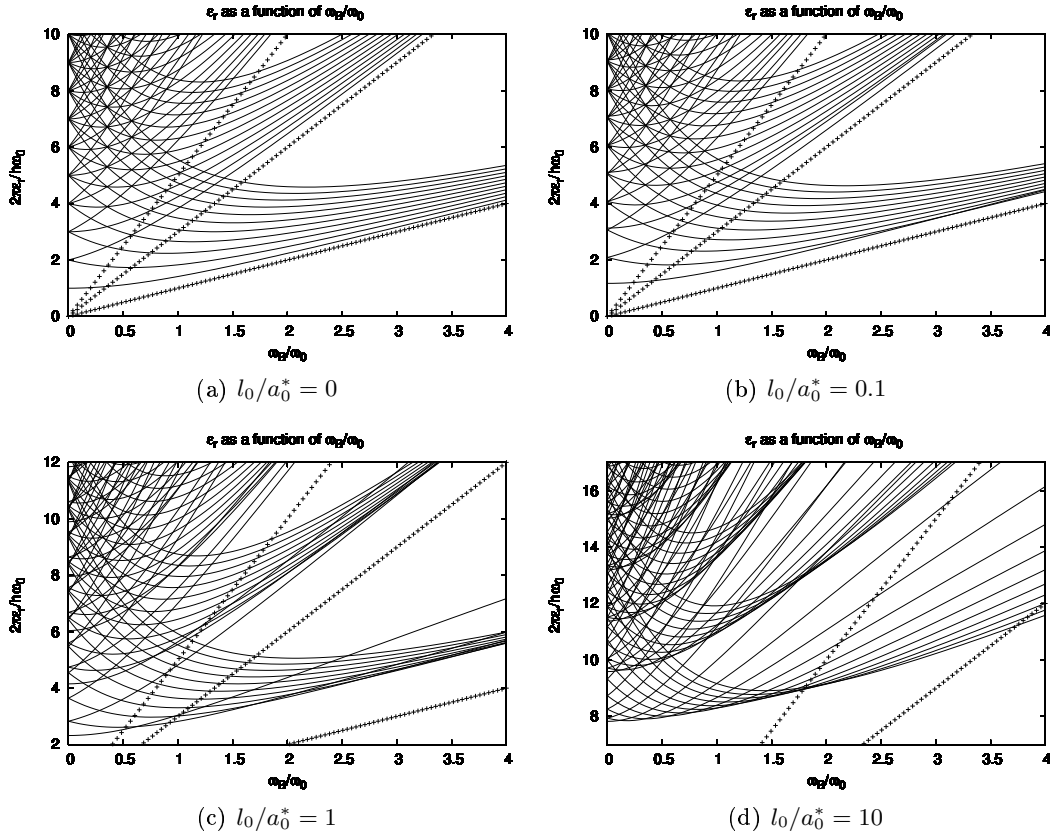


**Figure 4.3.11:** Fock-Darwin spectrum in two dimensions. The relative energy  $\epsilon_r$  is plotted against  $l_0/a_0^*$ . As  $l_B/a_0^*$  increases the lowest energy levels start to break out from the Landau bands. At  $l_B/a_0^*$  an almost complete breakdown can be observed.

see the same behavior as in Fig. 3.1.1 for  $l_0/a_0^* = 0$ . This is expected since  $l_0/a_0^* = 0$  makes the interaction disappear. When we increase  $l_B/a_0^*$ , a breaking of the Landau levels can be observed. The lines with pluses are the limits where the magnetic field

goes to infinity. For  $l_0/a_0^* = 0.1$  and  $l_0/a_0^* = 1.0$  only the lowest levels seem to break the Landau behavior we observed in the non-interacting case. For  $l_0/a_0^* = 10$  we have almost a complete breakdown. Without the interaction the particles have no problem resting in the Landau levels as the magnetic field increases. By adding the interaction one gets repulsion between the particles, and if we try to increase the magnetic field, their energy increases as they get closer to each other. The reason why the lowest levels break down first is because of confinement. For the lowest lying states, the particles are more tightly bound due to the quantum numbers  $n$  and  $m$ . Hence, the interaction is stronger and we get breakdown at the lowest lying states before a breakdown of the higher states becomes apparent. A breakdown of the higher levels will be unveiled by increasing the magnetic field even more.

Similar behavior is observed in Fig. 4.3.12 which shows the three dimensional Fock-Darwin spectrum for the same  $l_0/a_0^*$  values as for two dimensions. Observe how much more complicated the spectrum is for  $l_0/a_0^* = 1, 10$ . This is due to the added degeneracy. As we discussed in the last section, the interaction becomes stronger in two dimensions. This can be seen if we compare Figs. 4.3.11(c) and 4.3.12(c), where the lowest level seem to break the Landau levels faster in two dimensions. As the magnetic field increases, a stronger interaction would push the levels higher up in energy.

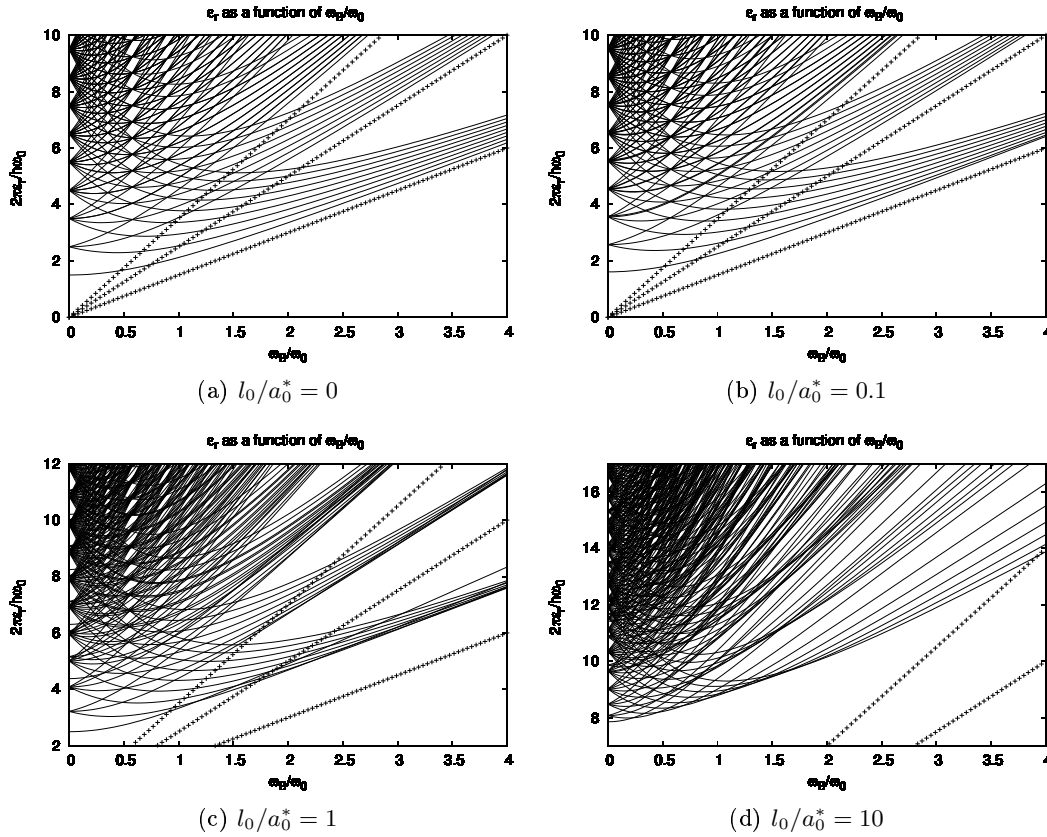


**Figure 4.3.12:** Fock-Darwin spectrum in three dimensions. The relative energy  $\epsilon_r$  is plotted against  $l_0/a_0^*$ . As  $l_B/a_0^*$  increases the lowest energy levels start to break out from the Landau bands. At  $l_B/a_0^*$  an complete breakdown can be observed

We have developed a complete comparison between two and three dimensional harmonic oscillators. First we looked at the single particle harmonic oscillators and then we added the interaction term. This gave us a different Fock-Darwin spectrum, especially for strong interactions. We will now consider quantum dots with several particles. The structure needs to be analyzed as quantum dots often contain more than two electrons. It would be reasonable to believe that the complexity increases with electron number. Understanding the structure of multi-particle quantum dots gives us more in depth knowledge about the artificial atoms.

## Chapter 5

# Structure of quantum dots in laboratory basis

The center-of-mass and relative, hereafter CM-rel, separation we employed in the last chapter is an excellent way to treat two-particle problems. However when we want to include several particles we run into problems with this basis. We have no clean way of describing several particles in the CM-rel notation, unless we include a modified center of mass and relative motion between each particle. The center-of-mass term would be very complicated as the particle number increases. Hence we need to change basis. We need to transform the CM-rel coordinates to what we will refer to as laboratory coordinates or lab coordinates. Before we work out the transformations we need to outline the many-particle scheme and define the lab basis.

In the next section we will define the many-particle basis in terms of single-particle eigenvectors, which will be related via a Slater determinant of harmonic oscillator eigenvectors. The same section also covers single-particle classification in the shell model. When this is done we set up an effective two-particle interaction model space by employing Lee-Suzuki transformations. This model space will be defined by single-particle harmonic oscillator shells. Then we work out the transformation from the CM-rel to the lab basis. At the end we will include a brief note about the OSMC and results for four, six and eight particles.

### 5.1 Many-particle basis for the shell model

This section discuss how to construct and define a fermionic many-particle basis in terms of single-particle eigenvectors. We will also define the harmonic oscillator shells used in the shell model. Let us first define the many particle wave function as

$$\Psi = \Psi(x_1, \dots, x_N), \quad (5.1.1)$$

where  $N$  is the particle number, while  $x_i$ ,  $i = 1 \dots N$  contains both space and spin degrees of freedom for particle  $i$ . One usually defines  $x = (\vec{r}, s)$ , where  $\vec{r}$  and  $s$  are spatial and spin coordinates, respectively. In this thesis we only consider identical

particles. Exchanging two coordinates in the wave function should not change the observables of the system, so it is reasonable to assume

$$\langle \Psi_{jk} | O | \Psi_{jk} \rangle = \langle \Psi_{kj} | O | \Psi_{kj} \rangle, \quad (5.1.2)$$

where  $O$  is the operator of the observables and

$$\Psi_{jk} = \Psi(x_1, \dots, x_j, \dots, x_k, \dots, x_N), \quad (5.1.3)$$

$$\Psi_{kj} = \Psi(x_1, \dots, x_k, \dots, x_j, \dots, x_N). \quad (5.1.4)$$

Defining the permutation operator  $P_{jk}$  with the following properties

$$P_{jk} | \Psi_{jk} \rangle = | \Psi_{kj} \rangle, \quad (5.1.5)$$

and

$$P_{jk}^2 | \Psi_{jk} \rangle = | \Psi_{jk} \rangle. \quad (5.1.6)$$

We then have

$$P_{jk}^2 = 1, \quad (5.1.7)$$

and

$$P_{jk} = P_{jk}^{-1}. \quad (5.1.8)$$

Using the permutation operator Eq. (5.1.2) can be written

$$\langle \Psi | O | \Psi \rangle = \langle \Psi | P_{jk}^\dagger O P_{jk} | \Psi \rangle, \quad (5.1.9)$$

where  $P_{jk}$  must have the property

$$O = P_{jk}^\dagger O P_{jk}. \quad (5.1.10)$$

This should be valid for all  $O$ . Taking  $O = 1$  gives the relation

$$P_{jk}^\dagger = P_{jk}. \quad (5.1.11)$$

Multiplying Eq. (5.1.10) by  $P_{jk}$  from the left gives the commutator

$$[O, P_{jk}] = 0. \quad (5.1.12)$$

The observables must commute with  $P_{jk}$ . Taking  $O$  as the Hamiltonian operator we see that any solution of the Schrödinger equation are also eigenfunctions of  $P_{jk}$ . Defining the eigenvalues of the  $P_{jk}$  operator as

$$P_{jk} | \Psi \rangle = \epsilon_{jk} | \Psi \rangle, \quad (5.1.13)$$

where  $\epsilon_{jk}$  is the eigenvalue of  $P_{jk}$ . Multiplying from the left with  $P_{jk}$  gives

$$P_{jk}^2 | \Psi \rangle = \epsilon_{jk}^2 | \Psi \rangle. \quad (5.1.14)$$

From Eq. (5.1.7) we see that

$$\epsilon_{jk} = \pm 1 \quad (5.1.15)$$

Let us now define symmetric and antisymmetric eigenfunctions. If

$$P_{jk}|\Psi\rangle = |\Psi\rangle, \quad (5.1.16)$$

we call the eigenfunctions symmetric, while for

$$P_{jk}|\Psi\rangle = -|\Psi\rangle, \quad (5.1.17)$$

the eigenfunctions are called antisymmetric. We label them  $|\Psi_S\rangle$  and  $|\Psi_A\rangle$  respectively. The Hilbert space only has antisymmetric or symmetric eigenvectors. This is called the symmetry postulate. For antisymmetric and symmetric eigenvectors we call the particles fermions and bosons respectively. Electrons are fermions as their spin is equal to half of an odd integer. This is a result from quantum field theory, see for example [Peskin and Schroeder; 1995]. Assume that our operator  $O$  is a many-body operator and can be defined as

$$O = \sum_i^N o_i, \quad (5.1.18)$$

where  $N$  is the number of particles. The single particle eigensolutions are then

$$o|\psi_n\rangle = e_n|\psi_n\rangle. \quad (5.1.19)$$

By assuming that we can write the many-particle eigenvector as a product of single-particle eigenvectors,  $|\Psi\rangle$  can be written

$$|\Psi\rangle = \prod_i^N |\psi_i\rangle. \quad (5.1.20)$$

From the presumption that the many-particle eigenvectors can be separated into single-particle eigenvectors. Using the antisymmetric permutation, the many-fermion eigenvector can be written as

$$|SD\rangle = \frac{1}{\sqrt{N!}} \begin{vmatrix} \psi_{n_1}(x_1) & \cdots & \psi_{n_1}(x_N) \\ \vdots & & \vdots \\ \psi_{n_N}(x_1) & \cdots & \psi_{n_N}(x_N) \end{vmatrix}. \quad (5.1.21)$$

This determinant is called the Slater determinant and it is labeled  $|SD\rangle$  by convention. The total antisymmetric eigenfunction will be expanded in a basis given by Slater determinants. From the properties of determinants we see that Eq. (5.1.21) vanish if  $n_i = n_j$  for  $i \neq j$ , The same thing happens if  $x_i = x_j$  for  $i \neq j$ . We can summarize these two properties as

- Two fermions with the same spin projection cannot be at the same point.
- Two fermions cannot be in the same quantum state.

These two properties outline an important principle in quantum mechanics called the Pauli exclusion principle.

We will now develop the usual classification of single-particle states used in the shell model. Together with the Slater determinant they will serve as building blocks for the many-particle basis. A central part of the classification is of course the quantum numbers, but the parity is also important. A parity operator has several similarities with the permutation operators discussed above, but their main intention is different. A permutation operator exchanges two particles, while the parity operator changes the coordinate sign. We define the parity operator in Cartesian coordinates as

$$P_{\pm}\Psi(\vec{r}) = \Psi(-\vec{r}), \quad (5.1.22)$$

where  $\Psi(\vec{r})$  is the eigenvector of the system. Transforming to spherical polar coordinates the Cartesian transformation

$$\vec{r} \rightarrow -\vec{r}, \quad (5.1.23)$$

$$x \rightarrow -x, \quad (5.1.24)$$

$$y \rightarrow -y, \quad (5.1.25)$$

$$z \rightarrow -z, \quad (5.1.26)$$

implies

$$r \rightarrow r, \quad (5.1.27)$$

$$\theta \rightarrow \pi - \theta, \quad (5.1.28)$$

$$\phi \rightarrow \pi + \phi. \quad (5.1.29)$$

This can be seen from the transformations in App. A.3. We observe that the radial eigenfunctions are not affected by the parity operator. Applying the parity operator to the spherical eigenfunction from Eq. (3.1.34) yields

$$P_{\pm}\Omega(\theta, \phi) = (-1)^l\Omega(\theta, \phi), \quad (5.1.30)$$

where  $P_+ = 1$  and  $P_- = -1$ . Since the many-particle eigenvector can be made by multiplying the single-particle eigenvectors, the total parity is defined as

$$P_{\pm}^T = (-1)^{l_1+l_2+\dots+l_N}, \quad (5.1.31)$$

where  $N$  is the total number of particles. A single particle state is usually described by the notation

$$nC_j(P_{\pm}), \quad (5.1.32)$$

where  $n$  is the principal quantum number and  $j$  the quantum number of the total angular momentum defined as  $j = l + s$ . The total angular momentum is discussed in Sec. 3.1.2 along with the orbital quantum number defined as  $l$ . The electron spin  $s$  take values  $s = \pm 1/2$ . The character  $C$  is associated with the value of  $l$ . For the first values of  $l$  the definition of  $C$  is given in Table 5.1. This gives the needed description of the single particle states. In analogy with Sec. 3.1.2 we list the first five filled shells in Table 5.2. The filled shells  $S$  are obtained by filling all shells up to the limit  $N = 2n + l$ . The dimensions of the model space is also listed as  $d_{M_P}$  and it can be defined as  $d_{M_P} = S + 1$ .



$l$	$C$
0	$s$
1	$p$
2	$d$
3	$f$
4	$g$

**Table 5.1:** Definition of the character  $C$  describing the orbital shells  $l$ . Also used in the OSMC for this thesis.

Moving to the many particle case we can classify each single particle by the notation developed here. In Sec. 4.1 we suggested a matrix cutoff at  $n \approx 80$  to obtain convergent

$d_{M_P}$	$N$	$n$	$l$	$j$	$D$	$nC_j(P_{\pm})$	$S$
1	0	0	0	1/2	2	$0s_{1/2}(+)$	2
2	1	0	1	3/2	4	$0p_{3/2}(-)$	8
		0	1	1/2	2	$0p_{1/2}(-)$	
3	2	0	2	5/2	6	$0d_{5/2}(+)$	20
		0	2	3/2	4	$0d_{3/2}(+)$	
		1	0	1/2	2	$1s_{1/2}(+)$	
4	3	0	3	7/2	8	$0f_{7/2}(-)$	40
		0	3	5/2	6	$0f_{5/2}(-)$	
		1	1	3/2	4	$1p_{3/2}(-)$	
		1	1	1/2	2	$1p_{1/2}(-)$	
5	4	0	4	9/2	10	$0g_{9/2}(+)$	70
		0	4	7/2	8	$0g_{7/2}(+)$	
		1	2	5/2	6	$1d_{5/2}(+)$	
		1	2	3/2	4	$1d_{3/2}(+)$	
		2	0	1/2	2	$2s_{1/2}(+)$	
6	5	0	5	11/2	12	$0h_{11/2}(-)$	112
		0	5	9/2	10	$0h_{9/2}(-)$	
		1	3	7/2	8	$1f_{7/2}(-)$	
		1	3	5/2	6	$1f_{5/2}(-)$	
		2	1	3/2	4	$2p_{3/2}(-)$	
		2	1	1/2	2	$2p_{1/2}(-)$	

**Table 5.2:** Overview of the first single particle shells up to  $d_{M_P} = 6$ . Here we have used  $N = 2n + l$ , where  $n$  is the principal and  $l$  the orbital quantum number. For a given model space we have  $S$  possible single particle states. The degeneracy of each shell is labeled  $D$ . The nuclear shell notation is also given as  $nC_j(P_{\pm})$ .

eigenvalues for the lowest states. Working with such matrices is not a problem for a modern computer. If we now use these states to generate two particle interactions between several particles, and at the same time include a sufficient selection of orbital quantum numbers we understand that the matrices we are going to diagonalize becomes too large. Thus it is important to reduce the size of the interacting matrix and at the

same time conserve its eigenvalues. A common way of reducing the Hilbert space even further than the matrix cut-off at  $n \approx 80$  is a method worked out by Lee and Suzuki [Lee and Suzuki; 1980]. It is basically a collection of similarity transformations. We will now discuss the three different methods developed by Lee and Suzuki and decide which method is best suited for our problem.

## 5.2 Effective interactions and the transformation to laboratory basis

In this section we are going to develop an effective interaction by limiting the Hilbert space even further than the previously discussed matrix cut-off, see Sec. 4.1.3 for details. The main idea is to use similarity transformations which conserves the eigenvalues of the eigenproblem. Three different transformations are worked out, their main principle are the same, to restrict the Hilbert space to a smaller model space yielding what we will call an effective interaction. Let us again start with the Schrödinger equation

$$H|\Psi\rangle = E|\Psi\rangle. \quad (5.2.1)$$

A matrix  $H$  is said to be similar to  $H'$  if there exists an invertible matrix  $X$  such that  $H' = X^{-1}HX$ . A similarity transformation of the Schrödinger equation will not change its eigenvalues. To see this, multiply Eq. (5.2.1) with  $X^{-1}$  from the left. This gives

$$X^{-1}H|\Psi\rangle = EX^{-1}|\Psi\rangle, \quad (5.2.2)$$

inserting  $XX^{-1}$  between  $H$  and  $|\Psi\rangle$  results in

$$X^{-1}HX|\Psi_P\rangle = E|\Psi_P\rangle. \quad (5.2.3)$$

Where the eigenvectors  $|\Psi_P\rangle = X^{-1}|\Psi\rangle$  have been modified, but the eigenvalues are still intact. Let us now define a model space  $M_P$  and its complementary space  $M_Q$ , where  $P$  and  $Q$  are the projection operators defined in Fig. 5.2.1. The transformation  $X$  should bring us from  $|\Psi_P\rangle$  to  $|\Psi\rangle$ . The projection operators follow the restrictions  $P + Q = 1$ ,  $P^2 = P$ ,  $Q^2 = Q$  and  $PQ = QP = 0$ . Assume that we can separate the Hamiltonian into an exactly solvable  $H_0$  and a perturbation  $H_1$  as

$$H = H_0 + H_1. \quad (5.2.4)$$

In our case  $H_1$  would be the Coulomb interaction. Since  $H_0$  should be valid across the Hilbert space, we define

$$[H_0, P] = 0, \quad (5.2.5)$$

$$[H_0, Q] = 0, \quad (5.2.6)$$

and

$$[QH_0, P] = 0. \quad (5.2.7)$$

Let us now do a similarity transformation of  $H$ , such that

$$H' = X^{-1}HX. \quad (5.2.8)$$

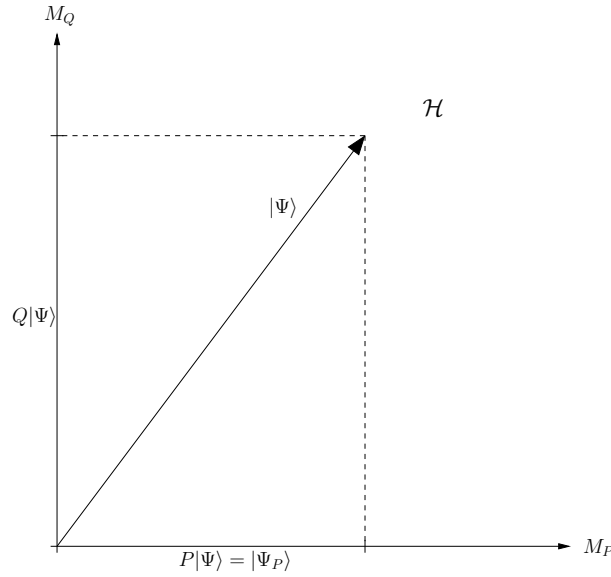


**Figure 5.2.1:** Decomposition of the Hilbert space  $\mathcal{H}$ . The projection operator  $P$  projects  $|\Psi\rangle$  down on the model space  $M_P$ , while  $Q$  projects  $|\Psi\rangle$  on the complement  $M_Q$ .

The transformation should bring  $H$  onto the  $M_P$  and  $M_Q$  space. If we decompose the transformed Hamiltonian we get

$$H' = PH'P + QH'P + PH'Q + QH'Q. \quad (5.2.9)$$

We would like to obtain an effective Hamiltonian acting only within the  $M_P$  space, that is

$$H_e = PH'P. \quad (5.2.10)$$

If we ensure that

$$QH'P = 0, \quad (5.2.11)$$

and

$$PH'Q = 0, \quad (5.2.12)$$

then the decomposition of  $H'$  has only the components  $PH'P$  and  $QH'Q$ . The component acting in the  $M_Q$  space is the excluded states and it is important that the  $|\Psi\rangle$  states of interest to us have a minimal overlap with the components in the  $M_Q$  space. To determine the similarity transformation Eqs. (5.2.11) and (5.2.12) are used. We will not give a proof here, but  $X$  is not uniquely determined. Hence, different choices of  $X$  gives us different effective Hamiltonians. During a similarity transformation, the eigenvalues of the effective Hamiltonian will overlap with the eigenvalues of  $H$ . Remember that the Hamiltonians in our case are hermitian and obey

$$H'^{\dagger} = X^{\dagger} H X^{-\dagger}. \quad (5.2.13)$$

Since  $H'^{\dagger} = H'$  we see that  $X^{\dagger} = X^{-1}$ , thus  $X$  is unitary. Let us introduce an  $X$  that satisfies this and can be expanded in powers of another transformation  $\omega$ . We define

$$X = e^{\omega}, \quad (5.2.14)$$

where we want  $\omega$  to be an operator that transforms an  $M_P$  state to an  $M_Q$  state. If  $\omega$  works on a state in  $M_P$ , namely  $P|\Psi\rangle$  we have

$$\omega P|\Psi\rangle = |\phi\rangle, \quad (5.2.15)$$

where  $|\phi\rangle$  is a state in the  $M_Q$  space. If we now project this state onto  $M_P$  we see that

$$P\omega P = 0, \quad (5.2.16)$$

and

$$Q\omega Q = 0. \quad (5.2.17)$$

Suppose  $\omega$  transforms a state in  $M_Q$ . The transformed state would still be in  $M_Q$ , that is

$$\omega Q|\Psi\rangle = Q|\Psi\rangle. \quad (5.2.18)$$

Projecting this down to  $M_P$  would yield

$$P\omega Q = 0. \quad (5.2.19)$$

The last transformation we need to consider is  $Q\omega P$ . Projecting Eq. (5.2.15) onto the  $M_Q$  space we see that

$$Q\omega P = \omega. \quad (5.2.20)$$

The exponential of an operator can be expanded just like the regular exponential as a power series. This gives

$$e^{\omega} = 1 + \omega + \frac{\omega^2}{2!} + \frac{\omega^3}{3!} + \dots \quad (5.2.21)$$

From Eq. (5.2.20) this expansion simplifies as

$$\omega^n = 0, \quad n > 1, \quad (5.2.22)$$

and we are left with

$$e^{\omega} = 1 + \omega. \quad (5.2.23)$$

Substituting  $X = 1 + \omega$  and  $X^{-1} = 1 - \omega$  into Eq. (5.2.11) gives

$$QH P - Q\omega P H P + Q H Q \omega P - Q\omega P H Q \omega P = 0, \quad (5.2.24)$$

inserting  $H = H_0 + H_1$  and Eq. (5.2.7) yields

$$QH_1 P - Q\omega P H P + Q H Q \omega P - Q\omega P H_1 Q \omega P = 0, \quad (5.2.25)$$

due to the nature of the projection operators, this equation is equivalent to

$$QH_1 P - \omega P H P + Q H Q \omega - \omega P H_1 Q \omega = 0. \quad (5.2.26)$$

The effective Hamiltonian can be rewritten in terms of  $\omega$  as

$$H_e = PHP + PVQ\omega. \quad (5.2.27)$$

For later use we also need

$$QH'Q = QHQ - \omega PH_1Q. \quad (5.2.28)$$

Rayleigh-Schrödinger perturbation theory can be expressed in the same basis as discussed above. This is proved by Bloch [Bloch; 1958]. Define the wave operator  $\Omega$  as

$$\Omega = P + \omega. \quad (5.2.29)$$

This wave operator should bring us from  $|\Psi'\rangle$  to  $|\Psi\rangle$ . We see that

$$\Omega|\Psi_P\rangle = |\Psi_P\rangle + \omega|\Psi_P\rangle, \quad (5.2.30)$$

that is, components in the  $M_P$  and  $M_Q$  space respectively. In other words

$$\Omega|\Psi_P\rangle = |\Psi\rangle. \quad (5.2.31)$$

Also note that  $\Omega$  performs the same operation as the similarity transformation  $X$ . Substituting Eq. (5.2.30) into Eq. (5.2.11) using  $H' = (1 - \Omega + P)H(1 + \Omega - P)$  gives

$$QH\Omega P - Q\Omega H\Omega P = 0, \quad (5.2.32)$$

inserting  $P + Q = 1$  in the last term between the first  $\Omega$  and  $H$  yields

$$QH\Omega P - Q\Omega PH\Omega P - Q\Omega QH\Omega P = 0, \quad (5.2.33)$$

where the last term is zero due to Eq. (5.2.17). Removing the leftmost  $P$  in the two remaining terms gives

$$QH\Omega - Q\Omega PH\Omega = 0, \quad (5.2.34)$$

substituting  $H = H_0 + H_1$  yields,

$$Q(\Omega PH_0 - H_0)\Omega = QH_1\Omega - Q\Omega PH_1\Omega, \quad (5.2.35)$$

inserting  $P + Q = 1$  after each  $H_0$  and observing that the unperturbed energy in  $M_P$  space can be written as  $PH_0P = PE_0P = E_0P$  we get

$$(E_0(\Omega - P) - QH_0Q)\Omega = QH_1\Omega - Q\Omega PH_1\Omega. \quad (5.2.36)$$

Unitary transformations have the property  $\Omega^2 = 1$ , this can also be seen from Eq. (5.2.31). The sum  $\Omega^2 - P\Omega$  can now be written as

$$\Omega^2 + P\Omega = 1 - P, \quad (5.2.37)$$

and Eq. (5.2.36) can be rewritten as the Bloch equation [Bloch; 1958]

$$\Omega = P + \frac{1}{E_0 - QH_0Q}QH_1\Omega - \frac{1}{E_0 - QH_0Q}Q\Omega PH_1\Omega. \quad (5.2.38)$$

Before we continue to express  $\Omega$  as a recursive series, we define the  $M_P$  space effective interaction as

$$V_e = H_e - PH_0P. \quad (5.2.39)$$

Substituting Eq. (5.2.27) into the equation above give us the effective interaction as

$$V_e = PH_1P + PH_1Q\omega. \quad (5.2.40)$$

We now expand  $\Omega$  as

$$\Omega = \sum_{n=0}^{\infty} \Omega^{(n)}, \quad (5.2.41)$$

and define  $\Omega^{(0)} = P$ . Let  $\Omega^{(n)}$  contain an n-th order expression of  $H_1$  in such way that we can rewrite Eq. (5.2.38) as a recursive sum

$$\Omega^{(q)} = \frac{1}{E_0 - QH_0Q}QH_1QH_1\Omega^{(q-1)} - \frac{1}{E_0 - QH_0Q}QH_1 \sum_{n=0}^{q-1} \Omega^{(n)}PH_1\Omega^{(q-n-1)}. \quad (5.2.42)$$

By using Eq. (5.2.40) we can rewrite Eq. (5.2.42) as

$$V_e^{(q)} = PH_1 \frac{1}{E_0 - QH_0Q}H_1\Omega^{(q-1)} - \sum_{n=0}^{q-1} PH_1 \frac{1}{E_0 - QH_0Q}\Omega^{(n)}V_e^{(q-n-1)}, \quad (5.2.43)$$

where we have expanded

$$V_e = \sum_{q=0}^{\infty} V_e^{(q)}, \quad (5.2.44)$$

and

$$V_e^{(q)} = PH_1\Omega^{(q)}. \quad (5.2.45)$$

We have now obtained a recurrence relation which generates the perturbative Rayleigh-Schrödinger terms. Using Eq. (5.2.45) we would determine  $\Omega^{(q)}$  which again would determine  $\Omega$ . When  $\Omega$  is determined we could solve Eq. (5.2.26). Note that if  $E_0 - QH_0Q \rightarrow 0$  the perturbation diverges and  $\Omega$  would cause the eigenvector to diverge. This can happen if the spectrum in the  $M_P$  and the  $M_Q$  spaces overlap.

We will now illustrate an alternative way worked out by Lee and Suzuki [Lee and Suzuki; 1980], called vertex renormalization. This method is based on an iteration scheme developed from Eq. (5.2.26). Details on the advantages and convergence rates will not be covered in detail in this thesis, see [Lee and Suzuki; 1980] and references therein for discussions. It can be showed that if the vertex renormalization scheme converges, it converges to the energy closest to the chosen starting energy,  $E_0$ . While the method discussed previously will converge to the energy with the most overlap in the  $M_P$  space. What we want to do is to linearize Eq. (5.2.26) by making it iterative. But let us first rewrite and rearrange Eq. (5.2.26) as

$$QH_1P - \omega PH_1P = E_0\omega P - QHQ\omega + \omega PH_1Q\omega, \quad (5.2.46)$$

where we used  $H = H_0 + H_1$  and  $PH_0P = E_0P$ . Inserting  $Q + P = 1$  between  $E_0$  and

$\omega$ , using Eq. (5.2.16) and Eq. (5.2.20) we get

$$QH_1P - \omega PH_1P = (E_0 - QHQ)\omega + \omega PH_1Q\omega. \quad (5.2.47)$$

To linearize the equation, index the leftmost  $\omega$ 's by  $q-1$  and the rightmost by  $q$ . This gives

$$QH_1P - Q\omega^{q-1}PH_1P = (E_0 - (QH_0Q + QH_1Q - Q\omega^{q-1}PH_1Q))\omega^q, \quad (5.2.48)$$

where we again used  $H = H_0 + H_1$ , Eq. (5.2.16) and the substitution  $P + Q = 1$ . This equation can be simplified by defining

$$V_Q^{q-1} = (1 - \omega^{q-1})H_1, \quad (5.2.49)$$

which can be thought as the effective interaction in  $M_Q$  space, though with a slightly different  $\omega$  factor than in Eq. (5.2.28). Substituting Eq. (5.2.49) into Eq. (5.2.48), rearranging and rewriting  $\omega^{q-1}P = \omega^{q-1}$  yields

$$\omega^q = \frac{1}{E_0 - QH_0Q - QV_Q^{q-1}Q} QV_Q^{q-1}P. \quad (5.2.50)$$

Substituting this into Eq. (5.2.40) gives

$$V_e^q = PH_1P + PH_1Q \frac{1}{E_0 - QH_0Q - QV_Q^{q-1}Q} QV_Q^{q-1}P. \quad (5.2.51)$$

We can make the expression seem more symmetric if we rewrite  $PV_Q^{q-1}P = P = PH_1P$  and  $PV_Q^{q-1}Q = PH_1Q$ . Doing this, Eq. (5.2.51) can be written as

$$V_e^q = PV_Q^{q-1}P + PV_Q^{q-1}Q \frac{1}{E_0 - QH_0Q - QV_Q^{q-1}Q} QV_Q^{q-1}P. \quad (5.2.52)$$

Observe that  $V_e^q$  is not hermitian. This can be fixed by yet another similarity transformation, see [Suzuki and Okamoto; 1995] for in depth discussions of its form. Comparing Eq. (5.2.52) with the perturbed  $V_e^q$  from Eq. (5.2.43) we see that the divergence in the perturbation can be controlled by introducing a renormalization. Hence the name self-energy renormalization method or vertex renormalization method.

However in this thesis we will use a direct way of calculating  $\omega$ . This can be done as the complete set of eigenvectors are known. Suppose we operate  $\omega$  on an  $M_P$  state  $|\Psi_P\rangle$  as

$$\omega|\Psi_P\rangle = \sum_i \omega|\Psi_i\rangle\langle\Psi_i|\Psi_P\rangle, \quad (5.2.53)$$

where we have used the completeness relation. The  $|\Psi_i\rangle$  state satisfies  $H'|\Psi_i\rangle = E_i|\Psi_i\rangle$ . Multiplying Eq. (5.2.53) with an  $M_Q$  state from the left gives

$$\langle\Psi_Q|\omega|\Psi_P\rangle = \sum_i \langle\Psi_Q|\omega|\Psi_i\rangle\langle\Psi_i|\Psi_P\rangle. \quad (5.2.54)$$

As long as  $\langle \Psi_Q | \omega$  has an inverse, we see from Eq. (5.2.18) that  $\omega | \Psi_Q \rangle = | \Psi_Q \rangle$ . We can then simplify Eq. (5.2.54) as

$$\langle \Psi_Q | \omega | \Psi_P \rangle = \sum_{i=0}^{d_{MP}} \langle \Psi_Q | \Psi_i \rangle \langle \Psi_i | \Psi_P \rangle. \quad (5.2.55)$$

We would now choose our model space dimension,  $d_{MP}$ . In practice this is the same as to choose the number of states we want to include in the model space. This set would then restrict the sum over  $i$ . From Eq. (5.2.40),  $\omega$  could be calculated. However, our effective Hamiltonian is still non-hermitian. And to obtain real eigenvalues it can be made hermitian by yet another similarity transformation of the form

$$H_e^{herm} = \{P(1 + \omega^\dagger \omega P)\}^{1/2} H_e \{P(1 + \omega^\dagger \omega P)\}^{-1/2}, \quad (5.2.56)$$

see [Suzuki; 1982] for details.

We have so far developed an effective interaction, which was needed to reduce the number of available states in a many-particle calculation. In the last section we defined the lab basis, but one thing remains, the transformation to the lab basis. Moshinsky transformations are used to transform the CM-rel basis to the lab basis. The transformation coefficients used in the Moshinsky transformations are worked out in detail in App. A.4 and will not be reprinted here due to their complexity. We basically need two recursion relation to find any needed coefficient. The total lab eigenvector will be a composite of single particle eigenvectors put together by a Slater determinant, see Sec. 5.1 for details. As in Sec. 3.1.2 we need to replace the single particle orbital momentum by the total angular momentum. And we would like to write the two particle eigenvectors as

$$|jm, n_1 j_1, n_2 j_2\rangle = \sum_{m_1 m_2} |n_1 j_1 m_1, n_2 j_2 m_2\rangle \langle n_1 j_1 m_1, n_2 j_2 m_2 | jm, n_1 j_1, n_2 j_2\rangle, \quad (5.2.57)$$

where  $|n_1 j_1 m_1\rangle$  are the single particle eigenfunctions. It is intuitive to seek a form like Eq. (5.2.57) since the total angular momenta  $j$  commutes with the Hamiltonian. The last coefficient in Eq. (5.2.57) is called the Clebsch-Gordon coefficient and it is non-zero only if

$$|j_1 - j_2| \leq j \leq j_1 + j_2, \quad (5.2.58)$$

and

$$m = m_1 + m_2, \quad (5.2.59)$$

see [Shankar; 1994] for details.

After the transformations have been done, the ground state energies should remain the same. Indeed every energy level is conserved during the transformations to the laboratory basis. The diagonalization in the laboratory basis is done using the Oslo Shell Model Code, or OSMC [Engeland; 1990-2006]. At the time of writing, development of a two dimensional version of OSMC is in process. Only three dimensional results are considered in the following sections. Before we list diagonalization results for four, six and eight particles, we will briefly discuss the OSMC.



### 5.3 Brief notes about OSMC and the diagonalization process

In this thesis we make use of the OSMC to obtain the eigenvalues. This method is very effective and has been developed to solve nuclear systems. The diagonalization scheme used in OSMC is basically the Lanczos algorithm. See App. A.1 for details. The Lanczos algorithm is very handy if we want to calculate the lowest eigenvalues of large, sparse and symmetric eigenproblems. The Lanczos is used to tridiagonalize the operator matrix and the extreme eigenvalues are often converged before the tridiagonalization is complete. A standard tridiagonal solver are then be used to diagonalize and obtain the eigenvalues, see [Press et al.; 2002] and [Golub and Loan; 1996] for a details.

First, we set up the interaction matrix in the center-of-mass and relative coordinates using a jj-scheme. This is due to the OSMC specifications. Ideally we want an ls-scheme for our problem. Then, using Lee-Suzuki transformation explained in Sec.5.2 we reduce the Hilbert space to our model space  $M_P$  as shown in Fig. 5.3.2. After the Lee-Suzuki transformation is complete we employ the Moshinsky transfor-

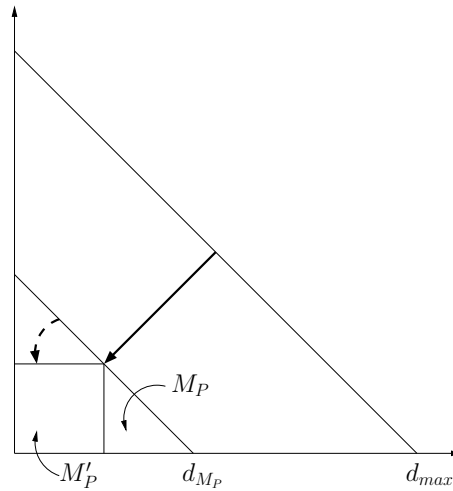


**Figure 5.3.2:** The maximum number of allowed harmonic oscillator states is  $d_{max} = 2n + l$ , where  $n$  and  $l$  are the single particle principal and orbital quantum numbers respectively. This number is limited by the matrix cut-off discussed in Sec. 4.1.3. After the Lee-Suzuki transformation marked by the thick solid line we get an effective model space  $M_P$  of size  $d_{M_P}$ . Due to the OSMC specification we had to cut the model space  $M_P$  even more. This restriction is marked by the stippled line. We then obtain the final model space  $M'_P$ . Note however that this restriction excludes states that should have been included when initiating the diagonalization process of the OSMC.

mation explained in App. A.4. As a consequence of the specifications of the OSMC we need a quadratic model space. The triangular model space  $M_P$  introduces not only a cut in state, but also energy. A simple two dimensional example can be made. Lets assume that we have two states available. See Fig. 5.3.3 for an illustration. If we restrict our model space to the triangle we exclude the  $|22\rangle$  state, so excitation to this state is not allowed. Our model space  $M_P$  then reduces to  $M'_P$  where the states

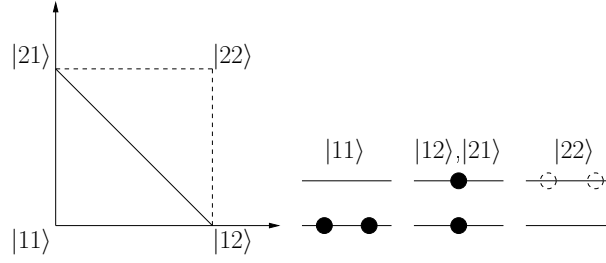


**Figure 5.3.3:** A simple example of a triangular versus quadratic model space. The triangular model space puts restrictions not only on the states, but also on the energy. Observe that excitations to the state  $|22\rangle$  is not allowed in the triangular model space.

$M_P - M'_P$  are excluded by a brute force cut. Using  $M'_P$  in the diagonalization process introduces errors as some states are excluded. The error should become more severe for the excited states. One might ask why we did not transform our Hilbert space to a quadratic model space in the first place. The Moshinsky transformation is diagonal in the center-of-mass motion only with a triangular model space, which simplifies calculations considerably. When all the transformations are done, the effective interaction is fed into the OSMC and a Lanczos iteration is started. The result is a tridiagonal matrix which is diagonalized using an implicit QR algorithm. One thing that makes the OSMC stand out is that it represents the eigenstates by computer bits. This speeds up the calculations considerably, but limits the number of states available. Due to the 64-bit limitations in the present OSMC, we cannot increase the model space beyond four shells. If we were to use five shells we would have 70 different single particle states, which is too big for 64-bit word length. The model space and its shells are shown in Table 5.2. Utilizing a 128-bit word length would increase the model space dimensions to include both the fifth and the sixth shell. In this thesis we only consider model spaces with dimension two, three and four.

We have done almost all the analysis needed to start the many particle simulations. However, one important step is left. To compare energies in the CM-rel diagonalization with the OSMC diagonalization. This is done in the next section.

## 5.4 Comparison of energies using OSMC and CM-rel diagonalization

The eigenvalues before and after the transformation to the laboratory basis should be invariant. Thus doing the diagonalization in either one has to yield the same results. At least as long as the numerics are stable. Comparing the eigenvalues are difficult as the basis of the states in the OSMC becomes rather large when we increase the model space. The ground state is easy to identify and is made by placing two particles in  $0s_{1/2}(+)$  state, each with opposite spin due to the Pauli principle. The Pauli principle is explained in Sec. 5.1. Let us define the difference

$$|\epsilon| = |E(OSMC) - E(CM - rel)|, \quad (5.4.1)$$

where  $E(OSMC)$  and  $E(CM - rel)$  are the eigenvalues obtained using OSMC and CM-rel diagonalization, respectively. In Table 5.3 we have compared the ground states obtained using the CM-relative and OSMC diagonalization as a function of model space  $M_P$ . From the table we see that as we increase the model space, the difference decreases. Going from a model space of dimension three to four yields a difference of the order of  $10^{-3}$  or smaller for most values of  $l_B/a_0^*$ . But at  $l_B/a_0^* = 10$  the difference is about one or two orders of magnitude larger than for smaller values of  $l_B/a_0^*$ . This is probably caused by the need of a larger model space as the interaction strength increases. This seem intuitive as a larger interaction would spread the particles, which leads to excitations. As a consequence, we need a larger model space to include these excitations. The forced cut imposed to meet the current OSMC specification also worsens this scenario by further limiting the number of states. Comparing higher energy levels needs careful examination. This is difficult and there is a risk of having levels that are off due to the forced cut mentioned in Sec. 5.3. Hence only a limited choice of eigenvalues are listed in Table 5.3.

	$l_B/a_0^*$	$d_{M_P}$		
		2	3	4
$E_0$	0.01	3.0113	3.0113	3.0113
	0.1	3.1118	3.1114	3.1114
	1	4.0416	4.0046	4.0027
	10	9.5715	9.5557	9.4036
$E_{CM}$	0.01	3.011276	3.011276	3.011276
	0.1	3.111322	3.111322	3.111322
	1	4.000025	4.000025	4.000025
	10	9.350621	9.350621	9.350621
$ \epsilon $	0.01	$2.4 \times 10^{-5}$	$2.4 \times 10^{-5}$	$2.4 \times 10^{-5}$
	0.1	$4.78 \times 10^{-4}$	$7.8 \times 10^{-5}$	$7.8 \times 10^{-5}$
	1	$4.16 \times 10^{-2}$	$4.58 \times 10^{-3}$	$2.68 \times 10^{-3}$
	10	$2.21 \times 10^{-1}$	$2.05 \times 10^{-1}$	$5.3 \times 10^{-2}$

**Table 5.3:** Ground state eigenvalues for a three dimensional two-electron quantum dot. Quantum numbers  $n = l = m = 0$  for different values of the model space dimension  $d_{M_P}$  are listed. We clearly see a convergent behavior. Going from three to four shells yields a difference of the order of  $10^{-3}$  or greater except for  $l_B/a_0^* = 10$ .

To sum things up we can say that an acceptable convergence is obtained for the ground state, except when  $l_B/a_0^* = 10$ . It would be fruitful to increase the model space to the fifth and sixth shell and observe the difference in eigenvalues. Hopefully, the convergence is better. In the next section we will finally move on and consider four, six and eight particles.

## 5.5 Many-particle diagonalization using OSMC

During the last chapters and sections we have developed the theory and discussed different numerical tools for the two body interactions. Extending the simulations in

the OSMC is easy as long as we disregard the higher order corrections for three particle interaction. For a discussion about three particle interactions see (FINN REF). In the last section we saw that the OSMC gave us convergence for the ground states with an acceptable accuracy except for  $l_B/a_0^*$  values larger than one. Hence only  $l_B/a_0^* = 0.01, 0.1, 1$  values are considered in this section. In the last section we only investigated the convergence of the ground state. However, it is important that at least the lower lying levels converge within our model space. As the particle number increases the number of states explodes and it is difficult to follow a given state to observe convergence. In this thesis we only consider the lowest lying states. Following is a discussion of the lowest diagonalized eigenvalues for a four-, six- and eight-particle quantum dot.

### 5.5.1 Four particles

Let us start the many-particle simulations by looking at the four-particle quantum dot. In addition to the ground state defined by  $E_0$  we define two more excited states in Table 5.4. The total parity is defined in Sec. 5.1, while  $J$  is the total angular momentum. For more than two particles,  $J$  will be a combinations of the two-particle total angular momentums, see [Edmonds; 1957] for details. The integer  $p$  keeps track of the excited states for each given configuration of  $P_\pm^T$  and  $J$ . For example, if  $p = 0$  it gives the lowest eigenvalue of the given  $P_\pm^T$  and  $J$ . States that do not have a stable expectation value of  $J(J+1)$  are rejected from the results. The lowest eigenvalue listed would be the ground state. To determine the convergence rate we define the deviation

	$P_\pm^T$	$J$	$p$
$E_0$	+	2	0
$E_1$	-	2	0
$E_2$	+	1	1

**Table 5.4:** Definition of ground state and excited states used for convergence tests for four electrons. The integer  $p$  tells us which excited state it is within the given configuration of the total parity  $P_\pm^T$  and the total angular momentum  $J$ . If for example  $p = 0$ , the lowest eigenvalue for the given  $P_\pm^T$  and  $J$  is listed.

$$|\epsilon|_{i \rightarrow j} = |E(OSMC \ d_{M_P, j}) - E(OSMC \ d_{M_P, i})|. \quad (5.5.1)$$

In Table 5.5 we list the eigenvalues of the excited states along with the deviation for four particles. We clearly see that if we increase the model space from three to four the deviation increases by almost an order of magnitude, indicating a convergence for  $l_B/a_0^* = 0.01, 0.1$ . For  $l_B/a_0^* = 1$  one observes  $|\epsilon|_{2 \rightarrow 3} > |\epsilon|_{3 \rightarrow 4}$ , but it cannot be taken as a sign of convergence. This indicates that we need to increase our model space when  $l_B/a_0^*$  gets sufficiently large. The ground state seems to have converged already at two model shells. The degeneracy is higher than in the two-particle case, as we the number of available quantum numbers are higher.

Even though convergence can be observed it is by no means very good, at least not on a general basis. It would be interesting to see what the fifth and the sixth model

spaces would give. This is however out of scope in this thesis. Let us now increase the complexity and move on to the case of six particles.

	$l_B/a_0^*$	$d_{MP}$			$ \epsilon _{2 \rightarrow 3}$	$ \epsilon _{3 \rightarrow 4}$
		2	3	4		
$E_0$	0.01	8.0526	8.0526	8.0526	0	0
	0.1	8.2513	8.5221	8.5202	$2.708 \times 10^{-1}$	$1.9 \times 10^{-3}$
	1	13.0135	12.8451	12.6925	$1.684 \times 10^{-1}$	$1.526 \times 10^{-1}$
$E_1$	0.01	9.0451	9.0451	9.0451	0	0
	0.1	9.4492	9.4494	9.4476	$2.0 \times 10^{-4}$	$1.8 \times 10^{-3}$
	1	13.3078	13.3311	13.1635	$2.33 \times 10^{-2}$	$1.676 \times 10^{-1}$
$E_2$	0.01	10.0479	10.0419	10.0418	$6.0 \times 10^{-3}$	$1.0 \times 10^{-4}$
	0.1	10.4772	10.4182	10.4158	$5.9 \times 10^{-2}$	$2.4 \times 10^{-3}$
	1	14.589	14.0667	13.9578	$5.223 \times 10^{-1}$	$1.089 \times 10^{-1}$

**Table 5.5:** Four-electron quantum dot eigenvalues  $E_0, E_1, E_2$  and deviation  $|\epsilon|_{i \rightarrow j}$  defined in Tab. 5.4 and Eq. (5.5.1). At  $l_B/a_0^* = 0.01, 0.1$  almost an order of magnitude improvement from three to four shells can be observed. The convergence gets worse as we increase  $l_B/a_0^*$ , indicating that we need a larger model space. This is a consequence of a stronger interaction and probably the forced cut introduced in Sec. 5.1

### 5.5.2 Six particles

Here we will follow the same procedure as in the last section, but now for six particles. The chosen states are shown in Table 5.6. In Table 5.7 we list the energies and the

	$P_{\pm}^T$	$J$	$p$
$E_0$	+	0	0
$E_1$	−	1	0
$E_2$	+	0	1

**Table 5.6:** Definition of ground state and excited states used for convergence tests for six electrons. The integer  $p$  keep track of the excited states within each given configuration of the total parity  $P_{\pm}^T$  and the total angular momentum  $J$ . If for example  $p = 0$ , the lowest eigenvalue for the given  $P_{\pm}^T$  and  $J$  is listed.

deviation from Eq. (5.5.1). Signs of convergence can be seen. Note that in the case of  $l_B/a_0^* = 0.01$  and  $d_{MP} = 3$ , the excited states  $E_1$  and  $E_2$  cannot be extracted. This is probably a failure in the diagonalization algorithm as the off-diagonal elements are small. One order decrease in deviation can be observed for the two excited states when  $l_B/a_0^* = 0.1$ . For six particles we see that going from three to four model shells decreases the deviation by one order less than for four particles. This is not surprising as we add more particles into the same volume. As a consequence, the average interaction is stronger and the convergence suffers. The importance of the interaction can also be observed by looking at the energy levels as we increase  $l_B/a_0^*$ . The energy spacing between two values of  $l_B/a_0^*$  is much larger than for four particles, thus indicating that

the interaction becomes more important as we increase the particle number. Even though the data very limited there seems to be that the low lying states converge slower than the excited states as we increase  $l_B/a_0^*$ . This is a consequence of the relative electron-electron motion discussed earlier in this thesis. Particles in excited states can be further apart, thus decreasing the interaction. Let us now look at an eight-particle quantum dot.

	$l_B/a_0^*$	$d_{MP}$			$ \epsilon _{2 \rightarrow 3}$	$ \epsilon _{3 \rightarrow 4}$
		2	3	4		
$E_0$	0.01	13.128	13.1279	13.1278	$1.0 \times 10^{-4}$	$1.0 \times 10^{-4}$
	0.1	14.2634	14.2595	14.2499	$3.9 \times 10^{-3}$	$9.6 \times 10^{-3}$
	1	25.1176	24.7839	24.0629	$3.339 \times 10^{-1}$	$7.116 \times 10^{-1}$
$E_1$	0.01	14.1222	14.1194	14.1194	$2.8 \times 10^{-3}$	0
	0.1	15.2165	15.1881	15.1806	$2.84 \times 10^{-2}$	$7.5 \times 10^{-3}$
	1	25.6629	25.219	24.6015	$4.439 \times 10^{-1}$	$6.175 \times 10^{-1}$
$E_2$	0.01	15.1213	15.1123	15.1122	$9.0 \times 10^{-3}$	$1.0 \times 10^{-4}$
	0.1	16.2076	16.1187	16.1118	$8.89 \times 10^{-2}$	$6.9 \times 10^{-3}$
	1	26.6236	25.7337	25.2358	$8.899 \times 10^{-1}$	$4.979 \times 10^{-1}$

**Table 5.7:** Six-electron quantum dot eigenvalues  $E_0, E_1, E_2$  and deviation  $|\epsilon|_{i \rightarrow j}$  defined in Tab. 5.6 and Eq. (5.5.1). At  $l_B/a_0^* = 0.01, 0.1$  almost an order of magnitude improvement from three to four shells can be observed. The convergence gets worse as we increase  $l_B/a_0^*$ . This is a consequence of a stronger interaction.

### 5.5.3 Eight particles

The final results will now be listed for eight particles. At this particle number we really start to hit computer limitations at a model space consisting of four shells. However, the OSMC has the possibility to restrict excitations by limiting the number of particles allowed at certain single particle excitation levels. To be able to get results for four shells we had to force the states  $0f_{7/2}(-)$  and  $0f_{5/2}(-)$  to contain zero particles. See Table 5.2 for an overview of the allowed single particle shells. For two and three shells no condition like this was enforced. The chosen states are shown in Table 5.8, while the results from the diagonalization is shown in Table 5.9. For the ground state  $E_0$  a slight increase of deviation can be observed with increasing model space. This is probably due to limitations on the number of available states, or it is a result of a stronger interaction due to smaller relative distance in the ground state. The ground state is the only possible configuration at a two shelled model space, see Table 5.2. Since this is the only possible configuration, the diagonalization requires less numerical work and should be more accurate. But this is a very limiting case. Comparing the six- and eight-electron quantum dot eigenvalues and  $\epsilon_{3 \rightarrow 4}$  shows an order decrease in  $\epsilon_{3 \rightarrow 4}$ , thus indicating a more severe convergence for eight particles. Due to the complexity this should not come as a surprise. At  $E_2$  we had certain problems identifying the states due to non acceptable  $J(J+1)$  expectation values. When this happens, there is an indication of problems with the Lanczos iteration which fails if there is a large number of degenerated states. An increased number of degenerate states could be a

consequence of the forced cut discussed in 5.3. The deviation between three and four shelled model space is stable in a sense that it is of the same order of magnitude for different energy levels.

The trend is more or less equal between four-, six- and eight-electron quantum dot. Increasing the interaction strength  $l_B/a_0^*$  results in a worse convergence. The energy spacing increases quite drastically when adding more electrons into the quantum dot due to the increasing importance of the interaction.

	$P_{\pm}^T$	$J$	$p$
$E_0$	+	0	0
$E_1$	-	2	0
$E_2$	+	2	1

**Table 5.8:** Definition of ground state and excited states used for convergence tests for eight particles. The integer  $p$  tells us which excited state it is with the given configuration of  $P_{\pm}^T$  and  $J$ .

	$l_B/a_0^*$	$d_{M_P}$			$ \epsilon _{2 \rightarrow 3}$	$ \epsilon _{3 \rightarrow 4}$
		2	3	4		
$E_0$	0.01	18.2340	18.2340	18.2337	0	$3.0 \times 10^{-4}$
	0.1	20.3302	20.3238	20.2976	$6.4 \times 10^{-3}$	$2.62 \times 10^{-2}$
	1	40.3464	39.8233	38.1288	$5.231 \times 10^{-1}$	$1.6945 \times 10^0$
$E_1$	0.01	$n/a$	19.2259	19.2257	$n/a$	$2.0 \times 10^{-4}$
	0.1	$n/a$	21.2457	21.2259	$n/a$	$1.98 \times 10^{-2}$
	1	$n/a$	40.1833	38.8647	$n/a$	$1.3186 \times 10^0$
$E_2$	0.01	$n/a$	20.2171	20.2169	$n/a$	$2.0 \times 10^{-4}$
	0.1	$n/a$	22.1596	22.1448	$n/a$	$1.48 \times 10^{-2}$
	1	$n/a$	40.4778	39.4486	$n/a$	$1.0292 \times 10^0$

**Table 5.9:** Eight-electron quantum dot eigenvalues  $E_0, E_1, E_2$  and deviation  $|\epsilon|_{i \rightarrow j}$  defined in Tab. 5.8 and Eq. (5.5.1). At  $l_B/a_0^* = 0.01, 0.1$  almost an order of magnitude improvement from three to four shells can be observed. The convergence gets worse as we increase  $l_B/a_0^*$ . This is a consequence of a stronger interaction. Excited states  $E_1$  and  $E_2$  are not available in a two shelled model space.

## Chapter 6

# Concluding remarks

This thesis started out with an overview of two-particle quantum dots, where we worked in the center-of-mass and relative basis. A harmonic oscillator basis was chosen as an approximation of the interacting basis. An exact analytic solution was then worked out, but only for limited values of the interaction strength. Comparing the ground states energies of both solutions gave surprisingly good results. We then diagonalized the problem and found that Gauss-Laguerre quadrature integration was preferred due to its fast convergence for smaller quantum numbers. The diagonalization of the relative part was done using Householder reductions and implicit QR shifts. Truncation of the relative matrix was carefully analyzed, for a given orbital quantum number an  $80 \times 80$  matrix gave convergence for the ten lowest eigenvalues. Perturbation theory was also considered, but found to be limited with regards to the interaction strength.

To compare the non-interacting and the interacting case, Fock-Darwin energy spectra was plotted for both cases. For the non-interacting case, the energy levels converged into Landau bands as we increased the magnetic field. This was also true for the interacting case, but only for low interaction strengths. When we increased the interaction strength, a breaking of the Landau levels could be seen. First at the lowest, then for all energy levels as the interaction strength was increased. This makes sense as a strong repulsive interaction is more sensitive to a confining magnetic field, thus increasing the systems energy. The lower states are often closer in space and their interaction would be stronger than for particles resting at higher states. As a consequence, the lowest lying states will be the first to break the Landau levels, which was observed in the Fock-Darwin plots.

The main goal of this thesis was to investigate if the OSMC [Engeland; 1990-2006] would be suited for many-particle quantum dot calculations. The OSMC solves an eigenproblem of a system by exact diagonalization. In most calculation done elsewhere, a mean field approximation is used. It is believed that exact diagonalization usually gives better results. However exact diagonalization involves complicated calculation routines and unless implemented efficiently they can be insolvable due to computation time. As far as we know, there has not been any work done which involves exact diagonalization and effective interaction of quantum dots.

The center-of-mass and relative basis did not suit a many-particle scenario. A



Moshinsky transformation [Moshinsky; 1959] was used to transform our system from center-of-mass and relative basis into the laboratory basis. Before we did the Moshinsky transformation we defined a new model space of effective interaction using Lee-Suzuki similarity transformations [Lee and Suzuki; 1980]. This had to be done as the complexity explodes as soon as we start adding more than two particles to the dot. The model space was chosen to be triangular to be compatible with the diagonal center-of-mass terms. The present OSMC needs a quadratic model space, so we had to force a strict cut of the model space. As a consequence the OSMC diagonalized with a modified model space without knowing it. This has obviously introduced errors, especially for higher lying states. However, convergence was present which indicates that OSMC could be a viable option for solving eigenproblems of quantum dots. A general trend could be seen. As we added more particles to the dot, the interaction became more important. The energy level spacing grew significantly when we went from six to eight particles, for example. We also observed that convergence could not be determined when the interaction strength became too large. Expanding the model space would unveil this region and hopefully show signs of convergence. When the interaction became small we had problems identifying certain states due to a non-convergent Lanczos iteration. This indicates high degeneracy, which is giving rise to problems with the orthogonality of the Lanczos iteration.

At this point it would be very interesting to rewrite the OSMC to accept a triangular model space. It would probably reduce errors by a significant margin, how much remains to be seen. Doing a transformation from center-of-mass and relative basis to lab basis in a quadratic model space is not an option as the center-of-mass transformation would give non-diagonal elements. As a consequence the OSMC model could not be used. Developing a two dimensional version of the OSMC and comparing results of many-particle diagonalization in two and three dimensions are important for future work.

At present the OSMC works in 64-bit word length. This limits the number of states that can be represented. Porting this to 128-bit should be possible and probably easy. Both the fifth and sixth model shell could then be included in calculation and we would have more data to analyze the convergence. We observed that a larger model space was necessary to observe convergence when the interaction strength became large. Special data types can also be written to go past 128-bit, but the performance setback should be investigated. The center-of-mass corrections have not been included in this thesis. They would give corrections to the system due to spurious states affecting the chosen model space. Computing time also restricts the choice of the number of particles and the model space. For eight particles with a model space of four, the diagonalization would take days to complete on a normal computer. Introducing a cut in energy, by excluding certain excited states reduces the computing time considerably. How a cut in energy would affect the convergence needs careful investigation.

The quantum dot simulations done in this thesis are based on a spherical symmetric harmonic oscillator potentials. This is seldom the case in experiments and exploring a deformed harmonic oscillator potential is important. However, analytic solutions to this problem does not exist. A very hot topic these days is the coupling of two quantum dots to form logical gates, see for example [Day; March 2006] and references therein. In such setups it is crucial to understand the time dependence of the system. Time

varying magnetic fields are also an interesting topic which needs investigation. To treat time development we would dissect our problem into time steps and diagonalize for each step, while adjusting time dependent parameters between each diagonalization. This, along with parallelization techniques should be investigated. Another interesting aspect is to compare results obtained from the exact diagonalization with Monte Carlo simulations and mean field theories. The eigenvectors from the OSMC could be used as trial wave functions in Monte Carlo simulations.

# Appendix A

## A.1 Lanczos methods

In this section we will develop a method that is an alternative to the Householder method used elsewhere in this thesis. An optimal way of finding eigenvalues and eigenvector is first to reduce the matrix to a simple form, often triangular and then start the iterative process. The Householder method is one of the most effective methods of reducing the matrix. An  $n \times n$  matrix is reduced to tridiagonal form by  $n - 2$  orthogonal transformations, see [Press et al.; 2002] for details. The operations needed go as  $2n^3/4$ . As the matrices becomes large, we will get performance issues with this method. In addition, the Householder reduction may give roundoff errors when the matrix elements vary over many orders of magnitude. If our matrix is sparse, the orthogonal transformation destroys the sparsity. As a result we get larger dense matrices during the reduction. In many cases only the extreme eigenvalues are of interest. This is also the case for this thesis. Doing a complete matrix diagonalization is simply not needed. The Lanczos algorithm is one of the most effective computational tools for searching few extreme eigenvalues and corresponding eigenvectors. The application in physics and mathematics are countless. In this section we will give a brief introduction to the Lanczos algorithm. At the end we will discuss convergence and its downsides.

Let us first assume that we have a large, sparse and symmetric matrix  $A \in \mathbb{R}^{n \times n}$  in the eigenproblem  $Ax = \lambda x$ . Then assume that only the extreme eigenvalues are of interest to us. Also note that symmetric matrices can be expressed as  $A = QDQ^T$ , where  $Q$  is an orthogonal matrix and  $D$  is a diagonal matrix containing the eigenvalues. Looking at the quotient

$$r(x) = \frac{\vec{x}^T A \vec{x}}{\vec{x}^T \vec{x}} \quad \vec{x} \neq 0, \quad (\text{A.1.1})$$

we observe that the maximum and minimum values of  $r(x)$  would be the eigenvalues  $\lambda_1(A)$  and  $\lambda_m(A)$  respectively. Now suppose  $Q_i = [q_1, \dots, q_i]$  is orthogonal. Define scalars  $M_i$  and  $m_i$  as

$$M_i = \lambda_1(Q_i^T A Q_i), \quad (\text{A.1.2})$$

$$m_i = \lambda_i(Q_i^T A Q_i). \quad (\text{A.1.3})$$

A new quotient is defined with eigenvector  $y$  to give

$$M_i = \max_{\vec{y} \neq 0} \frac{\vec{y}^T (Q_i^T A Q_i) \vec{y}}{\vec{y}^T \vec{y}}, \quad (\text{A.1.4})$$

$$m_i = \min_{\vec{y} \neq 0} \frac{\vec{y}^T (Q_i^T A Q_i) \vec{y}}{\vec{y}^T \vec{y}}. \quad (\text{A.1.5})$$

Comparing this with Eq. (A.1.1) would yield the following relations

$$M_i = \max_{\|\vec{y}\|_2=1} r(Q_i \vec{y}) \leq \lambda_1(A), \quad (\text{A.1.6})$$

$$m_i = \min_{\|\vec{y}\|_2=1} r(Q_i \vec{y}) \geq \lambda_m(A), \quad (\text{A.1.7})$$

where

$$\|\vec{y}\|_2 = \sqrt{\vec{y}^T \vec{y}}. \quad (\text{A.1.8})$$

The main purpose of the Lanczos algorithm is to generate the  $q_i$  in such way that  $M_i$  and  $m_i$  gets increasingly closer to  $\lambda_1$  and  $\lambda_m$ . The gradient of the quotient needs to be calculated. First we explicitly write out the quotient from Eq. (A.1.1) as

$$r(x) = \frac{\sum_{j=1}^n \sum_{k=1}^n A_{jk} x_j x_k}{\sum_{j=1}^n x_j^2}, \quad (\text{A.1.9})$$

where  $n$  is the number of components in  $\vec{x}$ . Taking the derivative with respect to  $x_q$  we get the expression

$$\frac{\partial r(x)}{\partial x_q} = \sum_{j=1}^n \sum_{k=1}^n A_{jk} x_j x_k \frac{\partial}{\partial x_q} \left( \frac{1}{\sum_{j=1}^n x_j^2} \right) + \frac{1}{\sum_{j=1}^n x_j^2} \frac{\partial}{\partial x_q} \left( \sum_{j=1}^n \sum_{k=1}^n A_{jk} x_j x_k \right), \quad (\text{A.1.10})$$

expanding and performing the derivatives yields

$$\frac{\partial r(x)}{\partial x_q} = -2 \sum_q \sum_k A_{qk} x_q x_k \frac{1}{\sum_q x_q^3} + \frac{1}{\sum_j x_j^2} \left( \sum_k A_{qk} x_k + \sum_j A_{jq} x_j \right). \quad (\text{A.1.11})$$

Because of the symmetry of  $A$  we combine the two last sums into one and the gradient can now be written as

$$\nabla r(x) = \frac{2}{\vec{x}^T \vec{x}} (A \vec{x} - r(x) \vec{x}). \quad (\text{A.1.12})$$

Suppose  $u_k \in \text{span}\{q_1, \dots, q_{i+1}\}$  is such that  $M_k = r(u_k)$ . We want to make sure  $M_{i+1} > M_i$ . This can be done by demanding that

$$\nabla r(u_i) \in \text{span}\{q_1, \dots, q_{i+1}\}, \quad (\text{A.1.13})$$

from where  $q_{i+1}$  can be determined. This can be ensured since  $r(x)$  increases most rapidly in the direction of the gradient. If  $v_i \in \text{span}\{q_1, \dots, q_{i+1}\}$  satisfies  $r(v_i) = m_i$  we demand

$$\nabla r(v_i) \in \text{span}\{q_1, \dots, q_{i+1}\}. \quad (\text{A.1.14})$$

Again, this can be assured since  $r(x)$  decreases most rapidly along its negative gradient. From Eq. (A.1.12) we see that

$$\nabla r(x) \in \text{span}\{q_1, \dots, q_i\}, \quad (\text{A.1.15})$$

which means that Eq. (A.1.13) and (A.1.14) are satisfied if

$$\text{span}\{q_1, \dots, q_i\} = \text{span}\{q_1, Aq_1, \dots, A^{i-1}q_1\}. \quad (\text{A.1.16})$$

This basis set is often called the Krylov subspace. We could then generate  $q_{i+1}$  if it satisfied

$$\text{span}\{q_1, \dots, q_{i+1}\} = \text{span}\{q_1, Aq_1, \dots, A^{i-1}q_1, A^i q_1\}. \quad (\text{A.1.17})$$

Finding  $q_i$  is now a straightforward job of finding the orthonormal basis of the Krylov subspace. Introducing the Krylov matrix as

$$K(A, q_1, i) = [q_1, Aq_1, \dots, A^{i-1}q_1], \quad (\text{A.1.18})$$

we see that the orthonormal basis of the Krylov subspace is just the column space of the Krylov matrix. If  $Q_i^T A Q_i = T_i$  where  $T$  is tridiagonal we can write Eq. (A.1.18) as

$$K(A, q_1, i) = Q[e_1, T e_1, \dots, T^{i-1} e_1], \quad (\text{A.1.19})$$

with

$$Q e_1 = q_1. \quad (\text{A.1.20})$$

Since  $A$  is symmetric, so is  $T$ . We define the off-diagonal elements of  $T$  as  $\{b_1, \dots, b_{i-1}\}$  and the diagonal elements as  $\{a_1, \dots, a_i\}$ . Doing this we can write out  $AQ = QT$  as

$$Aq_j = b_{j-1}q_{j-1} + a_j q_j + b_j q_{j+1}, \quad (\text{A.1.21})$$

where  $j = [1, \dots, i-1]$  and  $b_0 q_0 = 0$ . By using Eq. (A.1.21),  $q_{j+1}$  can be determined. When this is done,  $Q$  is known. The method will terminate when  $b_j q_{j+1} = 0$ . Then, we extract the eigenvalues of  $T$  by using an effective symmetric tridiagonal QR algorithm or any other effective diagonalization technique. If for some reason the  $Q$  matrix deviates and becomes non-orthogonal we have a problem. This is also the downside of the Lanczos procedure. As we generate the  $q_i$  we may run into roundoff errors which could imply that  $Q$  becomes non-orthogonal. There are several ways of controlling the orthogonality which we will not cover here. See for example [Golub and Loan; 1996] for details. The computing power of Lanczos methods should not be underestimated as long as our matrix is large and sparse. For an in dept review of effective and practical Lanczos algorithms see [Golub and Loan; 1996] for details. This reference also compares the Lanczos method and the Power method. The Lanczos method is far superior to the Power method as long as its orthogonality is controlled.

## A.2 Gauge transformations and invariance

Maxwell's equation [Goldstein et al.; 2002] are known from classical electromagnetics as

$$\nabla \cdot \vec{E} = \rho, \quad (\text{A.2.1})$$

$$\nabla \times \vec{E} = -\frac{1}{c} \frac{\partial \vec{B}}{\partial t}, \quad (\text{A.2.2})$$

$$\nabla \cdot \vec{B} = 0, \quad (\text{A.2.3})$$

$$\nabla \times \vec{B} = \frac{1}{c} \vec{J} + \frac{1}{c} \frac{\partial \vec{E}}{\partial t}, \quad (\text{A.2.4})$$

where  $\rho$  is the charge density,  $\vec{J}$  the vector current density.  $\vec{B}$  and  $\vec{E}$  are the magnetic and electric vector field respectively. Solving Eqs. (A.2.3) and (A.2.4) with respect to  $\vec{B}$  and  $\vec{E}$  results in

$$\vec{B} = \nabla \times \vec{A}, \quad (\text{A.2.5})$$

$$\vec{E} = -\nabla\phi - \frac{1}{c} \frac{\partial \vec{A}}{\partial t}. \quad (\text{A.2.6})$$

Here,  $\vec{A}$  is a vector potential while  $\phi$  is a scalar potential. They are at this time unknown, but should be a function of  $\vec{B}$  and  $\vec{E}$ . Now, consider the following transformation

$$\phi \rightarrow \phi' = \phi + \frac{1}{c} \frac{\partial h(\vec{x}, t)}{\partial t}, \quad (\text{A.2.7})$$

$$\vec{A} \rightarrow \vec{A}' = \vec{A} - \nabla h(\vec{x}, t), \quad (\text{A.2.8})$$

where  $h(\vec{x}, t)$  is an unknown arbitrary function, called the gauge function. If we put these transformations back into Eqs. (A.2.5) and (A.2.8) we see that  $\vec{E}$  and  $\vec{B}$  is unchanged, whatever  $h(\vec{x}, t)$  is. Since  $\vec{E}$  and  $\vec{B}$  is the only observables, we can chose  $h(\vec{x}, t)$  in any way we want, and still have invariant observables. These type of transformation is known as gauge transformations of second kind. As a consequence of this, all theories using the potentials  $\phi$  and  $\vec{A}$  should be gauge invariant, since the observables do not change. And to this date, there has not been a single experiment voiding a gauge invariance. This gives some rules to  $\phi$  and  $\vec{A}$ . If we insert the vector potentials into Eqs. (A.2.1) and (A.2.2) the following two equations restricts the choice of  $\vec{A}$  and  $\phi$  even more

$$-\nabla^2 \phi - \frac{1}{c} \frac{\partial}{\partial t} (\nabla \cdot \vec{A}) = \rho, \quad (\text{A.2.9})$$

$$\left( \frac{1}{c^2} \frac{\partial^2}{\partial t^2} - \nabla^2 \right) \vec{A} + \nabla \left( \frac{1}{c} \frac{\partial \phi}{\partial t} + \nabla \cdot \vec{A} \right) = \frac{1}{c} \vec{J}. \quad (\text{A.2.10})$$

We see that due to the freedom of Eqs. (A.2.7) and (A.2.8), we can choose

$$\nabla \cdot \vec{A} = 0, \quad (\text{A.2.11})$$

or

$$\nabla \cdot \vec{A} - \frac{1}{c} \frac{\partial \phi}{\partial t} = 0. \quad (\text{A.2.12})$$

The first one is called the Coulomb or transverse gauge, the second is the Lorentz gauge. The choice of gauge is not restricted to these two, there are many others, but the Lorentz and the Coulomb gauge are the most used. By a proper gauge function, we can go from a Lorentz gauge to a Coulomb gauge in general. The Coulomb gauge has severe problems in relativistic field calculations since we impose commutator relations between the fields to obey the canonical commutator relation. The manifest Lorentz invariance is also broken if we try to circumvent these problems. As a consequence, the Lorentz gauge is used due to its covariant form. In this thesis we use the Coulomb gauge, which in this special case is just the same as the Lorentz gauge. We only want a constant magnetic field which means that  $\rho$  and  $\vec{J}$  can be put to zero. If we impose the Coulomb gauge on Eq. (A.2.9), we see that the scalar potential  $\phi = 0$ . From the gauge condition we can choose  $\vec{A}$  to be symmetric. We only want a magnetic field along the  $z$ -axis and from Eq. (A.2.5) we see  $\vec{A}$  is potential with elements in  $x$  and  $y$  direction, zero otherwise. By choosing

$$\vec{A} = \frac{B}{2} \{-y, x, 0\}, \quad (\text{A.2.13})$$

we obtain  $B = B\vec{e}_z$  and gauge invariance is preserved.

### A.3 Coordinate transformations

Let us now develop the needed transformations from a Cartesian coordinate system to a polar one. First, we define what is called general curvilinear coordinates. Orthogonal coordinates will be used here. They cover cartesian, polar, spherical and several others. We assume that the functions used in the derivations are continuous and differentiable. Let us say that the vector  $\vec{r}(x_1, x_2, x_3, \dots)$  points at a point in space. Then this vector has its tangents as the most elementary basis. We can define them as  $\vec{e}_i = \partial\vec{r}/\partial x_i$  for  $i = 1, 2, 3, \dots$ . Each  $\vec{e}_i$  will be a tangent to each  $x_i$ -curve in a direction of increasing  $x_i$  values. If we now normalize these vectors we get

$$\vec{e}_i = \frac{1}{a_i} \frac{\partial\vec{r}}{\partial x_i}. \quad (\text{A.3.1})$$

Where  $a_i$  is the length of each vector. The metric tensor is defined as

$$g_{ij} = \frac{\partial\vec{r}}{\partial x_i} \cdot \frac{\partial\vec{r}}{\partial x_j}. \quad (\text{A.3.2})$$

In the orthogonal case  $g_{ij}$  is a matrix with  $a_i^2$  on the diagonal. An infinitesimal displacement along  $\vec{r}$  in three dimensions can be written as

$$d\vec{r} = \frac{\partial\vec{r}}{\partial x_1} dx_1 + \frac{\partial\vec{r}}{\partial x_2} dx_2 + \frac{\partial\vec{r}}{\partial x_3} dx_3, \quad (\text{A.3.3})$$

in terms of  $\vec{e}_i$  we get

$$d\vec{r} = a_1 dx_1 \vec{e}_1 + a_2 dx_2 \vec{e}_2 + a_3 dx_3 \vec{e}_3. \quad (\text{A.3.4})$$

We introduce a vector potential  $\psi(x_1, x_2, x_3, \dots)$ . An infinitesimal change in three dimensions in  $x_i$  gives the change of  $\psi$  as follows

$$d\psi = \frac{\partial\psi}{\partial x_1} dx_1 + \frac{\partial\psi}{\partial x_2} dx_2 + \frac{\partial\psi}{\partial x_3} dx_3. \quad (\text{A.3.5})$$

Comparing this result with Eq. (A.3.3), we observe that we can write

$$d\psi = \nabla\psi \cdot d\vec{r}, \quad (\text{A.3.6})$$

where

$$\nabla\psi = \frac{\vec{e}_1}{a_1} \frac{\partial\psi}{\partial x_1} + \frac{\vec{e}_2}{a_2} \frac{\partial\psi}{\partial x_2} + \frac{\vec{e}_3}{a_3} \frac{\partial\psi}{\partial x_3}, \quad (\text{A.3.7})$$

giving the  $\nabla$  operator

$$\nabla = \frac{\vec{e}_1}{a_1} \frac{\partial}{\partial x_1} + \frac{\vec{e}_2}{a_2} \frac{\partial}{\partial x_2} + \frac{\vec{e}_3}{a_3} \frac{\partial}{\partial x_3}. \quad (\text{A.3.8})$$

We have now developed a general expression for the gradient and del operator in three-dimension curvilinear coordinates. We also need the divergence in order to calculate the Laplace operator. Define a vector field

$$\vec{f} = f_1 \vec{e}_1 + f_2 \vec{e}_2 + f_3 \vec{e}_3, \quad (\text{A.3.9})$$

calculate its divergence

$$\nabla \cdot \vec{f} = \nabla \cdot (f_1 \vec{e}_1) + \nabla \cdot (f_2 \vec{e}_2) + \nabla \cdot (f_3 \vec{e}_3), \quad (\text{A.3.10})$$

where the first term is

$$\nabla \cdot (f_1 \vec{e}_1) = \frac{\partial f_1}{\partial x_1} + f_1 \left( \frac{\partial \vec{e}_1}{\partial x_1} \right) \cdot \vec{e}_1. \quad (\text{A.3.11})$$

The last term in this equation is problematic since we have no direct way of calculating it. We calculate the gradient of  $x_1$  by using the developed term for the del operator in Eq. (A.3.8)

$$\nabla x_1 = \frac{1}{a_1} \vec{e}_1, \quad (\text{A.3.12})$$

and similarly for the other two components. We also note that

$$\vec{e}_1 = \vec{e}_2 \times \vec{e}_3, \quad (\text{A.3.13})$$

which gives, using Eq. (A.3.12)

$$\vec{e}_1 = a_2 \nabla x_2 \times a_3 \nabla x_3. \quad (\text{A.3.14})$$

Again we write out the first term in Eq. (A.3.10), but now with the help of Eq. (A.3.14)

$$\nabla \cdot (f_1 \vec{e}_1) = \nabla(f_1 a_2 a_3) \cdot (\nabla x_2 \times \nabla x_3) + f_1 a_2 a_3 \nabla \cdot (\nabla x_2 \times \nabla x_3), \quad (\text{A.3.15})$$



writing out the last term, we see that

$$\nabla \cdot (\nabla x_2 \times \nabla x_3) = \nabla x_3 \cdot (\nabla \times \nabla x_2) - \nabla x_2 \cdot (\nabla \times \nabla x_3), \quad (\text{A.3.16})$$

is  $\vec{0}$ , since  $\nabla \times \nabla x_i = \vec{0}$ . Using Eq. (A.3.12) again we get

$$\nabla \cdot (f_1 \vec{e}_1) = \frac{1}{a_2 a_3} (\vec{e}_2 \times \vec{e}_3) \nabla (f_1 a_2 a_3), \quad (\text{A.3.17})$$

using Eq. (A.3.13) and Eq. (A.3.8) gives

$$\nabla \cdot (f_1 \vec{e}_1) = \frac{\vec{e}_1}{a_2 a_3} \left( \frac{\vec{e}_1}{a_1} \frac{\partial}{\partial x_1} (f_1 a_2 a_3) \right). \quad (\text{A.3.18})$$

This is of course cyclic in the coordinates and we can finally write out the divergence in Eq. (A.3.10) as

$$\nabla \cdot \vec{f} = \frac{1}{a_1 a_2 a_3} \left( \frac{\partial}{\partial x_1} (f_1 a_2 a_3) + \frac{\partial}{\partial x_2} (f_2 a_1 a_3) + \frac{\partial}{\partial x_3} (f_3 a_1 a_2) \right) \quad (\text{A.3.19})$$

We need a general expression for the Laplace operator. This is rather simple. We can set  $\vec{f} = \nabla$  in the equation above and get

$$\nabla^2 = \frac{1}{a_1 a_2 a_3} \left( \frac{\partial}{\partial x_1} \left( \frac{a_2 a_3}{a_1} \frac{\partial}{\partial x_1} \right) + \frac{\partial}{\partial x_2} \left( \frac{a_1 a_3}{a_2} \frac{\partial}{\partial x_2} \right) + \frac{\partial}{\partial x_3} \left( \frac{a_1 a_2}{a_3} \frac{\partial}{\partial x_3} \right) \right) \quad (\text{A.3.20})$$

A general volume element in three dimensions can be written as

$$dV = a_1 a_2 a_3 dx_1 dx_2 dx_3. \quad (\text{A.3.21})$$

Expressions for cylindrical polar coordinates can now be developed. First define

$$x = r \cos(\theta), \quad (\text{A.3.22})$$

$$y = r \sin(\theta), \quad (\text{A.3.23})$$

$$z = z, \quad (\text{A.3.24})$$

where  $r$  is the radial distance from the origin to the point  $P$ , while  $\theta$  is the anticlockwise angle from the x-axis up to  $P$ . The last coordinate  $z$  is the same as in the Cartesian case. Transforming the vector  $\vec{r}$  from Cartesian to polar coordinates results in the following  $\vec{r}$

$$\vec{r} = \begin{bmatrix} r \cos(\theta) \\ r \sin(\theta) \\ z \end{bmatrix}. \quad (\text{A.3.25})$$

We need to calculate the normalizations variables. Remember that

$$a_i = \left\| \frac{\partial \vec{r}}{\partial x_i} \right\|. \quad (\text{A.3.26})$$

This gives

$$a_r = 1, \quad (\text{A.3.27})$$

$$a_\theta = r, \quad (\text{A.3.28})$$

$$a_z = 1. \quad (\text{A.3.29})$$

We put these into Eq. (A.3.20) and get

$$\nabla^2 = \frac{1}{r} \left( \frac{\partial}{\partial r} \left( r \frac{\partial}{\partial r} \right) \right) + \frac{1}{r^2} \frac{\partial^2}{\partial \theta^2} + \frac{\partial^2}{\partial z^2}. \quad (\text{A.3.30})$$

Observe that we could write out the first term as a second and first derivate. In the two-dimensional case this would be

$$\nabla^2 = \frac{\partial^2}{\partial r^2} + \frac{1}{r} \frac{\partial}{\partial r} + \frac{1}{r^2} \frac{\partial^2}{\partial \theta^2}. \quad (\text{A.3.31})$$

The volume element from Eq. (A.3.21) becomes in two dimensional polar coordinates

$$dV = r dr d\theta, \quad (\text{A.3.32})$$

in two dimensional polar coordinates. In spherical polar coordinates we define

$$x = r \cos(\theta) \sin(\phi), \quad (\text{A.3.33})$$

$$y = r \sin(\theta) \sin(\phi), \quad (\text{A.3.34})$$

$$z = r \cos(\phi). \quad (\text{A.3.35})$$

When we now transform the vector  $\vec{r}$  from Cartesian to spherical polar coordinates we get

$$\vec{r} = \begin{bmatrix} r \cos(\theta) \sin(\phi) \\ r \sin(\theta) \sin(\phi) \\ r \cos(\phi) \end{bmatrix}. \quad (\text{A.3.36})$$

From Eq. (A.3.26) we see that

$$a_r = 1, \quad (\text{A.3.37})$$

$$a_\theta = r \sin(\phi), \quad (\text{A.3.38})$$

$$a_\phi = r. \quad (\text{A.3.39})$$

Plugging this into Eq. (A.3.20) gives the Laplace operator for the spherical polar case

$$\nabla^2 = \frac{1}{r^2} \frac{\partial}{\partial r} \left( r^2 \frac{\partial}{\partial r} \right) + \frac{1}{r^2 \sin^2(\theta)} \frac{\partial^2}{\partial \theta^2} + \frac{1}{r^2 \sin(\phi)} \frac{\partial}{\partial \phi} \left( \sin(\phi) \frac{\partial}{\partial \phi} \right), \quad (\text{A.3.40})$$

which can be written as

$$\nabla^2 = \frac{\partial^2}{\partial r^2} + \frac{2}{r} \frac{\partial}{\partial r} + \frac{1}{r^2 \sin^2(\theta)} \frac{\partial^2}{\partial \theta^2} + \frac{\cot(\phi)}{r^2} \frac{\partial}{\partial \phi} + \frac{1}{r^2} \frac{\partial^2}{\partial \phi^2}. \quad (\text{A.3.41})$$

From Eq. (A.3.21), the volume element in spherical polar coordinates can be written

$$dV = r^2 \sin(\phi) dr d\theta d\phi. \quad (\text{A.3.42})$$

In this thesis we have introduced the orbital momentum. We will now develop an expression for the z-component and the square of the angular momentum. We know that

$$\vec{L} = \vec{r} \times \vec{p}, \quad (\text{A.3.43})$$

written in components

$$L_x = yp_z - zp_y, \quad (\text{A.3.44})$$

$$L_y = zp_x - xp_z, \quad (\text{A.3.45})$$

$$L_z = xp_y - yp_x, \quad (\text{A.3.46})$$

$$L^2 = L_x^2 + L_y^2 + L_z^2. \quad (\text{A.3.47})$$

By transforming these expressions into polar coordinates, we can show that

$$L_z = -i\hbar \frac{\partial}{\partial \theta}, \quad (\text{A.3.48})$$

and

$$L^2 = -\hbar^2 \left( \frac{1}{\sin^2(\phi)} \frac{\partial^2}{\partial \theta^2} + \cot(\phi) \frac{\partial}{\partial \phi} + \frac{\partial^2}{\partial \phi^2} \right). \quad (\text{A.3.49})$$

## A.4 Transformation from center-of-mass to laboratory

In this section we will develop a transformation from the center-of-mass and relative basis to the laboratory basis in both two and three dimensions. We will call the center-of-mass and relative basis, the CM-rel basis for simplicity. The laboratory basis will be referred to as the lab basis. The harmonic oscillator basis is of interest to us, and it is this basis we are going to transform. In this section we will use Dirac notation due to its simplicity. See basic textbooks in quantum mechanics, for example [Shankar; 1994] for a mathematical introduction to the Dirac notation. The quantum number of the total angular momentum will now be referred to as  $L_T$ . This means that we can construct eigenfunctions of  $L_T^2$ ,  $L_{T_z}$  and  $H$  at the same time. This should not come as a surprise as we did this in Sec. 3.1. As an analogy to  $L_T$  we define  $M_T$  as the quantum number of the projection of the total orbital momentum. As elsewhere in this thesis we will label the center-of-mass quantum numbers and coordinates by capital letters, while we use low-key letters for the relative quantum numbers. The quantum numbers in the lab basis will be labeled by low-key letters, but with an index to separate the particles. The spins  $\vec{s}_1$  and  $\vec{s}_2$  are dropped during discussions since they work on the spin eigenvectors, which are invariant under this transformation. However, we should mention that the full eigenvector including spins are defined as  $|n_1 l_1, n_2 l_2, L_T M_T, S_T M_{S_T}\rangle$ , where  $S_T$  will be the total spin quantum number with projection  $M_{S_T}$ .

Using Dirac notation we define a state in the CM-rel basis as  $|nl, NL, L_T M_T\rangle$ .

Similarly a two-particle state is defined in the lab basis as  $|n_1 l_1, n_2 l_2, \tilde{L}_T \tilde{M}_T\rangle$ . The total orbital momenta is conserved along with its projection, thus  $\tilde{L}_T = L_T$  and  $\tilde{M}_T = M_T$ . We want to find a transformation between  $|nl, NL, L_T M_T\rangle$  and  $|n_1 l_1, n_2 l_2, L_T M_T\rangle$ . By using the completeness relation we can write the transformation as

$$|n_1 l_1, n_2 l_2, L_T M_T\rangle = \sum_{nlNL} |nl, NL, L_T M_T\rangle \langle nl, NL, L_T M_T | n_1 l_1, n_2 l_2, L_T M_T\rangle. \quad (\text{A.4.1})$$

From [Talmi; 1952] we know that the coefficients in Eq. (A.4.1) is independent of  $M_T$ . Hence it is dropped from the coefficient in further calculation. When doing the transformation, the energy needs to be conserved. Comparing the solutions of Eq. (3.2.26) and the three dimensional counterpart of Eq. (3.1.3) we get the relation

$$2n_1 + l_1 + 2n_2 + l_2 = 2n + l + 2N + L. \quad (\text{A.4.2})$$

This makes the sum in Eq. (A.4.1) finite due to the restriction posed by Eq. (A.4.2) and nonzero by the triangle inequality

$$|l_1 - l_2| \leq L_T \leq l_1 + l_2, \quad (\text{A.4.3})$$

and

$$m_1 + m_2 = M_T. \quad (\text{A.4.4})$$

The two last equations are properties of the Clebsh-Gordon coefficients, see [Shankar; 1994] for details. As we are investigating the Coulomb interaction we will now observe what will happen with the matrix elements during the transformation. Instead of illustrating this using the Coulomb interaction, we use the general interaction  $V(r)$ . Using Eq. (A.4.1) and the completeness relation the matrix elements of this interaction could be written as

$$\begin{aligned} \langle n_1 l_1, n_2 l_2, L_T M_T | V(r) | n'_1 l'_1, n'_2 l'_2, L'_T M'_T \rangle = \\ \sum_{nlNL} \sum_{n'l'N'L'} \langle n_1 l_1, n_2 l_2, L_T | nl, NL, L_T \rangle \times \\ \langle n'_1 l'_1, n'_2 l'_2, L'_T | n'l', N'L', L'_T \rangle \times \\ \langle nl, NL, L_T M_T | V(r) | n'l', N'L', L'_T M'_T \rangle. \end{aligned} \quad (\text{A.4.5})$$

The interaction depends only on the relative coordinates and last coefficient in Eq. (A.4.5) simplifies to

$$\begin{aligned} \langle nl, NL, L_T M_T | V(r) | n'l', N'L', L'_T M'_T \rangle = \\ \langle nl | V(r) | n'l' \rangle \delta_{NN'} \delta_{ll'} \delta_{LL'} \delta_{L_T L'_T} \delta_{M_T M'_T}. \end{aligned} \quad (\text{A.4.6})$$

This coefficient could be evaluated explicitly using the series expansion over the Talmi integrals [Talmi; 1952], see Sec. 4.1 for details. Substituting Eq. (A.4.6) into Eq. (A.4.5)

gives

$$\begin{aligned} \langle n_1 l_1, n_2 l_2, L_T M_T | V(r) | n'_1 l'_1, n'_2 l'_2, L_T M_T \rangle = \\ \sum_{nlNL} \langle nl, NL, L_T | n_1 l_1, n_2 l_2, L_T \rangle \\ \langle n' l', NL, L_T | n'_1 l'_1, n'_2 l'_2, L_T \rangle \langle nl | V(r) | n' l' \rangle. \end{aligned} \quad (\text{A.4.7})$$

If we now could find an expression for the two unknown coefficients in the sum we could calculate both the transformations and the integral explicitly using Talmi integrals. However, for reasons explained in Sec. 4.1 we will not be using a series expansion of the interacting part. But the transformation is of great importance to us. These transformation coefficients have already been worked out and is called Moshinsky transformation coefficients [Moshinsky; 1969]. Basically we have the two recurrence relations

$$\begin{aligned} \langle nl, NL, L_T M_T | (n_1 + 1) l_1, n_2 l_2, L_T M_T \rangle = - \\ \sqrt{\frac{1}{(n_1 + 1)(n_1 + l_1 + 3/2)}} \times \\ \sum_{\tilde{n} \tilde{l} \tilde{N} \tilde{L}} \langle nl, NL, L_T M_T | \rho_1^2 | \tilde{n} \tilde{l}, \tilde{N} \tilde{L}, L_T M_T \rangle \times \\ \langle \tilde{n} \tilde{l}, \tilde{N} \tilde{L}, L_T | n_1 l_1, n_2 l_2, L_T \rangle, \end{aligned} \quad (\text{A.4.8})$$

and

$$\begin{aligned} \langle nl, NL, L_T M_T | n_1 l_1, (n_2 + 1) l_2, L_T M_T \rangle = - \\ \sqrt{\frac{1}{(n_2 + 1)(n_2 + l_2 + 3/2)}} \times \\ \sum_{\tilde{n} \tilde{l} \tilde{N} \tilde{L}} \langle nl, NL, L_T M_T | \rho_2^2 | \tilde{n} \tilde{l}, \tilde{N} \tilde{L}, L_T M_T \rangle \times \\ \langle \tilde{n} \tilde{l}, \tilde{N} \tilde{L}, L_T | n_1 l_1, n_2 l_2, L_T \rangle, \end{aligned} \quad (\text{A.4.9})$$

where  $\rho_1$  and  $\rho_2$  is the dimensionless radial coordinates in the lab basis for particle one and two respectively. The definition  $\rho^2 = \beta r^2$  and the definition of  $\beta$  can be obtained from App. A.7.2.

If we now had a way to calculate the matrix elements in Eq. (A.4.9) we could determine all transformation brackets in Eq. (A.4.1) and hence have a proper transformation which is easily implemented on a computer. The matrix elements can be calculated in several ways and is not shown explicitly in this section as it is done elsewhere. See for example Sec. 4.1 where the analogy should be clear. To be able to calculate the elements one needs to transform  $\rho_1$  and  $\rho_2$  into an  $r$  and  $R$  dependent expression. Using Eq. (3.2.3) and (3.2.4) we can express  $\rho_1$  and  $\rho_2$  in relative and center-of-mass coordinates so they coincide with the quantum numbers of the eigenvectors. Recursion relation need to start somewhere and in our case it would be natural to start at  $\langle nl, NL, L_T | 0 l_1, 0 l_2, L_T \rangle$ . Up until now we have no clue how  $l$  and  $L$  transforms. Thus we need to develop an explicit expression for this bracket. This notation also suits us well, as we diagonalize for each  $l$  and  $L$ . The derivation is not given in this

thesis as it is complicated and cumbersome. See for example [Moshinsky; 1969] for an overview and [Brody and Moshinsky; 1967] for a more simplified expression. The  $\langle nl, NL, L_T | 0l_1, 0l_2, L_T \rangle$  coefficient can be written as

$$\begin{aligned} \langle nl, NL, L_T | 0l_1, 0l_2, L_T \rangle = & \\ & (-1)^{n+l+L-L_T} \sqrt{\frac{l_1! l_2! (2l+1)(2L+1)}{(2l_1)! (2l_2)! 2^{l+L}}} \times \\ & \sqrt{\frac{(n+l)! (N+L)!}{n! N! (2n+2l+1)! (2N+2L+1)!}} \times \\ & \sum_x (2x+1) A(l_1 l, l_2 L, x) W(l L l_1 l_2; L_T x), \end{aligned} \quad (\text{A.4.10})$$

where

$$\begin{aligned} A(l_1 l, l_2 L, x) = & B(l_1, l, x) B(l_2, L, x) \times \\ & \sum_q \left\{ (-1)^{(l+q-l_1)/2} \frac{(l+q-l_1)!}{((l+q-l_1)/2)! ((l+l_1-q)/2)!} \times \right. \\ & \left. \frac{(L+q-l_2)!}{(q-x)! (q+x+1)! ((L+q-l_2)/2)! ((L+l_2-q)/2)!} \right\}, \end{aligned} \quad (\text{A.4.11})$$

and

$$B(a, b, x) = \sqrt{\frac{(a+b+x+1)! (a+b-x)! (a+x-b)!}{(b+x-a)!}}. \quad (\text{A.4.12})$$

The  $W$  in Eq. (A.4.10) is the Racah  $W$ -coefficient [Edmonds; 1957] which relates to the Clebsch-Gordon coefficients. The summation of these coefficients are reduced from  $9j$  to  $6j$ , hence the variable  $x$ . See [Jahn and Hope; 1954] and [Edmonds; 1957] for details regarding the  $9j$  and  $6j$  coefficients. Proper references are given therein. The restrictions on  $x$  are

$$|l - l_1| \leq x \leq l + l_1, \quad (\text{A.4.13})$$

and

$$|L - l_2| \leq x \leq L + l_2. \quad (\text{A.4.14})$$

The summation over  $q$  is restricted to those non-negative integer values of  $q$  for which  $l+q-l_1$  is even and the arguments of the factorials are non-negative integers. Calculation of the  $\langle nl, NL, L_T | n_1 l_1, n_2 l_2, L_T \rangle$  in Eq. (A.4.7) can now be done using first Eq. (A.4.10) and Eq. (A.4.9) if needed.

## A.5 Time-independent perturbation theory

Time-independent perturbation theory has a wide range of applications and its basics will be covered in this section. The whole idea of perturbation theory is to separate a problem in two parts. The first part is known and can be calculated, while the second is unknown and small compared to the first. The Hamiltonian of our system can then

be separated in two parts as

$$H = H_0 + \lambda H_1, \quad (\text{A.5.1})$$

where  $H_0$  has a known solution,  $H_1$  has not. The constant  $\lambda$  is the strength of the perturbation. Often  $H_1$  is referred to as the correction term or as a the perturbation. We define, in Dirac notation

$$H_0|n^0\rangle = E_n^0|n^0\rangle, \quad (\text{A.5.2})$$

where  $|n^0\rangle$  is the normalized eigenvector and  $E_0$  is the eigenvalue of  $H_0$ . In this thesis we will only meet non-degenerate eigenvalues. Hence, degenerate perturbation theory is not covered. Assume that we can expand the eigenvectors and eigenvalues in the parameter  $\lambda$

$$|n\rangle = |n^0\rangle + \lambda|n^1\rangle + \lambda^2|n^2\rangle + \dots, \quad (\text{A.5.3})$$

$$E_n = E_n^0 + \lambda E_n^1 + \lambda^2 E_n^2 + \dots \quad (\text{A.5.4})$$

The exact eigensolutions are given as

$$H|n\rangle = E_n|n\rangle. \quad (\text{A.5.5})$$

Substituting Eq. (A.5.2) into this equation yields

$$(H_0 + \lambda H_1)|n\rangle = E_n|n\rangle. \quad (\text{A.5.6})$$

Expanding and moving eigenvalues from right to left gives

$$(H_0 + \lambda H_1 - E_n^0 - \lambda E_n^1 - \lambda^2 E_n^2 - \dots)(|n^0\rangle + \lambda|n^1\rangle + \lambda^2|n^2\rangle + \dots) = 0. \quad (\text{A.5.7})$$

This equation should be valid for all  $\lambda$  thus giving rise to equations of different orders. The first few are given in Table A.1 If we multiply the equation corresponding to  $\lambda = 1$

Order, $\lambda$	Equation
0	$(H_0 - E_n^0) n^0\rangle = 0$
1	$(H_0 - E_n^0) n^1\rangle + (H_1 - E_n^1) n^0\rangle = 0$
2	$(H_0 - E_n^0) n^2\rangle + (H_1 - E_n^1) n^1\rangle + E_n^2 n^0\rangle = 0$

**Table A.1:** Lowest order perturbation equations.

with  $\langle n^0|$  from the left and make use of  $\langle n^0|n^0\rangle = 1$  we get

$$\langle n^0|H_0 - E_n^0|n^1\rangle + \langle n^0|H_1|n^0\rangle - E_n^1 = 0, \quad (\text{A.5.8})$$

where we can write

$$\langle n^0|H_0 - E_n^0|n^1\rangle = \langle n^1|H_0 - E_n^0|n^0\rangle^\dagger, \quad (\text{A.5.9})$$

which is zero from Table A.1. We now have an expression for the first order eigenvalue correction given as

$$E_n^1 = \langle n^0|H_1|n^0\rangle. \quad (\text{A.5.10})$$

To find the first order eigenvector correction we multiply the first order equation with  $\langle n'|$ ,  $n' \neq n$  from the left and make use of  $\langle i|j\rangle = \delta_{ij}$ . We then get

$$\langle n'|H_0 - E_n^0|n^1\rangle + \langle n'|H_1|n^0\rangle. \quad (\text{A.5.11})$$

Taking the complex conjugate of the first term

$$\langle n'|H_0 - E_n^0|n^1\rangle = \langle n^1|H_0 - E_n^0|n'\rangle^\dagger, \quad (\text{A.5.12})$$

and using  $H_0|n'\rangle = E_{n'}^0|n'\rangle$ , we obtain

$$\langle n'|H_0 - E_n^0|n^1\rangle = (E_{n'}^0 - E_n^0)\langle n'|n^1\rangle. \quad (\text{A.5.13})$$

Solving this equation and using the completeness relation to expand the eigenvector gives

$$|n^1\rangle = \sum_{n' \neq n} \frac{\langle n'|H_1|n^0\rangle}{E_n^0 - E_{n'}^0} |n'\rangle. \quad (\text{A.5.14})$$

In many situations the second order term is also needed. We can obtain the expression for  $E_n^2$  by multiplying the second order equation in Table A.1 with  $\langle n^0|$  from the left. This gives rise to

$$\langle n^0|H_0 - E_n^0|n^2\rangle + \langle n^0|H_1 - E_n^1|n^1\rangle - E_n^2 = 0. \quad (\text{A.5.15})$$

Solving for  $E_n^2$  yields

$$E_n^2 = \langle n^0|H_1|n^1\rangle. \quad (\text{A.5.16})$$

By substituting Eq. (A.5.14) into the equation above we finally get

$$E_n^2 = \sum_{n' \neq n} \frac{|\langle n'|H_1|n^0\rangle|^2}{E_n^0 - E_{n'}^0}. \quad (\text{A.5.17})$$

We will not be using the eigenvector perturbations explicitly nor any higher order eigenvalue perturbations. Thus we will not develop an expression for the second order eigenvector perturbation. Writing out the eigenvalue to second order from Eq. (A.5.4) gives

$$E_n = E_n^0 + \langle n^0|H_1|n^0\rangle + \sum_{n' \neq n} \frac{|\langle n'|H_1|n^0\rangle|^2}{E_n^0 - E_{n'}^0} + O(\lambda^3). \quad (\text{A.5.18})$$

The perturbation theory we just considered is called Rayleigh-Schrödinger perturbation theory [Gross and Runge; 1991]. For the perturbation theory to be valid, the series in Eq. (A.5.14) need to converge. We then require

$$\left| \frac{\langle n'|H_1|n^0\rangle}{E_n^0 - E_{n'}^0} \right| \ll 1. \quad (\text{A.5.19})$$



## A.6 Numerical Integration

In this section we will discuss different numerical integrations techniques and at the end decide which of these are the best suited for our application. Basically we want to calculate

$$I = \int_i^e f(x)dx. \quad (\text{A.6.1})$$

The integral starts at  $x = i$  and ends at  $x = e$ . We will first discuss equal step techniques and then move on to a more complicated integration scheme called Gaussian quadrature. In the end of this section we will do a numerical analysis of the techniques.

### A.6.1 Equal step techniques

The simplest approximation is to divide the area into a given number of smaller areas as shown in Fig. A.6.1. We can then partition Eq. (A.6.1) as

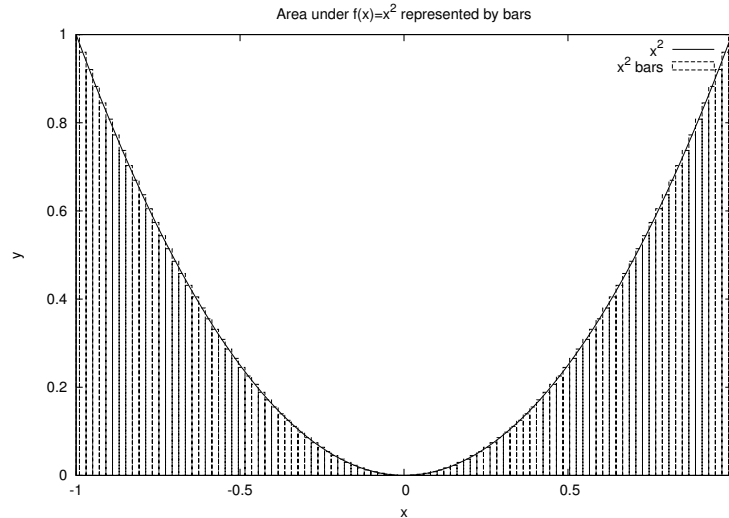


**Figure A.6.1:** Area of  $f(x) = x^2$  represented by bars

$$\int_i^e f(x)dx = \int_i^{i+h} f(x)dx + \int_{i+h}^{i+2h} f(x)dx + \dots + \int_{e-h}^e f(x)dx, \quad (\text{A.6.2})$$

where  $h$  is the step length, the width of each area. By approximating  $f(x)$  as a linear function between  $i$  and  $i+h$  we get trapezoids instead of rectangular areas. Hence this integration technique is often referred to as the trapezoidal rule. The average height between the two endpoints in the sub-interval is  $(f(i) + f(i+h))/2$ . To get the area, we need to multiply the height by the width, which is  $h$ . Doing this yields

$$\int_i^{i+h} f(x)dx \approx \frac{h}{2}(f_i + f_{i+1}), \quad (\text{A.6.3})$$

where  $f_i$  and  $f_{i+1}$  are evaluated at the points  $x = i$  and  $x = i + h$  respectively. On the interval  $[i, e]$  the integral approximation becomes

$$\int_i^e f(x)dx = h \left( \frac{f(i)}{2} + f(i+h) + f(i+2h) + \dots + f(e-h) + \frac{f(e)}{2} \right). \quad (\text{A.6.4})$$

Only the endpoints keep their pre-factor of  $1/2$  since the internal points are counted twice. From a more general viewpoint we could write Eq. (A.6.1) as

$$\int_i^e f(x)dx = \sum_{i=1}^N f_i w_i. \quad (\text{A.6.5})$$

Comparing this to Eq. (A.6.3) we have  $N = 2$  and  $w_1 = w_2 = h/2$ . Other approximations than the trapezoidal rule can be found if we represent  $f(x)$  by a higher degree polynomial between the points. In Table A.2 we have listed the most common numerical integration techniques using equal step length  $h$ .

	$N$	$w_i$
Trapezoid	2	$(h/2, h/2)$
Simpson's	3	$(h/3, 4h/3, h/3)$
Simpson's 3/8	4	$(3h/8, 9h/8, 9h/8, 3h/8)$
Bodes	5	$(14h/45, 64h/45, 24h/45, 64h/45, 14h/45)$

**Table A.2:** Equal step numerical integration techniques.

Later we are going to investigate the numerical error in these methods, but first we need to determine the analytical error. To find this we use a Taylor expansion [Riley et al.; 2003] around a point  $x = a$  given as

$$f_{a+b} = f_a + b \frac{df_a}{dx} + \frac{b^2}{2} \frac{d^2 f_a}{dx^2} + \frac{b^3}{8} \frac{d^3 f_a}{dx^3} + O(h^4). \quad (\text{A.6.6})$$

Let  $a = i + 1/2$  and  $b = \pm 1/2$  to get the Taylor expansion around the half-width of  $h$  for one sub-interval as

$$f_{i+1/2, \pm 1/2} = f_{i+1/2} \pm \frac{1}{2} \frac{df_{i+1/2}}{dx} + \frac{1}{8} \frac{d^2 f_{i+1/2}}{dx^2} \pm \frac{1}{48} \frac{d^3 f_{i+1/2}}{dx^3} + O(h^4). \quad (\text{A.6.7})$$

Combining this with Eq. (A.6.3) yields

$$\int_i^{i+1} f(x)dx \approx h \left( f_{i+1/2} + \frac{h^2}{8} \frac{d^2 f_{i+1/2}}{dx^2} + O(h^4) \right). \quad (\text{A.6.8})$$

To be able to separate the error we need an exact expression for the integration within one sub-interval. For comparison reasons we choose to evaluate this integral around  $x = i + h/2$ . This gives, after a variable change

$$\int_i^{i+1} f(x)dx = \int_{-h/2}^{h/2} f(x_{i+1/2} + t)dt. \quad (\text{A.6.9})$$

Taylor expansion is again used on  $f(x_{i+1/2} + t)$  to give

$$\int_{-h/2}^{h/2} f(x_{i+1/2} + t) dt = \int_{-h/2}^{h/2} \sum_{n=0}^{\infty} f_{i+1/2}^{(n)} \frac{t^n}{n!} dt, \quad (\text{A.6.10})$$

where  $f^{(n)}$  is the  $n$ 'th derivative of  $f$ . The change in notation should be obvious from earlier derivations. Evaluating the integral gives us an exact expression for the integrals as follows

$$\int_{-h/2}^{h/2} f(x_{i+1/2} + t) dx = \sum_{\substack{n=0 \\ \text{even}}}^{\infty} f_{i+1/2}^{(n)} \frac{2}{(n+1)!} \left(\frac{h}{2}\right)^{n+1}. \quad (\text{A.6.11})$$

Subtract Eq. (A.6.8) from this, results in the analytical local error

$$E_l = \frac{h^3}{12} \frac{d^2 f_{i+1/2}}{dx^2} + O(h^5). \quad (\text{A.6.12})$$

If we take  $N$  as the number of sub-intervals we can write

$$h = \frac{e - i}{N}. \quad (\text{A.6.13})$$

The local error will be added  $N$  times. The global error will be the total analytical error on the interval  $[i, e]$ . This can now be approximated as

$$E_g \approx \frac{(e - i)^3}{12N^2} \frac{d^2 f_{i+1/2}}{dx^2}. \quad (\text{A.6.14})$$

Similar expressions can be found for the other integration techniques by using the same procedures. The trapezoidal rule gives exact solutions for a linear  $f(x)$  on the sub-interval just as the Simpson's rule gives us exact solutions for a parabolic  $f(x)$ . On the global scale we can at best hope for an exact solution of an  $N - 1$  degree polynomial by using  $N$  points. In this thesis we are going to integrate polynomials with much higher orders than one and two. It is possible to improve the accuracy by using Gaussian quadrature integration, which we will now briefly explain.

### A.6.2 Gaussian quadrature techniques

We will often see that Gaussian quadrature offers a faster and more accurate integration scheme than the equal step techniques. The choice of method depends on the behavior of  $f(x)$ . As before we can write the integral as

$$\int_i^e f(x) dx = \sum_{i=1}^N f_i w_i. \quad (\text{A.6.15})$$

Let us now be more open minded than previous. By not fixing the integration points and weights we have greater flexibility to choose the variables. Actually the approximation error vanishes if  $f(x)$  is a  $2N - 1$  degree polynomial and we are cautious with the

choice of weights  $\omega_i$ . This is due to the fact that  $N$  different mesh points and weights gives rise to  $2N$  degrees of freedom. It is important that  $f(x)$  is smooth, or can be made smooth by factoring out  $g(x)$  from  $f(x)$  as  $f(x) = g(x)F(x)$ . Singularities or unwanted behavior is included in  $g(x)$ , thus making  $F(x)$  more smooth. In Table A.3 we have listed the most used Gaussian quadrature integration techniques. We will not

	Integral	$g(x)$
Gauss-Legendre	$\int_a^b f(x)dx$	1
Gauss-Chebyshev	$\int_{-1}^1 \frac{1}{\sqrt{1-x^2}} F(x)dx$	$\frac{1}{\sqrt{1-x^2}}$
Gauss-Hermite	$\int_{-\infty}^{\infty} e^{-x^2} F(x)dx$	$e^{-x^2}$
Gauss-Laguerre	$\int_0^{\infty} x^\alpha e^{-x} F(x)dx$	$x^\alpha e^{-x}$
Gauss-Jacobi	$\int_{-1}^1 (1-x)^\alpha (1+x)^\beta F(x)dx$	$(1-x)^\alpha (1+x)^\beta$

**Table A.3:** Overview of Gaussian quadrature integration techniques.  $\alpha$  and  $\beta$  are constants.

go into the procedures of calculating the integration points and weights. For details see [Press et al.; 2002]. Immediately we recognize the Laguerre behavior we obtained by solving the harmonic oscillator problem in the Gauss-Laguerre integration method. In the next section we will compare trapezoidal, Gauss-Laguerre and Gauss-Legendre integration methods and decide which are most suited to our situation.

### A.6.3 Numerical analysis of the numerical integration techniques

The discussion in the last section yielded different integrations techniques. In this section we will create a test case and compare the trapezoidal, Gauss-Laguerre and Gauss-Legendre techniques. At the end we will hopefully come to a conclusion of the preferred method. In this thesis  $F(x)$  from Table A.3 is the Laguerre polynomials. To be able to compare results, we also need the analytical solution. For simplicity we chose to integrate

$$\int_0^{\infty} x^\alpha e^{-x^2} (1 - x^2 + x^4 + \dots + (-1)^p x^{2p}) dx, \quad (\text{A.6.16})$$

as this reflects our Laguerre solutions coming from the Coulomb interaction, see Sec. 4.1.1 for details. From definite integral tables, for example [Abramowitz and Stegun; 1972], we know that

$$\int_0^{\infty} x^\alpha e^{-\beta x^2} dx = \frac{1}{2} \beta^{-(\alpha+1)/2} \Gamma\left(\frac{\alpha+1}{2}\right), \quad (\text{A.6.17})$$

where  $\Gamma$  is the Gamma function [Abramowitz and Stegun; 1972]. Using this, Eq. (A.6.16) have the analytical solution

$$\begin{aligned} \int_0^\infty x^\alpha e^{-x^2} (1 - x^2 + x^4) dx = \\ \frac{1}{2} \left[ \Gamma\left(\frac{\alpha+1}{2}\right) - \Gamma\left(\frac{\alpha+3}{2}\right) + \Gamma\left(\frac{\alpha+5}{2}\right) \right. \\ \left. + \dots (-1)^p \Gamma\left(\frac{\alpha+2p+1}{2}\right) \right]. \end{aligned} \quad (\text{A.6.18})$$

In Fig. A.6.2 we have compared the relative error defined as

$$|\epsilon| = \left| \frac{\text{analytic integration} - \text{numerical integration}}{\text{analytic integration}} \right|, \quad (\text{A.6.19})$$

of the four integration techniques. The analytic solutions can be found in Eq. (A.6.18). Each figure represents a given order of integration polynomial  $p$ . In all figures we have used  $\alpha = 3.0$ . For the Gauss-Legendre scheme the low integration limit  $a = 0.0$  and the high integration limit  $b$  are used for each  $p$ . The  $b$  values for the Gauss-Legendre scheme are listed for each figure. To illustrate that it is important to adjust  $b$  accordingly is illustrated in Fig. A.6.3 for the case of  $p = 50$ . For the trapezoidal scheme,  $a = 0$  and  $b = 20$  are used. They differ from the Gauss-Legendre scheme due to the substitution  $x = r^2$ . We clearly see that the Gauss-Laguerre method is the most stable, especially for very low  $n$ . As  $p$  increases the equal width methods needs more integration points to keep up with the Gauss-Laguerre technique. This should not come as a surprise, since the complexity of the integral increases with  $p$ . However, as  $p = 100$ , the Gauss-Legendre method gets more accurate than the Gauss-Laguerre. But in Sec. 4.1 we showed that a quantum number cutoff at  $n_{max} \approx 80$  was more than sufficient to obtain convergent eigenvalues. The interacting term would then yield an integral over a polynomial with largest degree  $\propto r^{320}$ . To simplify the calculations we substitute  $x = r^2$ , so the largest term in the polynomial becomes  $\propto x^{160}$ . The same situation is obtained by letting  $p \approx 80$  and we can then conclude that Gauss-Laguerre is the method of choice. Gauss-Laguerre methods are also more computer efficient to calculate. In this thesis we have strictly used Gauss-Laguerre due to its simplicity and effectiveness.

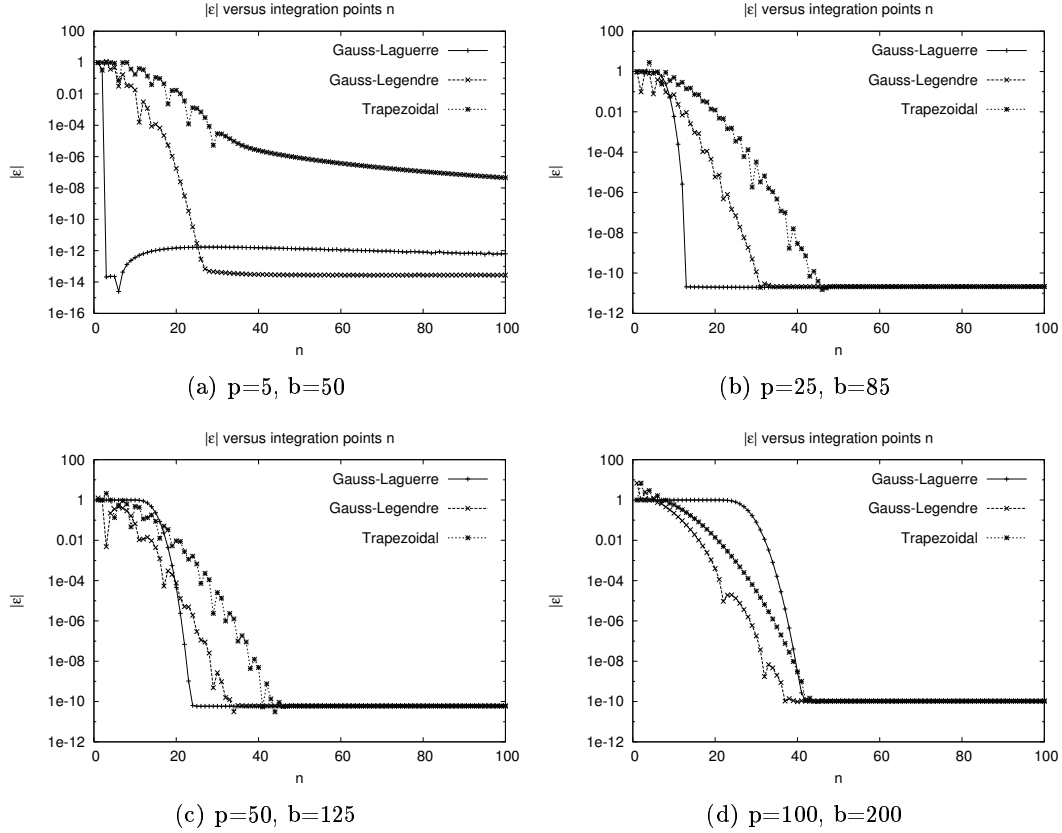


**Figure A.6.2:** The error  $|\epsilon|$  as a function of numerical integration points  $n$ . The upper integration limit  $b$  is also listed for each  $p$ . The importance of this can be seen from Fig. A.6.3. We clearly see the advantage of the Gauss-Laguerre method. The difference between Gauss-Laguerre and Gauss-Legendre for  $p = 5$  is due to numerical limitations and they have essentially the same accuracy as soon as they have converged. A numerical error of about  $10^{-10}$  is in most cases more than enough. Also note the low accuracy for the trapezoidal method at  $p = 5$ .

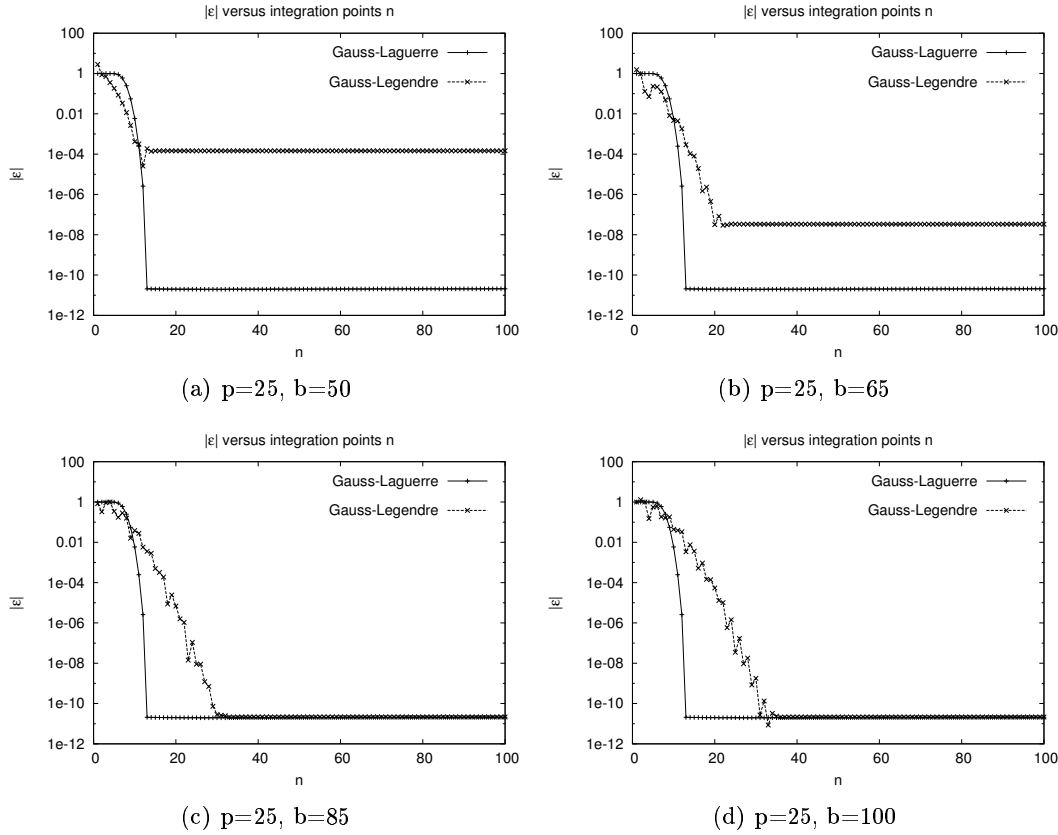


**Figure A.6.3:** The error  $|\epsilon|$  as a function of numerical integration points  $n$ . Here we illustrate the importance of the choice of integration points for  $p = 25$ . As we increase the integration points, the accuracy increases. This should not come as a surprise as a termination of the eigenvector before it is completely damped excludes contributions to the integral. At the same time, we do not want the limit to be artificially high, due to computer work. Hence, setting the limit to  $b = 85$  for  $p = 25$  ensures optimal balance between accuracy and computer work.

## A.7 Solution of the radial equation

The first section calculates the radial eigensolutions for a two dimensional harmonic oscillator in a magnetic field along the third axis. In section two, the three dimensional counterpart is worked out

### A.7.1 Two dimension

We will now solve the Schrödinger equation given as

$$-\frac{\hbar^2}{2m^*} \left( \frac{\partial^2}{\partial r^2} + \frac{1}{r} \frac{\partial}{\partial r} - \frac{m^2}{r^2} - \frac{emB}{\hbar c} \right) \psi(r) + \frac{1}{2} m^* \omega^2 r^2 \psi(r) = E \psi(r). \quad (\text{A.7.1})$$

Define

$$\epsilon = \frac{2m^* E}{\hbar^2} - \frac{emB}{\hbar c}, \quad (\text{A.7.2})$$

and substitute

$$x = r^2, \quad (\text{A.7.3})$$

into Eq. (A.7.1) to get

$$-\left( 4x \frac{\partial^2}{\partial x^2} + 4 \frac{\partial}{\partial x} - \frac{m^2}{x} \right) \psi'(x) + \frac{m^{*2} \omega^2}{\hbar^2} x \psi'(x) = \epsilon \psi'(x). \quad (\text{A.7.4})$$

To get rid of the first derivative we can do the substitution  $\psi'(x) = x^{-1/2} u(x)$ . After a bit of algebra we get the equation

$$-\frac{\partial^2 u(x)}{\partial x^2} + \frac{1}{4} \left( \frac{m^{*2} \omega^2}{\hbar^2} - \frac{\epsilon}{x} - \frac{(1-m^2)}{x^2} \right) u(x) = 0. \quad (\text{A.7.5})$$

To make the equation dimensionless, substitute  $y = m^* \omega x / \hbar = \beta x$ . This gives

$$-\frac{\partial^2 u'(y)}{\partial y^2} + \frac{1}{4} \left( 1 - \frac{\epsilon}{\beta y} - \frac{(1-m^2)}{y^2} \right) u'(y) = 0. \quad (\text{A.7.6})$$

We now have a much simpler equation compared to what we started out with. However, we still need to make some general considerations at the limits to simplify the equation even more. Let us consider what is going on if we let  $y \rightarrow \infty$ . When this happens we get a very simple equation

$$\frac{\partial^2 u'(y)}{\partial y^2} \simeq \frac{1}{4} u'(y), \quad (\text{A.7.7})$$

which has an approximate solution which goes as  $u'(y) \simeq e^{\pm y/2}$ . But we need the solution to be finite, even at  $y \rightarrow \infty$ . Then, only the solution for the negative  $y$  is allowed. That is

$$u'(y) \simeq e^{-y/2}. \quad (\text{A.7.8})$$



Now, let us consider  $y \rightarrow 0$ . In this regime we get a equation

$$\frac{\partial^2 u'(y)}{\partial y^2} \simeq \frac{m^2 - 1}{4y^2} u'(y). \quad (\text{A.7.9})$$

This equation has two solution

$$u'(y) \simeq y^{(m+1)/2}, \quad (\text{A.7.10})$$

$$u'(y) \simeq y^{-(m-1)/2}. \quad (\text{A.7.11})$$

This should be finite at  $y = 0$ . If  $m > 0$  we see that the only valid solution is the first. Combining Eq. (A.7.8) and Eq. (A.7.10) we can now substitute

$$u'(y) = y^{(m+1)/2} e^{-y/2} \rho(y), \quad (\text{A.7.12})$$

into Eq. (A.7.6) and get, again after tedious algebra

$$y \frac{\partial^2 p(y)}{\partial y^2} + (m+1-y) \frac{\partial p(y)}{\partial y} + \frac{1}{2} \left( \frac{\epsilon}{2\beta} - m - 1 \right) p(y) = 0. \quad (\text{A.7.13})$$

Defining

$$\lambda = \frac{1}{2} \left( \frac{\epsilon}{2\beta} - m - 1 \right), \quad (\text{A.7.14})$$

and substituting this into the previous differential equation yields

$$y \frac{\partial^2 p(y)}{\partial y^2} + (m+1-y) \frac{\partial p(y)}{\partial y} + \lambda p(y) = 0. \quad (\text{A.7.15})$$

We have now arrived at a differential equation known as the associated Laguerre differential equation. Its solutions can be found by series expansion. Let us do this for illustrative purpose. The quantum number  $n$  will arise during termination of the series and hence it is important. From Eq. (A.7.15) we see that there is a singular point at  $y = 0$  and an irregular singularity at  $y = \infty$ . From Fuch's theorem [Arfken and Weber; 1995], we know that there exist a solution by using the Frobenius series

$$p(y) = \sum_{n=0}^{\infty} a_n y^{n+\sigma}, \quad (\text{A.7.16})$$

where  $\sigma$  is any number and  $a_n$  are constants to be determined. Now, derivate  $p(y)$  twice to get

$$\frac{\partial p(y)}{\partial y} = \sum_{n=0}^{\infty} (n+\sigma) a_n y^{n+\sigma-1}, \quad (\text{A.7.17})$$

$$\frac{\partial^2 p(y)}{\partial y^2} = \sum_{n=0}^{\infty} (n+\sigma)(n+\sigma-1) a_n y^{n+\sigma-2}. \quad (\text{A.7.18})$$

We now demand that  $a_0 \neq 0$  since if this was not the case, we could redefine  $\sigma$  to make  $a_0 \neq 0$ . Putting equation Eqs. (A.7.16), (A.7.17) and (A.7.18) into Eq. (A.7.15) we

get

$$y \sum_{n=0}^{\infty} (n+\sigma)(n+\sigma-1)a_n y^{n+\sigma-2} + (m+1) \sum_{n=0}^{\infty} (n+\sigma)a_n y^{n+\sigma-1} - y \sum_{n=0}^{\infty} (n+\sigma)a_n y^{n+\sigma-1} + \lambda \sum_{n=0}^{\infty} a_n y^{n+\sigma} = 0, \quad (\text{A.7.19})$$

dividing by  $y^{\sigma-1}$  yields

$$\sum_{n=0}^{\infty} (n+\sigma)(n+\sigma-1)a_n y^n + (m+1) \sum_{n=0}^{\infty} (n+\sigma)a_n y^n - \sum_{n=0}^{\infty} (n+\sigma)a_n y^{n+1} + \lambda \sum_{n=0}^{\infty} a_n y^{n+1} = 0, \quad (\text{A.7.20})$$

sort terms so that

$$\sum_{n=0}^{\infty} [(n+\sigma)(n+\sigma-1) + (m+1)(n+\sigma) + y(\lambda - n - \sigma)] a_n y^n = 0. \quad (\text{A.7.21})$$

This equation should be valid for all  $y$ . Setting  $y = 0$  we see that all terms with  $n > 0$  vanish. Remember that we demanded that  $a_0 \neq 0$ . We can then remove the remaining  $a_0$  giving rise to the indicial equation

$$\sigma(\sigma + m) = 0 \quad (\text{A.7.22})$$

The solutions to this equation are  $\sigma = 0$  or  $\sigma = -m$ , where  $m$  is an integer. We cannot accept a solution with  $\sigma = -m$  around  $y = 0$ , since the eigenvectors will diverge. We then consider the remaining option. Putting  $\sigma = 0$  back into equation Eq. (A.7.20) gives

$$\sum_{n=0}^{\infty} n(n-1)a_n y^n + (m+1) \sum_{n=0}^{\infty} n a_n y^n - \sum_{n=0}^{\infty} n a_n y^{n+1} + \lambda \sum_{n=0}^{\infty} a_n y^{n+1} = 0, \quad (\text{A.7.23})$$

doing a variable change and sorting terms we get

$$\sum_{n=0}^{\infty} \{[(n+1)n + (m+1)(n+1)] a_{n+1} + [\lambda - n] a_n\} y^n = 0. \quad (\text{A.7.24})$$

This equation is satisfied if the coefficient of each power of  $y$  vanish separately. This gives the recurrence relation

$$a_{n+1} = \frac{n - \lambda}{(n+1)(m+n+1)} a_n. \quad (\text{A.7.25})$$

This equation determines the coefficients of the general solution in Eq. (A.7.16). Expanding, by substituting Eq. (A.7.25) into Eq. (A.7.16) we get

$$p(y) = \left[ 1 - \frac{\lambda}{m+1}y - \frac{(1-\lambda)\lambda}{2(m+2)(m+1)}y^2 + \dots \right] a_0, \quad (\text{A.7.26})$$

as long as  $\lambda \geq 0$  the series converges. Also, we want the series to terminate at a given  $n$  because of normalizability. This happens when  $n - \lambda = 0$ . Since  $n$  is integer,  $\lambda$  is too. Relabeling  $\lambda = n$  we get the allowed values for  $n$

$$n = 0, 1, 2, 3, \dots \quad (\text{A.7.27})$$

We still need to determine  $a_0$ . Looking at Eq. (A.7.15) we see that  $p(y)$  can be multiplied with any constant and still be a solution. Since there exists a solution for each  $m$  and  $n$ , we can choose this constant to be different for each solution. From Eq. (A.7.26) we also see that we must have  $m \geq 0$  in order to get a non-divergent solution. This gives the associated Laguerre polynomials  $L_n^{|m|}$  as solution to Eq. (A.7.15). The first few are listed in Table A.4. The Rodrigues representation [Abramowitz and Stegun;

$n$	$L_n^{ m }(y)$
0	1
1	$-y +  m  + 1$
2	$\frac{1}{2}( m  + 1)( m  + 2) - 2( m  + 2)y + y^2$

**Table A.4:** Lowest order associated Laguerre polynomials.

1972] of the associated Laguerre polynomials are

$$L_n^{|m|}(y) = \frac{e^y y^{-|m|}}{n!} \frac{\partial^n}{\partial y^n} \left( e^{-y} y^{n+|m|} \right). \quad (\text{A.7.28})$$

We may also write the Laguerre polynomials as a finite series [Abramowitz and Stegun; 1972]

$$L_n^{|m|}(y) = \sum_{k=0}^n (-1)^k \frac{(n+|m|)!}{(n-k)! (|m|+k)! k!} y^k. \quad (\text{A.7.29})$$

Three recurrence relations are often used to generate the polynomials in a successive way. They are given as

$$\sum_{i=0}^n L_i^{|m|}(y) = L_n^{|m|+1}(y), \quad (\text{A.7.30})$$

$$L_n^{|m|}(y) = L_n^{|m|+1}(y) - L_{n-1}^{|m|+1}(y), \quad (\text{A.7.31})$$

and

$$L_{n+1}^{|m|}(y) = \frac{(2n+|m|+1-y)L_n^{|m|}(y) - (n+|m|)L_{n-1}^{|m|}(y)}{n+1} \quad (\text{A.7.32})$$

See [Abramowitz and Stegun; 1972] for details. A solution for the eigenvector is now obtained. If back-substitute and do some simple algebra we get the unnormalized

eigenvector corresponding to Eq. (A.7.1)

$$\psi(r) \propto \beta^{(|m|+1)/2} r^{|m|} e^{-\beta r^2/2} L_n^{|m|}(\beta r^2). \quad (\text{A.7.33})$$

To find the eigenvalues, we start with Eq. (A.7.14), but since the series needs to terminate at  $\lambda = n$ , we get

$$n = \frac{1}{2} \left( \frac{\epsilon}{2\beta} - m - 1 \right). \quad (\text{A.7.34})$$

Remember that we need to use absolute values of  $m$  to rule out divergent solutions. Substituting Eq. (A.7.34) back into Eq. (A.7.2) yields the eigenvalues

$$E = (2n + |m| + 1)\hbar\omega + m\hbar\omega_B. \quad (\text{A.7.35})$$

What is left in this section is to normalize the eigenvectors. Including the normalization factors we get the total normalized eigenvector for the two dimensional harmonic oscillator,

$$\psi_{nm}(r) = \sqrt{\frac{2n!}{(n+|m|)!}} \beta^{(|m|+1)/2} r^{|m|} e^{-\beta r^2/2} L_n^{|m|}(\beta r^2). \quad (\text{A.7.36})$$

If we now make use of Eq. (A.7.29) and the substitution  $\rho^2 = \beta r^2$ , the eigenvector above can be written as

$$\psi_{nm}(\rho) = \sqrt{\beta} \rho^{|m|} e^{-\rho^2/2} \sum_{k=0}^n a_{nmk} \rho^{2k}, \quad (\text{A.7.37})$$

where

$$a_{nmk} = (-1)^k \frac{\sqrt{2n! (n+|m|)!}}{(n-k)! (|m|+k)! k!}. \quad (\text{A.7.38})$$

### A.7.2 Three dimension

In three dimension the Schrödinger equation has the following form

$$-\frac{\hbar^2}{2m^*} \left\{ \frac{\partial^2}{\partial r^2} + \frac{2}{r} \frac{\partial}{\partial r} - \frac{l(l+1)}{r^2} - \frac{emB}{\hbar c} \right\} \psi(r) + \frac{1}{2} m^* \omega^2 r^2 \psi(r) = E \psi(r). \quad (\text{A.7.39})$$

Defining

$$\epsilon = \frac{2m^* E}{\hbar^2} - \frac{emB}{\hbar c}, \quad (\text{A.7.40})$$

and substituting

$$\psi(r) = \frac{1}{r} u(r), \quad (\text{A.7.41})$$

into Eq. (A.7.39) yields

$$-\frac{\partial^2 u(r)}{\partial r^2} + \left( \frac{l(l+1)}{r^2} + \frac{m^* 2\omega^2 r^2}{\hbar^2} \right) u(r) = \epsilon u(r). \quad (\text{A.7.42})$$

We need to make the equation dimensionless. Substituting  $\rho = \sqrt{m^*\omega/\hbar}r = \sqrt{\beta}r$  into the equation above, and at the same time defining

$$\epsilon' = \frac{\epsilon}{\beta}, \quad (\text{A.7.43})$$

results in the equation

$$-\frac{\partial^2 u'(\rho)}{\partial \rho^2} + \left( \frac{l(l+1)}{\rho^2} + \rho^2 \right) u'(\rho) = \epsilon' u'(\rho). \quad (\text{A.7.44})$$

Considering the limit  $\rho \rightarrow \infty$  just like we did for the two dimensional case, we see that we can do the substitution

$$u'(\rho) = e^{-\rho^2/2} p(\rho). \quad (\text{A.7.45})$$

This give rise to

$$-\frac{\partial^2 p(\rho)}{\partial \rho^2} + 2\rho \frac{\partial p(\rho)}{\partial \rho} + \left( \frac{l(l+1)}{\rho^2} + 1 - \epsilon' \right) p(\rho) = 0. \quad (\text{A.7.46})$$

Just as we did for two dimensions we can represent  $p(\rho)$  as a series. By using Eq. (A.7.16) and its derivatives in Eqs. (A.7.17) and (A.7.18) with  $y$  replaced by  $\rho$  we get the equation

$$\sum_{n=0}^{\infty} [2\rho^2(n+\sigma) - (n+\sigma)(n+\sigma-1) + l(l+1) + \rho^2(1-\epsilon')] a_n \rho^n = 0. \quad (\text{A.7.47})$$

Observe that for  $\rho = 0$  we can get divergence for  $n < 2$  unless  $a_1 = 0$ . As a consequence of this, all odd terms vanish. Using the same arguments as for two dimensions, we get the indicial equation

$$\sigma(\sigma-1) = l(l+1). \quad (\text{A.7.48})$$

This equations has two solutions. The first,  $\sigma = -l$  gives a divergence for  $\rho = 0$  and is not allowed. The last solution is valid in our case, since  $\sigma = l+1$  does not give rise to any divergencies. Substituting this value back into Eq. (A.7.47) and sorting terms we get

$$\sum_{n=0}^{\infty} [(2(n+l) + 3 - \epsilon')a_n - ((n+2l+3)(n+2))a_{n+2}] a_n \rho^n = 0. \quad (\text{A.7.49})$$

For this equation to be satisfied we require that the coefficient of each power of  $\rho$  vanish separately. The recurrence relation is then

$$a_{n+2} = \frac{2(n+l) + 3 - \epsilon'}{(n+2l+3)(n+2)} a_n. \quad (\text{A.7.50})$$

We need the series to terminate at  $n = n'$ . This is satisfied if

$$\epsilon' = 2(n' + l) + 3. \quad (\text{A.7.51})$$

Remember that for odd values of  $n$ , the series is zero. Only even values of  $n$  are relevant. Let us define  $n = 2k$  and  $n' = 2k'$ , where  $k, k' = 0, 1, 2, \dots$ . Using the

relations in Eqs. (A.7.40), (A.7.43), (3.1.10) and in addition redefine  $k' = n$  we get the eigenvalues corresponding to Eq. (A.7.39)

$$E = \left(2n + l + \frac{3}{2}\right) \hbar\omega + m\hbar\omega_B, \quad (\text{A.7.52})$$

with  $l = 0, 1, 2, \dots$  and  $m \leq l$ . The recurrence relation becomes

$$a_{2k+2} = \frac{k - k'}{(k + l + 3/2)(k + 1)} a_{2k}. \quad (\text{A.7.53})$$

Notice the similarities with Eq. (A.7.25). By writing the recurrence relation above for even values of the polynomial we get

$$a_{k+1} = \frac{k - k'}{(k + l + 3/2)(k + 1)} a_k, \quad (\text{A.7.54})$$

which is exactly equal to Eq. (A.7.25) apart from one constant term. Since we used the substitution  $x = r^2$  in the two dimensional case, the polynomials are also the same, apart from the constant term. The constant term can be shifted. By using all the same arguments as in App. A.7.1 with slight modification due to the extra dimension, we get the normalized eigenvector

$$\psi_{nl}(r) = \sqrt{\frac{2n!}{(n + l + 1/2)!}} \beta^{(l+3/2)/2} r^l e^{-\beta r^2/2} L_n^{l+1/2}(\beta r^2), \quad (\text{A.7.55})$$

with  $k' = n$ . The Laguerre polynomials  $L_n^{l+1/2}$  are discussed in the end of App. A.7.1. We may again rewrite the eigenfunction as a finite series using the substitution  $\rho^2 = \beta r^2$  and Eq. (A.7.29). This would give

$$\psi_{nl}(\rho) = \beta^{3/4} \rho^l e^{-\rho^2/2} \sum_{k=0}^n a_{nlk} \rho^{2k}, \quad (\text{A.7.56})$$

where

$$a_{nlk} = (-1)^k \frac{\sqrt{2n!} (n + l + 1/2)!}{(n - k)! (l + k + 1/2)! k!}. \quad (\text{A.7.57})$$

## A.8 Exact solution for the interacting part in relative coordinates

We will in this section solve the two-particle Coulomb interaction problem exact in two dimension. At the end we will mention the differences of the solutions if we where to do the same procedure in three dimensions. This method are outlined in [Taut; 1994]. It is a very special and limited case, but it is nevertheless important. The Schrödinger equation in question is

$$H\Psi = E_r\Psi, \quad (\text{A.8.1})$$

where the Hamiltonian for the electron-electron interaction has the following form

$$H = -\frac{\hbar^2}{2m^*} \left( \frac{\partial^2}{\partial r^2} + \frac{1}{r} \frac{\partial}{\partial r} + \frac{1}{r^2} \frac{\partial^2}{\partial \theta^2} + i \frac{eB}{\hbar c} \frac{\partial}{\partial \theta} \right) + \left( \frac{1}{2} m^* \omega^2 r^2 + \frac{e^2}{4\pi\epsilon\epsilon_0 r} \right), \quad (\text{A.8.2})$$

where

$$\omega^2 = \omega_0 + \omega_B^2, \quad (\text{A.8.3})$$

and  $m^*$  the effective electron mass. As in Sec. A.7.1 the eigenvectors are separable in  $r$  and  $\theta$ .

$$\Psi(r, \theta) = e^{im\theta} \psi(r). \quad (\text{A.8.4})$$

We can then put the Hamiltonian into Schrödinger's equation, do the substitution and obtain the equation

$$-\frac{\hbar^2}{2m^*} \left( \frac{\partial^2}{\partial r^2} + \frac{1}{r} \frac{\partial}{\partial r} - \frac{m^2}{r^2} - \frac{emB}{\hbar c} \right) \psi(r) + \left( \frac{1}{2} m^* \omega^2 r^2 + \frac{e^2}{4\pi\epsilon\epsilon_0 r} \right) \psi(r) = E_r \psi(r), \quad (\text{A.8.5})$$

which has similarities with the solution for the non-interacting case, however, the interacting term will yield significant complications in the solution process. First we include the constant term into the energy by defining

$$E'_r = \frac{2m^* E_r}{\hbar^2} - \frac{emB}{\hbar c}. \quad (\text{A.8.6})$$

To get rid of the derivative, we substitute

$$\psi(r) = r^{-1/2} u(r), \quad (\text{A.8.7})$$

into the equation. Sorting terms gives

$$-\left( \frac{\partial^2}{\partial r^2} + \left( \frac{1}{4} - m^2 \right) \frac{1}{r^2} \right) u(r) + \left( \frac{m^{*2} \omega^2}{\hbar^2} r^2 + \frac{2m^* e^2}{4\pi\hbar^2 \epsilon\epsilon_0 r} - E'_r \right) u(r) = 0. \quad (\text{A.8.8})$$

Again we introduce another substitution to make the coordinate dimensionless

$$\rho = \sqrt{\frac{\omega m^*}{\hbar}} r. \quad (\text{A.8.9})$$

After doing this we get the equation

$$\left( \frac{\partial^2}{\partial \rho^2} + \left( \frac{1}{4} - m^2 \right) \frac{1}{\rho^2} \right) u'(\rho) - \left( \rho^2 + \frac{l_B}{a_0'^* \rho} - \epsilon_r \right) u'(\rho) = 0, \quad (\text{A.8.10})$$

where

$$l_B = \sqrt{\frac{\hbar}{m^* \omega}}, \quad (\text{A.8.11})$$

$$a_0'^* = \frac{4\pi\epsilon\epsilon_0 \hbar^2}{2e^2 m^*}, \quad (\text{A.8.12})$$

$$\epsilon_r = \frac{\hbar E'_r}{m^* \omega}. \quad (\text{A.8.13})$$

The constant  $a_0'^*$  is known as the modified Bohr radius. We now consider the isolated case for  $\rho \rightarrow \infty$ . As  $\rho$  increases, the Coulomb repulsion decreases and when  $\rho$  is big enough we can disregard it. For the non-interacting case we saw that we then had a solution

$$u(\rho) \simeq e^{-\rho^2/2}, \quad (\text{A.8.14})$$

when  $\rho \rightarrow \infty$ . Since the interacting case also exists when  $\rho$  approaches infinity we know that this is part of our solution and we can substitute

$$u(\rho) = e^{-\rho^2/2} p(\rho), \quad (\text{A.8.15})$$

into Eq. (A.8.10) and get

$$\left( \frac{\partial^2}{\partial \rho^2} - 2\rho \frac{\partial}{\partial \rho} + \left( \frac{1}{4} - m^2 \right) \frac{1}{\rho^2} - \frac{l_B}{a_0'^* \rho} - 1 \right) p(\rho) + \epsilon_r p(\rho) = 0. \quad (\text{A.8.16})$$

We now need to do a series expansion. Looking at the equation we see that we have a singularity at  $\rho = 0$  and an irregular singularity at  $\rho = \infty$ . We can then use the Frobenius series as we did in the non-interacting case. Using the expansion

$$p(\rho) = \sum_{n=0}^{\infty} a_n \rho^{n+\sigma}, \quad (\text{A.8.17})$$

with the derivatives

$$\frac{\partial p(\rho)}{\partial \rho} = \sum_{n=0}^{\infty} (n+\sigma) a_n \rho^{n+\sigma-1}, \quad (\text{A.8.18})$$

$$\frac{\partial^2 p(\rho)}{\partial \rho^2} = \sum_{n=0}^{\infty} (n+\sigma-1)(n+\sigma) a_n \rho^{n+\sigma-2}. \quad (\text{A.8.19})$$

Substituting Eqs. (A.8.17), (A.8.18) and (A.8.19) into Eq. (A.8.16) and sorting terms yields

$$\sum_{n=0}^{\infty} \left\{ (n+\sigma-1)(n+\sigma) - 2(n+\sigma)\rho^2 + \left( \frac{1}{4} - m^2 \right) - \frac{l_B \rho}{a_0'^*} - (1 - \epsilon_r)\rho^2 \right\} a_n \rho^n = 0. \quad (\text{A.8.20})$$

Again, this equation should be valid for all  $\rho$ . If we put  $\rho = 0$  all terms with  $n > 0$  disappears and we are left with the indicial equation

$$(\sigma - 1)\sigma + \left( \frac{1}{4} - m^2 \right) = 0. \quad (\text{A.8.21})$$

Solving this equation gives two solutions

$$\sigma = \frac{1}{2} \pm m. \quad (\text{A.8.22})$$



Since this is a physical system, we do not want divergent solutions. Looking at the first solution  $\sigma = 1/2 - m$  we see that this diverges at  $\rho = 0$  if  $m > 0$ . We cannot allow this and the second solution is accepted as long as we only use positive values of  $m$ . The series expansion that will give a solution is then

$$p(\rho) = \rho^{1/2+|m|} \sum_{n=0}^{\infty} a_n \rho^n \quad (\text{A.8.23})$$

Looking at equation Eq. (A.8.20) we can derive the recurrence relation by doing a variable change. This results in

$$\begin{aligned} \sum_{n=0}^{\infty} \left\{ \left( (n + \sigma - 1)(n + \sigma) + \left( \frac{1}{4} - m^2 \right) \right) a_n \right. \\ \left. - (1 - \epsilon_r + 2(n + \sigma - 2)) a_{n-2} - \frac{l_B}{a_0'^*} a_{n-1} \right\} \rho^n = 0. \end{aligned} \quad (\text{A.8.24})$$

Again, this should be valid for all  $\rho$  giving rise to the recurrence relation

$$\begin{aligned} a_n &= \frac{1}{(n + \sigma - 1)(n + \sigma) + \left( \frac{1}{4} - m^2 \right)} \\ &\times \left[ (1 - \epsilon_r + 2(n + \sigma - 2)) a_{n-2} + \frac{l_B}{a_0'^*} a_{n-1} \right], \end{aligned} \quad (\text{A.8.25})$$

and inserting  $\sigma = 1/2 + |m|$  we obtain

$$\begin{aligned} a_n &= \frac{1}{\left( n + |m| - \frac{1}{2} \right) \left( n + |m| + \frac{1}{2} \right) + \left( \frac{1}{4} - m^2 \right)} \\ &\times \left[ (1 - \epsilon_r + 2 \left( n + |m| + \frac{1}{2} - 2 \right)) a_{n-2} + \frac{l_B}{a_0'^*} a_{n-1} \right]. \end{aligned} \quad (\text{A.8.26})$$

Further manipulations yields

$$a_n = \frac{1}{n(n + 2|m|)} \left[ (2(n + |m| - 1) - \epsilon_r) a_{n-2} + \frac{l_B}{a_0'^*} a_{n-1} \right], \quad (\text{A.8.27})$$

for  $n \geq 2$ . Remember that we demanded that  $a_0 \neq 0$ . The coefficient for  $a_1$  can be found as long as we demand  $a_n = 0$  for  $n < 0$ . This gives

$$a_1 = \frac{l_B}{a_0'^* (1 + 2|m|)}. \quad (\text{A.8.28})$$

We can now put the coefficients back into Eq. (A.8.17) and get a solution for  $p(\rho)$

$$\begin{aligned} p(\rho) = \rho^{1/2+|m|} \left[ 1 + \frac{l_B \rho}{(1 + 2|m|) a_0'^*} + \frac{\rho^2}{2(2 + 2|m|)} \right. \\ \left. \times \left( 2(1 + |m|) - \epsilon_r + \frac{l_B^2}{(1 + 2|m|) a_0'^{*2}} \right) + \dots \right] a_0. \end{aligned} \quad (\text{A.8.29})$$

The constant  $a_0$  needs to be determined, but if we put  $p(\rho)$  back into Eq. (A.8.16), we see that it does not matter what  $a_0$  is as long as it is non-zero. Let us set  $a_0 = 1$  for convenience. The series needs to terminate at some  $n$  for normalizability to be fulfilled. Say that this  $n$  is  $n'$ . Then we demand that  $a_{n'} = 0$  and  $a_{n'+1} = 0$ . Under these circumstances Eq. (A.8.27) gives us a way to determine  $e_r$  in the following way. Note that

$$a_{n'+1} = \frac{1}{(n'+1)(n'+1+2|m|)} \left[ (2(n'+|m|) - \epsilon_r) a_{n'} + \frac{l_B}{a_0'^*} a_{n'+1} \right], \quad (\text{A.8.30})$$

with  $a_n = 0$  and  $a_{n+1} = 0$ . Then solve for  $\epsilon_r$  and obtain

$$\epsilon_r = 2(n' + |m|). \quad (\text{A.8.31})$$

The condition for  $a_{n'} = 0$  gives a second condition

$$\frac{1}{n'(n'+2|m|)} \left[ (2(n'+|m|-1) - \epsilon_r) a_{n'-1} + \frac{l_B}{a_0'^*} a_{n'-2} \right] = 0. \quad (\text{A.8.32})$$

We defined  $\epsilon_r$  as

$$\epsilon_r = \frac{\hbar}{m^* \omega} \left( \frac{2m^* E_r}{\hbar^2} - \frac{emB}{\hbar c} \right). \quad (\text{A.8.33})$$

Combined with Eq. (A.8.31) this gives us the eigenvalues in Eq. (A.8.1)

$$E_r = (n' + |m|)\hbar\omega + m\hbar\omega_B. \quad (\text{A.8.34})$$

With  $\omega$  and  $\omega_B$  as defined above. The eigenvectors can now be calculated by using the recurrence relation and the two conditions in Eqs. (A.8.31) and (A.8.32). For illustrative purposes, let us calculate the exact eigenvalue for  $n = 2$ . We have already defined  $a_0 = 1$  and  $a_1 = l_B/a_0'^*(1 + 2|m|)$ . Using the two conditions in Eqs. (A.8.31) and (A.8.32) yields

$$\frac{l_B^2}{a_0'^*2} = 2(1 + 2|m|). \quad (\text{A.8.35})$$

This can be solved for  $\omega$  and employing Eq. (A.8.11) we get

$$\omega = \frac{\hbar}{2a_0'^*2m^*(1 + 2|m|)}. \quad (\text{A.8.36})$$

Using Eq. (A.8.34) yields

$$E_r = (n' + |m|)\frac{\hbar^2}{2a_0'^*2m^*(1 + |m|)} + m\hbar\omega_B, \quad (\text{A.8.37})$$

which is exact. At first this seems remarkable, but we must not forget that this solution only exists for specific  $\omega$  values. The three dimensional counterpart can be obtained by substituting  $|m| = l + 1/2$  in Eq. (A.8.27) and terminating as before. Note however that the structure of the total eigenfunction will be different due to for example a substitution  $r^{-1}$  instead of  $r^{-1/2}$  in Eq. (A.8.7). However, the polynomial in Eq. (A.8.23) will have the same form apart from the substitution  $|m| = l + 1/2$ .

## A.9 Expressions

This section lists expressions that are not derived, but used during calculation in this thesis.

### A.9.1 Coefficient for the two dimensional Coulomb interaction

For use in the series expansion of the energy matrix to give explicit expressions for the two dimensional Coulomb matrix, see [Brody et al.; 1960, Brody and Moshinsky; 1967] for details.

$$B(n'm, nm, p) = (-1)^{p-l} \frac{(2p+1)!}{2^{n'+n} p!} \times \sqrt{\frac{n'!n!(2n+2|m|+1)!(2n'+2|m|+1)!}{(n+|m|)!(n'+|m|)!}} \Lambda, \quad (\text{A.9.1})$$

where

$$\Lambda = \sum_{k=\nu}^{\xi} \left[ \frac{(|m|+k)!(p-k)!}{k!(2k+2|m|+1)!(n-k)!(2p+1-2k)!} \times \frac{1}{(n'-p+|m|+k)!(p-|m|-k)!} \right]. \quad (\text{A.9.2})$$

The summation limits are given by

$$\nu = \begin{cases} 0 & , \quad p - |m| - n' \leq 0 \\ p - |m| - n' & , \quad p - |m| - n' > 0 \end{cases}, \quad (\text{A.9.3})$$

$$\xi = \begin{cases} p - |m| & , \quad p - |m| \leq n \\ n & , \quad p - |m| > n \end{cases}. \quad (\text{A.9.4})$$

# Bibliography

- M. Abramowitz and I. A. Stegun. *Handbook of mathematical functions*. National Bureau of Standards, 1972.
- G. B. Arfken and H. J Weber. *Mathematical methods for physicists*. Academic Press, 1995.
- C. Bloch. Sur la théorie des perturbations des états liés. *Nucl. Phys.*, 6:329, 1958.
- J. J. Brehm and W. J. Mullin. *Introduction to the structure of matter*. John Wiley & Sons, New York, 1989.
- T. A. Brody and M. Moshinsky. *Tables of transformation brackets*. Gordon and Breach, New York, 1967.
- T. A. Brody, G. Jacob, and M. Moshinsky. Matrix elements in nuclear shell theory. *Nucl. Phys.*, 17:16, 1960.
- L. L. Chang, L. Esaki, and R. Tsu. Resonant tunneling in semiconductor double barriers. *Appl. Phys. Lett.*, 24:593, 1974.
- M. Ciorga, A. S. Sachrajda, P. Hawrylak, C. Gould, P. Zawadzki, S. Jullian, Y. Feng, and Z. Wasilewski. Addition spectrum of a lateral dot from coulomb and spin-blockade spectroscopy. *Phys. Rev. B*, 61:16318, 2000.
- C. Day. *Semiconductor quantum dots take first steps toward spin-based quantum computation*. Physics Today, March 2006.
- R. Dingle, W. Weigmann, and C. H. Henry. Quantum states of confined carriers in very thin  $\text{Al}_x\text{Ga}_{1-x}\text{As}$ -GaAs- $\text{Al}_x\text{Ga}_{1-x}\text{As}$  heterostructures. *Phys. Rev. Lett.*, 33: 827, 1974.
- A. R. Edmonds. *Angular momentum in quantum mechanics*. Princeton University Press, 1957.
- A. I. Ekimov, A. L. Efros, and A. A. Onushchenko. Quantum size effect in semiconductor microcrystals. *Solid State Commun.*, 56:921, 1985.
- T. Engeland. Oslo shell model code (unpublished). 1990-2006.
- T. Fukui, S. Ando, and Y. Tokura. GaAs tetrahedral quantum dot structures fabricated using selective area metalorganic chemical vapor deposition. *Phys. Rev. Lett.*, 58: 2018, 1991.

- H. Goldstein, C. P. Poole, and J. L. Safko. *Classical Mechanics*. Addison Wesley, 2002.
- G. H. Golub and C. F. Van Loan. *Matrix Computations*. Johns Hopkins, 1996.
- E. K. U. Gross and E. Runge. *Many-particle theory*. Adam Hilger, 1991.
- P. J. F. Harris. *Carbon nanotubes and related structures*. Cambridge University Press, 2002.
- T. Heinzl. *Mesoscopic Electronics in Solid State Nanostructures*. Wiley, 2003.
- M. J. Bowers II, J. R. McBride, and S. J. Rosenthal. White-light emission from magic-sized cadmium selenide nanocrystals. *J. Am. Chem. Soc.*, 127:15378, 2005.
- H.A. Jahn and J. Hope. Symmetry properties of the wigner 9j symbol. *Phys. Rev.*, 93:318, 1954.
- R. H. Landau and M. J. Páez. *Computational Physics*. John Wiley & Sons, New York, 1997.
- J. A. Lebens, C. S. Tsai, and K. J. Vahala. Applications of selective epitaxy to fabrication of nanometer scale wire and dot structures. *Appl. Phys. Lett.*, 56:2642, 1990.
- S. Y. Lee and K. Suzuki. Convergent theory for effective interaction in nuclei. *Prog. Theor. Phys.*, 64:2091, 1980.
- J.-Y. Marzin, J.-M. Gérard, A. Izraël, D. Barrier, and G. Bastard. Photoluminescence of singel inas quantum dots obtained by self-organized growth on gaas. *Phys. Rev. Lett.*, 73:716, 1994.
- J. Millman and A. Grabel. *Microelectronics*. McGraw-Hill, 1987.
- P. J. Mohr and B. N. Taylor. *The 2002 CODATA Recommended Values of the Fundamental Physical Constants (Web Version 4.2)*. This database was developed by J. Baker, M. Douma, and S. Kotochigova. Available: <http://physics.nist.gov/constants>. National Institute of Standards and Technology, Gaithersburg, 2006.
- M. Moshinsky. Transformation brackets for harmonic oscillator function. *Nucl. Phys.*, 13:104, 1959.
- M. Moshinsky. *The harmonic oscillator in modern physics: From atoms to quarks*. Gordon and Breach, New York, 1969.
- M. E. Peskin and D. V. Schroeder. *An introduction to quantum field theory*. Westview Press, 1995.
- P. M. Petroff, A. C. Gossard, R. A. Logan, and W. Wiegmann. Toward quantum well wires: Fabrication and optical properties. *Appl. Phys. Lett.*, 41:635, 1982.
- W. H. Press, S. A. Teukolsky, W. T. Vetterling, and B. P. Flannery. *Numerical Recipes in C*. Cambridge, 2002.
- M. A. Ratner. *Molecular Electronics*. Blackwell, 1997.

- S. Raymond, S. Fafad, P. J. Poole, A. Wójs, P. Hawrylak, S. Charbon-Neau, D. Leonard, R. Leon, P. M. Petroff, and J. L Merz. State filling and time-resolved photoluminescence of excited states in  $\text{In}_{1-x}\text{Ga}_x\text{As}/\text{GaAs}$  self-assembled quantum dots. *Phys. Rev. B*, 54:11548, 1996.
- M.A. Reed, R. T Bate, K. Brandshaw, W. M. Duncan, W. M. Frensley, J. W. Lee, and H. D. Smith. Spatial quantization in GaAs-AlGaAs multiple quantum dots. *J. Vacuum Sci. Technol. B*, 4:358, 1986.
- K. F. Riley, M. P. Hobson, and S. J. Bence. *Mathematical Methods. For physics and engineering*. Cambridge, 2003.
- R. Shankar. *Principles of Quantum Mechanics*. Kluwer Academic/Plenum Publishers, 1994.
- K. Suzuki. Construction of hermitian effective interaction in nuclei. *Prog. Theor. Phys.*, 68:246, 1982.
- K. Suzuki and R. Okamoto. Effective operators in time-independent approach. *Prog. Theor. Phys.*, 93:905, 1995.
- I. Talmi. *Helv. Phys. Acta*, 25:185, 1952.
- M. Taut. Two electrons in a homogeneous magnetic field: particular analytical solutions. *J. Phys. A:Math. Gen.*, 27:1045, 1994.
- W. G. van der Wiel, M. Stopa, T. Koder, T. Hatano, and S. Tarucha. Semiconductor quantum dots for electron spin qubits. *New Journal of Physics*, 8:28, 2006.